Dissertation

Computational aeroacoustics for the characterization of noise sources in rotating systems

performed for the purpose of obtaining the academic degree
of Doctor of Technical Science
under the supervision of

Univ.Prof. Dipl.-Ing. Dr.techn. Manfred Kaltenbacher
Institute of Mechanics and Mechatronics
Research Unit of Technical Acoustics, E325-03

submitted to the Vienna University of Technology
Faculty of Mechanical and Industrial Engineering

by

Dipl.-Ing. Clemens Junger
Mat.Nr. 01426688
Zeillergasse 35/20-21
1170 Wien

revied by

Prof. Dr.-Ing. habil Stefan Becker
Friedrich-Alexander Universität Erlangen-Nürnberg
Lehrstuhl für Prozessmaschinen und Anlagentechnik
Cauerstraße 4, 91058 Erlangen

Univ.Prof. Dipl.-Ing. Dr.Ing. Christian Bauer
TU Wien
Institute for Energy Systems and Thermodynamics
Getreidemarkt 9, 1060 Wien

"Ich hege wirklich längst die Meinung, daß die Quantität Lerm, die Jeder unbeschwert vertragen kann, in umgekehrtem Verhältniß zu seinen Geisteskräften steht, und daher als das ungefähre Maaß derselben betrachtet werden kann."

— Arthur Schopenhauer, *Die Welt als Wille und Vorstellung*

Ehrenwörtliche Erklärung

Ich erkläre ehrenwörtlich, dass ich die vorliegende wissenschaftliche Arbeit selbstständig angefertigt und die mit ihr unmittelbar verbundenen Tätigkeiten selbst erbracht habe. Ich erkläre weiters, dass ich keine anderen als die angegebenen Hilfsmittel benutzt habe. Alle aus gedruckten, ungedruckten oder dem Internet im Wortlaut oder im wesentlichen Inhalt übernommenen Formulierungen und Konzepte sind gemäß den Regeln für wissenschaftliche Arbeiten zitiert und durch Fußnoten bzw. durch andere genaue Quellenangaben gekennzeichnet.

Die wissenschaftliche Arbeit ist noch keiner anderen Prüfungsbehörde vorgelegt worden. Diese Arbeit wurde in gedruckter und elektronischer Form abgegeben. Ich bestätige, dass der Inhalt der digitalen Version vollständig mit dem der gedruckten Version übereinstimmt.

Clemens Junger - Wien, 17.10.2019

Abstract

The objective of computational aeroacoustics is the prediction of sound generated by turbulent flow. Its utilization in design processes demands the prediction, and consequently the manipulation of sound. Therefore, not only the radiated sound is of interest, but also the flow mechanisms generating the noise sources have to be understood. A large area where sound prediction is applied - from aircraft engines down to vacuum cleaners - includes rotating systems. The aeroacoustic investigations in this work are applied to a low pressure axial fan benchmark, to be able to compare the results with measurements. The first aim of this work is the investigation of the prerequisites a simulation needs to fulfill to predict the sound correctly, as the rotation yields special challenges on the flow computation and the aeroacoustic methods. The second aim is the comparison with different prediction methods, and the third aim is to investigate the obtained information about noise sources in the rotating system.

Applied and compared are different methods, from empirical formulas to state of the art computational aeroacoustic prediction methods. In the computational prediction, detailed information about the flow field is needed. To obtain the information, a transient flow simulation was performed. For the validation of the flow simulation, flow velocity, pressure rise and wall pressure spectra were compared with the measurement results from the benchmark. From the sound prediction with the perturbed convective wave equation it can be seen that at least five revolutions of the fan have to be computed before tonal components in the acoustic spectrum can be predicted. The interpolation of acoustic sources as well as the spatial discretization have little influence on the acoustic result but large influence on the computational effort. Compared to that, blending of the acoustic source term can have more influence on the result of the aeroacoustic prediction. The over all sound power level is predicted with only a deviation of $0.6\,\mathrm{dB}$ compared to the measurements but the spectral prediction of the first subharmonic peak was not sufficient. The Ffowcs-Williams and Hawkings analogy is able to predict the first subharmonic peak but has a deviation of $2.1\,\mathrm{dB}$ in the over all sound pressure level compared to the measurements. Semi empirical methods predict the over all sound power level to an accuracy below $2\,\mathrm{dB}$. The stochastic noise prediction methods, predict the sound sources at the leading edges of the fan blades and in the flow of the boundary layer and tip flow. From the flow simulation, it can be seen that the tip flow leads to interactions with the blades. The investigations of the aeroacoustic sources show that the tip flow results in noise sources at the outer diameter of the fan, but the strength of the sources varies over the simulation time. Further strong sources occur at the leading edges of the blades. For higher frequencies acoustic sources become more and more compact.

Kurzfassung

Die Aufgabe der numerischen Aeroakustik ist die Schallvorhersage von turbulenten Strömungen. Im Designprozess ist ihre Aufgabe sowohl die Vorhersage, als auch die Veränderung von Schall. Deshalb besteht nicht nur Interesse am nach außen abgestrahlten Schall, sondern auch am Verständnis der Lärmquellen erzeugenden Strömungsmechanismen. Ein großes Gebiet auf dem Schallvorhersage betrieben wird - von Flugzeugtriebwerken bis hin zu Staubsaugern - beinhaltet rotierende Systeme. Die aeroakustischen Untersuchungen in dieser Arbeit finden Anwendung an einem Benchmark eines axialen Niederdrucklüfters, um Vergleiche mit Messergebnissen zu ermöglichen. Da die Rotation besondere Anforderungen an die Strömungsberechnung und die aeroakustischen Methoden stellt, ist das erste Ziel dieser Arbeit die Untersuchung, welche Voraussetzungen eine Simulation erfüllen muss, um Schall richtig vorherzusagen. Das zweite Ziel ist der Vergleich unterschiedlicher Vorhersagemethoden und das dritte Ziel ist die Untersuchung der Lärmquellen im rotierenden System.

Zur Vorhersage werden empirische Formeln bis hin zu numerischer Aeroakustik auf dem aktuellen Stand der Technik angewendet. In der numerischen Vorhersage werden detaillierte Informationen über das Strömungsfeld benötigt. Um diese zu erhalten, wurde eine transiente Strömungssimulation durchgeführt. Für die Validierung der Strömungssimulation wurden Strömungsgeschwindigkeit, Druckanstieg und Wanddruckspektren mit den Messungen des Benchmarks verglichen. Die Schallvorhersage mit der konvektiven Störungswellengleichung zeigt, dass mindestens fünf Umdrehungen des Lüfters simuliert werden müssen, bevor tonale Komponenten im akustischen Spektrum vorhergesagt werden können. Die Interpolation der akustischen Quellen und die räumliche Auflösung haben wenig Einfluss auf das akustische Ergebnis aber großen Einfluss auf den Berechnungsaufwand. Im Vergleich dazu kann Beschneidung der akustischen Quellen mehr Einfluss auf die aeroakustische Vorhersage haben. Der Gesamtschallleistungspegel dieser Schallvorhersage hat lediglich eine Abweichung von $0.6\,\mathrm{dB}$ im Vergleich mit den Messungen, aber die Vorhersage des ersten subharmonischen Peaks ist nicht ausreichend. Die Ffowcs-Williams Hawkings Analogie ist in der Lage den ersten subharmonischen Peak vorherzusagen aber hat eine Abweichung im Gesamtschallleistungspegel von $2.1\,\mathrm{dB}$ im Vergleich mit den Messungen. Die Genauigkeit der semiempirischen Vorhersagemethoden ist unter $2\,\mathrm{dB}$ im Gesamtschallleistungspegel. Die stochastischen Vorhersagemethoden verorten die Lärmquellen an den Blattvorderkanten des Lüfters und in der turbulenten Grenzschicht sowie in der Kopfspaltströmung. In den Ergebnissen der Strömungssimulation ist ersichtlich, dass es durch Kopfspaltströmung zu einer Interaktion mit den Blättern kommt. Die Untersuchung der aeroakustischen Lärmquellen zeigt, dass die Kopfspaltströmung zu Lärmquellen am äußeren Radius des Lüfters führt, aber die Stärke der Lärmquellen mit der Zeit variiert. Weitere starke Lärmquellen treten an den Blattvorderkanten auf. Für höhere Frequenzen werden die Lärmquellen zunehmend kompakt.

Danksagung

Zuerst möchte ich meinen Dank an Univ.Prof. Dipl.-Ing. Dr.techn. Manfred Kaltenbacher richten, der mich während dieser Arbeit betreute, und der mich stets unterstützte und mir dabei alle Freiheiten ließ, die ich nötig hatte. Darüber hinaus, bin ich ihm dankbar für die kollegiale Arbeitsatmosphäre für die er in unserer Arbeitsgruppe gesorgt hat. Zudem möchte ich mich auch bei Univ.Prof. Dipl.-Ing. Dr.Ing. Christian Bauer und Prof. Dr.-Ing. habil Stefan Becker bedanken, die meine Arbeit begutachteten.

Während meiner Arbeit am Institut für Mechanik und Mechatronik hatte ich das Glück hervorragende Kollegen zu haben, die mir durch manche schwere Stunde geholfen haben und zu guten Freunden geworden sind. Für die Bereitstellung der Messdaten und anregende Diskussionen bedanke ich mich bei Florian Krömer. Bei Andreas Hüppe bedanke ich mich dafür, dass er mich betreut hat und immer ein offenes Ohr für meine Probleme hatte und bei Stefan Zörner für die Einführung in die Freuden von Linux und seinen feinen Humor. Bei Beiden bedanke ich mich für den ein oder anderen Abend, der nicht an der TU verbracht wurden. Jochen Metzger danke ich für seine Vorbildfunktion - auch im Privaten - und zusammen mit Stefan Gombots für die gute Zusammenarbeit in der Lehre. Sebastian Floss danke ich für anregende Gespräche über alles. Bei Klaus Roppert bedanke ich mich für die Bereitschaft abends notfalls auch den Zug zu verpassen. Zudem bedanke ich mich bei Kirill Shaposhnikov, Dominik Perchthold, David Tumpold, Stefan Schoder, Jonathan Nowak, Clemens Freidhager, Philipp Seebacher, Felix Gassenmayer, Ferdinand Pacher und Florian Toth für anregende Diskussionen, Unterstützung bei der angewandten Akustik, kollegiales Verhalten und vieles mehr. Weiters möchte ich mich bei Birgit Pimperl, Renate Mühlberger, Ruth Tscherne und Georg Canek für alles Organisatorische bedanken, sowie bei Peter Unterkreuter, Christoph Keppel, Reinhold Wagner und Manfred Neumann.

Mein ganz besonderer Dank gehört meiner Freundin Alexandra, die mich stets ertragen und unterstützt hat. Ohne Sie wäre meine Arbeit nicht unmöglich aber unerträglich gewesen. Zudem danke ich meiner Familie und allen Freunden, die mich auf meinem Weg unterstützt und bestärkt haben.

Contents

Introduction

Jean Arp wrote in Arp on Arp: "Soon silence will have passed into legend. Man has turned his back on silence. Day after day he invents machines and devices that increase noise and distract humanity from the essence of life, contemplation, meditation . . . tooting, howling, screeching, booming, crashing, whistling, grinding, and trilling bolster his ego. His anxiety subsides. His inhuman void spreads monstrously like a gray vegetation." To save the silence, we have to decrease noise and build quieter machines. And it is not just about distraction and annoyance, it is also about health. Noise exposure can lead to health issues in different ways. The most direct is hearing loss, but there are also indirect issues like an increased stress level or disturbance of sleep that effect a healthy life. A detailed description of this topic and measures against it can be found in [29]. For that reason a lot of directives were passed in the EU to regulate noise exposure over the last decades. This directives lead to the current state of the art, where the generated noise of new products has to fulfill certain acoustic criteria. This is normally tested at the end of the design process by measurements of the finished product. But to build quieter machines we need a better understanding of the noise sources. This enables us to predict noise and incorporate it in the design process as a quality criterion.

For many flow related applications like jets, the main noise sources arise due to aerodynamic quantities - for example fluctuations in the pressure field. The acoustics of such applications is therefore called aeroacoustics. Many applications - from aircraft engines down to vacuum cleaners - includes rotating systems. The aeroacoustic investigations in this work are applied to a low pressure axial fan benchmark, to be able to compare the results with measurements. The numerical approach to the problem is called Computational Aeroacoustics (CAA) and is strongly related to Computational Fluid Dynamics (CFD) to predict the aerodynamic quantities. Therefore, the first aim of this work is to obtain CFD data describing the flow field. The important point here is to resolve not only the aerodynamic quantities but the sound producing fluctuations. Furthermore, the rotating geometry yields additional challenges. The second aim is to compare different aeroacoustic methods with the benchmark. They all have their advantages and disadvantages and vary largely in computational effort and accuracy.

The third aim of this work is to use obtained informations of the aeroacoustic methods to investigate the noise sources of the axial fan.

1.1. Noise regulations

The different noise directives aim on the noise sources but also on environmental noise and save working conditions. For example the directive 2003/10/EC of the European Parliament and of the Council on the minimum health and safety requirements regarding the exposure of workers to the risks arising from physical agents (noise) [112] defines measures to be taken if a peak sound pressure p_{peak} or an average daily noise exposure level L_{EX} is exceeded.

- Above $L_{\mathrm{EX}} = 80\,\mathrm{dB(A)}$ or $p_{\mathrm{peak}} = 112\,\mathrm{Pa}$ "the employer shall make individual hearing protectors available to workers".

- Above $L_{\mathrm{EX}} = 85\,\mathrm{dB(A)}$ or $p_{\mathrm{peak}} = 140\,\mathrm{Pa}$ "individual hearing protectors shall be used" and "... the employer shall establish and implement a programme of technical and/or organisational measures intended to reduce the exposure to noise...".

- A value of $L_{\mathrm{EX}} = 87\,\mathrm{dB(A)}$ or $p_{\mathrm{peak}} = 200\,\mathrm{Pa}$ shall never be exceeded.

The directive 2006/42/EC [113] also called machinery directive forces manufacturers to include in product manuals:

- "the A-weighted emission sound pressure level at workstations, where this exceeds $70\,\mathrm{dB(A)}$; where this level does not exceed $70\,\mathrm{dB(A)}$, this fact must be indicated,

- the peak C-weighted instantaneous sound pressure value at workstations, where this exceeds $63\,\mathrm{Pa}$ ($130\,\mathrm{dB}$ in relation to $20\,\mathrm{\mu Pa}$),

- the A-weighted sound power level emitted by the machinery, where the A-weighted emission sound pressure level at workstations exceeds $80\,\mathrm{dB(A)}$."

This means that the manufacturer has to be concerned about noise measurement as soon, as the sound pressure level is high enough. A similar regulation exists for machinery used outdoors [111]. Of course further noise regulations exist for automobiles, aircraft, railways, etc. In Germany the "TA Lärm" [19] based on the "Bundes-Immissionsschutzgesetz" gives strong limits to the noise levels inside and outside buildings for a wide range of applications. Some limits outside buildings are shown in Tab. 1.1. The limits at day time are applicable from 6 AM to 10 PM, the limits at night from 10 PM to 6 AM. Especially the values in the residential area are low and in need of protection. The noise limits inside buildings are even lower. Table 1.2 shows the noise limits for day and night time. In Austria, the "ArbeitnehmerInnenschutzgesetz" [1] states, that the employer has to achiev a noise exposure as low as reasonably possible. The "Verordnung Lärm und Vibrationen" [5] incorporates the limits of [113] but also gives limits for special rooms corrected with an annoyance level. This corrected limits are $65\,\mathrm{dB(A)}$ for rooms where simple office tasks are done and $50\,\mathrm{dB(A)}$ for rooms where mainly intellectual activity are done or recreation rooms, sanitary rooms and living rooms.

Table 1.1.: Noise limits outside buildings according to [19]

Industrial areas	75 dB(A)
Employment zone	at day 65 dB(A) at night 50 dB(A)
Urban area	at day 63 dB(A) at night 45 dB(A)
...	...
Residential are	at day 50 dB(A) at night 35 dB(A)
Spa areas and hospitals	at day 45 dB(A) at night 35 dB(A)

Table 1.2.: Noise limits inside buildings according to [19]

day	35 dB(A)
night	25 dB(A)

1.2. Noise sources of fans

The acoustic spectrum of a fan consists of broadband noise and tonal components. A schematic spectrum with different characteristics from [121] is shown in Fig. 1.1. The lower limit of the Sound Pressure Level (SPL) is given by the ambient noise. At low frequencies, steady blade forces dominate the spectrum. Although they are steady on the rotating fan, they cause a rotating pressure field for the stationary observer. Unsteady blade forces produce tonal components at the Blade Passing Frequency (BPF) and its higher harmonics. They can result from turbulent, non uniform inflow or interactions of the rotor with the stator. The interaction of the upstream flow with the blades is expected to be strongest at the leading edges of the blades, where this interaction first takes place. The noise mechanisms of turbulent and laminar vortex shedding are located in the higher frequency range. If laminar shedding occurs it can have a strong tonal characteristic. These noise mechanisms can occur without any influence of the upstream flow and can be described in analogy to airfoil noise [18, 20], where they are referred to as airfoil self noise. In turbulent boundary layers, the turbulent structures interact with the trailing edge and produce noise. If the trailing edge is blunt, a von Kármán vortex street can occur behind the profile and generate vortex shedding noise. Since the interactions are less coherent due to the turbulence in the boundary layer, this generates broadband noise. Vortex shedding noise can also occur for sharp trailing edges if the boundary layer is laminar. Then it is more coherent and therefore generates a distinct peak. Broadband noise sources occur for flow separations and stall at the blades or a rotating stall at the fan. For airfoils of finite span a tip vortex occurs which is also generating noise. In the case of a ducted fan, this
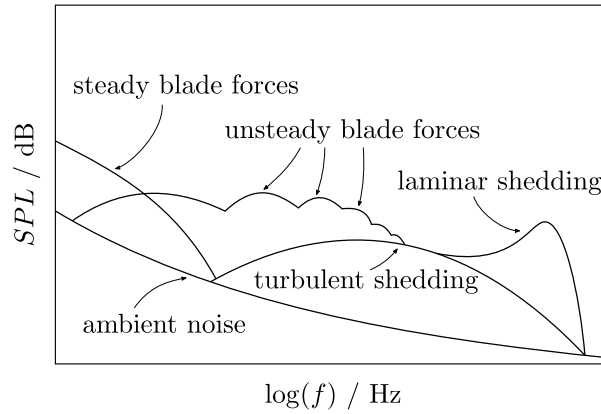
Figure 1.1.: Acoustic spectrum of an axial fan from [121].

corresponds to the sound produced by the tip flow between the blade tip and the duct. The tip flow induces a secondary flow, which is moving in circumferential direction with a velocity lower than the rotational velocity of the fan. This secondary flow can therefore interact with the following blades and produce noise at different frequencies than the BPF. In literature, this is commonly referred to as subharmonic tip noise. In [69] the schematic spectrum of [121] is extended by this subharmonic tip noise.

Noise prediction methods

Noise prediction methods have their origin in the mid of last century. Since then, a large variety of methods emerged from them and completely new approaches were invented. They differ strongly in how the sound producing mechanisms are described. But they also differ in the acoustic quantities they are describing. Where the simplest ones predict an averaged sound pressure level, the more sophisticated ones predict a spectral information. For the most advanced methods not only the emitted sound is considered, but also the acoustic propagation. The complexity of this methods differs strongly and some of them can be very demanding in computational time and effort. They also differ in the amount of insight in the noise producing mechanisms.

This chapter gives an overview of different noise prediction methods that are used nowadays. Basic information about their application and what their advantages and disadvantages are will be given. This is not meant to be a complete aggregation of all noise prediction methods but an overview of methods applicable to the prediction of fan noise. In cases where the methods are specific for a certain fan type, the specification for an axial fan is used.

To get an overview of the different approaches, the existing noise prediction methods are categorized based on their complexity and computational effort. A distinction of three different categories was done in [21]. The first category contains semi-empirical prediction methods, which correlate basic machine parameters with the generated sound. The second category contains methods that are able to distinguish between different sound producing mechanisms. For this methods some flow quantities may be needed from measurements or steady Computational Fluid Dynamics CFD or so called Reynolds Averaged Navier-Stokes (RANS) simulations. The third category contains Computational Aeroacoustic (CAA) methods that need high-fidelity flow field data, usually obtained by unsteady CFD simulations. These methods are also able to take the complex geometry of the fan into account. A fourth category for the direct aeroacoustic computation was suggested in [81]. In this category no model assumptions are made except them from the underlying CFD simulation.

The de facto industry standard for fan characteristics prediction is the usage of RANS

simulations. They are used to calculate fan performance like pressure raise and efficiency, and in general they are sufficient as long as the fan is operated at a stationary operating point. The quantities obtained by this simulations allow the usage of class 1 and 2 noise prediction methods. The effort for the class 3 and 4 methods is very high, due to the high accuracy that is needed in the unsteady CFD simulations. This limits their application mainly to research where the extended insight in the sound generating mechanisms is of interest. A simplified comparison of different prediction methods was already shown in [57].

2.1. Class 1 methods

The class 1 methods are the most basic ones and allow a rough estimation of the emitted noise. They are based on (semi-)empirical methods, which try to draw a connection from basic fan parameters to acoustic quantities, and rely on reference values. In general an overall sound power level is the result, which means that no spectral information can be obtained. For none of these noise prediction methods, the frequency range for the overall sound power level prediction is given. This may lead to differences to measurements where the measured frequency range is always restricted in one way or the other.

In one of the first fan noise predictions [76], the emitted sound power was assumed to be proportional to the square of the fan diameter and the circumferential velocity to the power of some empiric quantity. This proportionality can be rewritten to the volume flow rate and square to the pressure rise. Such a proportional relation can be found in many class 1 methods.

2.1.1. VDI 2081

The VDI 2081 standard [3] "Noise generation and noise reduction in air-conditioning systems" contains a noise prediction that is based on the noise law of Bommes [15]. It estimates the outlet duct sound power level L_W in the form of

$$L_\mathrm{W} = L_\mathrm{WS} + 10 \lg \dot{V} + 5(\gamma - 1) \lg \Delta p \quad \text{in dB}, \tag{2.1}$$

which is just a function of the volume flow rate $\dot{V}$, the total pressure increase Δp between the inlet chamber and the ambience, the specific sound power level L_WS and the Mach number exponent γ. The specific sound power level is assumed to be constant for fans with a diameter larger than 400 mm, and the Mach number exponent can be assumed to be $\gamma = 5$. This leads to a noise prediction in the form

$$L_\mathrm{W} = L_\mathrm{WS} + 10 \lg \dot{V} + 20 \lg \Delta p \quad \text{in dB}, \tag{2.2}$$

which is very similar to the estimation of [76]. For axial fans the specific sound power level can be estimated to be $L_\mathrm{WS} = 42\,\mathrm{dB}$. This estimation yields for the design point. How valid these assumptions are when the fan is not operated around the design point is questionable.

2.1.2. VDI 3731

The VDI 3731 standard [4] "Characteristic noise emission values of technical sound sources" part 2 contains a noise prediction that is based on Eck [27]. In this method, the sound

power P is assumed to be proportional to the aerodynamic power loss and an exponent of the circumferential Mach number

$$P \propto \dot{V} \Delta p \left(\frac{1}{\eta_i} - 1 \right) (\mathrm{Ma}_u)^m \,, \tag{2.3}$$

with the inner efficiency η_i (efficiency without losses due to leakage and friction in bearings), the Mach number exponent m and the circumferential Mach number Ma_u. The circumferential Mach-number is

$$\mathrm{Ma}_u = \frac{u_a}{c_0} = \frac{\pi D n}{c_0} \,, \tag{2.4}$$

with the fan diameter D, the rotational speed n and the speed of sound c_0. This can be written in a logarithmic form as

$$L_\mathrm{W} = L_\mathrm{WS} + 10 \lg \left[\frac{\dot{V}}{\dot{V}_0} \frac{\Delta p}{\Delta p_0} \left(\frac{1}{\eta} - 1 \right) \right] + 10\, m \lg \left[\mathrm{Ma}_u \right] \quad \text{in dB} \,, \tag{2.5}$$

with the reference values $\dot{V}_0 = 1\,\mathrm{m^3/s}$ and $\Delta p_0 = 1\,\mathrm{Pa}$. The measurement of the inner efficiency η_i is difficult, and therefore it is replaced with the total-to-static efficiency of the fan η. For axial fans, the specific sound power level can be assumed to be $L_\mathrm{WS} = 96.6\,\mathrm{dB}$ in a certain proximity to the design point and the exponent to $m = 3.16$. The total-to-static efficiency of the fan is

$$\eta = \frac{\dot{V} \Delta p}{2 \pi n M} \,, \tag{2.6}$$

with M the torque of the shaft. On the one hand, the assumption of the aerodynamic power loss as the source of the acoustic power gives a very figurative connection between both. On the other hand, the direct connection is questionable, since the aerodynamic losses are much larger than the acoustic power.

2.2. Class 2 methods

The class 2 methods distinguish the noise from different noise sources. The total noise is then expressed as a sum of the single noise sources. The flow quantities needed for the prediction are mostly averaged quantities, like inflow velocity, which can be obtained by steady CFD simulations. Otherwise they can be obtained by measurements and transferred to other designs. Most of them consider a simplified geometry like straight flat plates. This means that the best noise prediction can be assumed for simple fan geometries. The transferability to skewed or otherwise optimized fans has to be checked individually.

2.2.1. Sharland

The method of Sharland [102] makes a prediction of the over all sound power. It assumes the blades to be flat, incoherently radiating without any interfering effects. Sharland distinguishes between three different noise sources. The first one origins from the turbulent inflow (ti), the second one from pressure fluctuations in the turbulent boundary layer (tbl) and the third one

from vortex shedding at the trailing edge of the blade (vs)

$$P = P_{\text{ti}} + P_{\text{tbl}} + P_{\text{vs}} \,. \tag{2.7}$$

All noise contributions are approximated by an integral from the inner radius r_i to the outer radius r_o of the blade. All of them are scaled with an empirical constant and the relation of density and speed of sound ρ/c_0^3.

$$P_{\text{ti}} \approx z \frac{1}{48\pi} \frac{\rho}{c_0^3} \int_{r_i}^{r_o} l \Phi^2 w_\infty^6 \text{Tu}^2 \mathrm{d}r \tag{2.8a}$$

$$P_{\text{tbl}} \approx z \cdot 10^{-7} \frac{\rho}{c_0^3} \int_{r_i}^{r_o} l w_\infty^6 \mathrm{d}r \tag{2.8b}$$

$$P_{\text{vs}} \approx z \frac{1}{120\pi} \frac{\rho}{c_0^3} \int_{r_i}^{r_o} l w_\infty^6 \text{Re}^{-0.4} \mathrm{d}r \tag{2.8c}$$

All noise sources are dependent on the cord length l of the blade and the relative velocity w_∞. The noise contribution from the turbulent inlet depends on the turbulent intensity Tu, and the gradient of the lift coefficient Φ, which was approximated by Sharland as $\Phi \approx 0.9\pi$. The noise contribution of the turbulent boundary layer is purely dependent on the size of the blade and the noise contribution of the vortex shedding is dependent on the Reynolds number Re. This assumption for the vortex shedding might be a bit too generalized since the vortex depends on the individual geometry of the blade. For sharp trailing edges it might be very small. The sound power of each contribution is then multiplied by the number of blades z. The integrals may be approximated by an evaluation of the quantities at a representative radius of the blade, which makes the noise prediction easier. A height of about 70% of the blade seems to be applicable often [20].

2.2.2. Költzsch

The method of Költzsch [66] makes a prediction of the power spectral density (PSD) and therefore provides spectral information of the radiated sound. The distinguished sound sources are based on the turbulent inlet (ti) and the turbulent boundary layer (tbl)

$$S = S_{\text{ti}} + S_{\text{tbl}} \,. \tag{2.9}$$

The PSD of the turbulent inflow is approximated with the spectral energy density S_w of the inflow. This is scaled with the dimensions of the blade l and b and the number of blades

$$S_{\text{ti}}(f) \approx z \frac{0.81\pi}{48} \frac{\rho}{c_0^3} w_\infty^4 S_w(f) \, lb \,. \tag{2.10}$$

In the same way as the method of Sharland in eq. (2.8) this contribution uses an empirical constant and the proportionality to ρ/c_0^3. The inflow spectral energy density is computed as

$$S_w(f) = \bar{u} \text{Tu}^2 \Lambda \, 10^{F(f)/10} \,, \tag{2.11}$$

with the mean inflow velocity $\bar{u}$, the turbulence properties turbulent intensity Tu and turbulent length scale Λ, and a regression polynomial F. The turbulent length scale can be obtained from measurements or RANS simulations. The regression polynomial writes as

$$F(f) \approx \sum_{k=1}^{4} a_k \left(\lg \left(\frac{f\Lambda}{c_0} \right) \right)^{k-1}, \tag{2.12}$$

where the coefficients for the polynomial are

$$a_k = -9.784; -19.001; -5.548; -0.060. \tag{2.13}$$

The PSD of the turbulent boundary layer for a fan in a sound hard duct[1] computes as

$$S_{\text{tbl}} = z\frac{\pi}{4} \frac{f}{\rho c_0^2 r_o (1-\nu^2)^2} S_{\text{bl}}(f)\psi, \tag{2.14}$$

with the PSD of the lift forces on the blade S_{bl}, the frequency f, the outer radius r_o, a radiation function ψ that can be approximated as $\psi \approx 1$ for low Mach number flows and the relation of the outer diameter to the hub ν. The total noise contribution is again obtained by a multiplication with the number of blades. The approximation of the PSD of the lift forces S_{bl} is described by three different functions, depending on the frequency, the blade geometry and the relative velocity

$$S_{\text{bl}}(f) \approx \begin{cases} \frac{bl^2 w_\infty}{5\pi f} S_p(f) & \text{for} \quad \frac{\pi f l}{w_\infty} \leq 2 \\ \frac{2blw_\infty^2}{5\pi^2 f^2} S_p(f) & \text{for} \quad 2 < \frac{\pi f l}{w_\infty} \leq \frac{15}{\pi} \\ \frac{6bw_\infty^3}{\pi^4 f^3} S_p(f) & \text{for} \quad \frac{15}{\pi} \leq \frac{\pi f l}{w_\infty} \end{cases} \tag{2.15}$$

The needed PSD of the wall S_p is computed with the approximated boundary layer displacement thickness δ^* and an approximation formula $G(\text{St}_{\delta^*})$

$$S_p(f) = \rho^2 w_\infty^3 \delta^* G(\text{St}_{\delta^*}). \tag{2.16}$$

The approximated boundary layer displacement thickness can be estimated with the known relation for a flat plate

$$\frac{\delta^*}{l} \approx 0.05 \, \text{Re}_l^{-0.2}. \tag{2.17}$$

The Strouhal number of the displacement thickness is defined as

$$\text{St}_{\delta^*} = \frac{f\delta^*}{w_\infty}. \tag{2.18}$$

Finally the approximation formula is

$$G(\text{St}_{\delta^*}) = \frac{0.01}{1 + 4.1985\text{St}_{\delta^*} + 0.454\text{St}_{\delta^*}^6}. \tag{2.19}$$

---

[1]Költzsch also provides a prediction for fans in free flow, but only the ducted fan is considered in this work.

By inserting these equations the method of Költzsch gives a spectral noise prediction with sound sources assumed to be the turbulent inlet and the turbulent boundary layer. The noise from vortex shedding at the trailing edge is not take into account in this method.

2.2.3. Stochastic methods

The basic principle of the stochastic methods is to predict far field spectra with statistical information of the source resulting from turbulent flow, and a model for the propagation. Very often the assumption of free radiation is made. Due to the fact that stationary turbulent quantities are used for the sound source, just broadband noise can be predicted. The group of stochastic methods is sometimes located between class 2 and class 3.

One kind of approaches is based on Amiet's theory [7, 8]. The original approach assumes the noise source for trailing edge noise to be the surface pressure spectrum upstream of the trailing edge, which is convected with a certain convection velocity u_c in x direction over the trailing edge at $x = 0$ as shown in Fig. 2.1. The turbulence is assumed to be stationary and
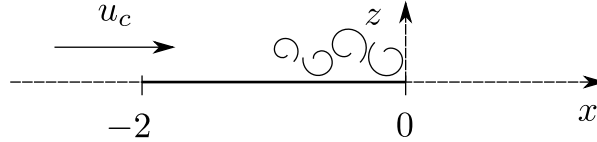

Figure 2.1.: Vortices cause a surface pressure spectrum at the trailing edge.

the solution is derived in a two dimensional half plane. The surface pressure is described in spectral components regarding the convection velocity and the spanwise wave number k_y

$$P = P_0 e^{i[\omega(t - x/u_c) - k_y y]} \,, \tag{2.20}$$

with ω the angular frequency and y the spanwise coordinate. With the assumption of an half infinite plane in the upstream direction, the airfoil response function g can be obtained by the Schwarzschild solution

$$g(\bar{x}, \omega, u_c) = \left((1 + i) E^* \left[-\bar{x}((1 + \mathrm{Ma})\mu + \bar{K}_x) \right] - 1 \right) e^{-i\bar{K}_x x} \,, \qquad -2 < \bar{x} < 0 \tag{2.21}$$

with $K_x = \omega/u_c$, $\mu = \mathrm{Ma}\,\omega\, b/\mathbf{u}\beta^2$, $\beta^2 = 1 - \mathrm{Ma}^2$ and b the semichord which is used to make the bar quantities non-dimensional and the function $E^*(x)$ is

$$E^*(x) = \int\limits_0^x (2\pi\xi)^{-1/2} e^{-i\xi} \,\mathrm{d}\xi \,, \tag{2.22}$$

consists of Fresnel integrals. This solution also satisfies the Kutta condition. After that, the far field spectrum in the $y = 0$ plane can then be computed as an integral solution of the airfoil response function and the surface pressure cross-spectrum $S_{qq}(\omega, y)$

$$S_{pp}(x, 0, z, \omega) = \left(\frac{\omega b z}{2\pi c_0 \sigma^2} \right)^2 l_y(\omega) d |\mathcal{L}|^2 S_{qq}(\omega, 0) \tag{2.23}$$

with $\sigma^2 = x^2 + \beta^2 z^2$, d the span and $l_y(\omega)$ being the spanwise correlation length. For the integral solution the Fresnel integrals

$$|\mathcal{L}| = |\int\limits_{-2}^{0} g(\xi, \omega, u_c) e^{-i\mu\xi(\text{Ma}-x/\sigma)} \, \mathrm{d}\xi| \tag{2.24}$$

have to be solved. The obtained solution gives the spectrum in the half plane. If the turbulent boundary conditions are identical on the top and bottom side, the solution can be multiplied by two, to get the amplitude with sound contribution from upper and lower side. Originally the only flows that were observed well enough to use the pressure spectra were turbulent boundary layers. Nowadays it is easy to generate the turbulent quantities from RANS simulations. Originally this method was only used for the prediction of trailing edge noise, but it can be also used for leading edge noise. The method was improved by different researches over the years. A recent adaption was the introduction of back-scattering correction [95], which was applied to trailing edge noise in [82]. In [23] this method was applied to predict the trailing edge noise of an airfoil under differ angles of attack and compared with measurements. The surface pressure spectrum at the trailing edge was obtained from an LES simulation. In [98] Amiet's theory was applied to predict fan noise. The sources for the broadband noise prediction were obtained by RANS simulations and the acoustic results were compared to other methods.

A simple estimation for surface noise contribution is based on Curle's analogy [24]. It gives the sound power contribution as the surface integral over the acoustic surface intensity I, respectively by an integral over a correlation area A_c and the mean-square time derivative of the surface pressure $\overline{\left(\frac{\partial p}{\partial t}\right)^2}$

$$P = \int\limits_{\Gamma} I \, \mathrm{d}\Gamma = \int\limits_{\Gamma} \frac{A_c}{12\rho_0\pi c_0^2} \overline{\left(\frac{\partial p}{\partial t}\right)^2} \, \mathrm{d}\Gamma \, . \tag{2.25}$$

This quantities can be easily provided by a RANS simulation, and are therefore suited to be used as a first investigation of the surface sound sources. Unfortunately this model gives no information about the incident sound. Therefore the original Curle's analogy has to be solved.

Another estimation of noise contribution in the volume in based on Proudman [90]. The generated acoustic power per unit volume is predicted as

$$P = \alpha\rho_0 \frac{u^3}{l} \frac{u^5}{c_0^5} \tag{2.26}$$

with α a constant, l the integral length scale and $u = \sqrt{2/3k}$ the root mean square of the velocity derived from the turbulent kinetic energy k. In StarCCM+ this is implemented as

$$P = \alpha\rho_0 \frac{U^3}{L} \frac{U^5}{c_0^5} \tag{2.27}$$

with $U = L/T$ the turbulent velocity computed by the turbulent length scale and the turbulent time scale. In the simulations, a default value of $\alpha = 0.629$ is used.

Another kind of noise prediction methods is based on the Stochastic Noise Theory (SNT). In SNT the right hand side of an acoustic analogy is modeled. If the flow quantities of the right hand side are modeled (for example p and $\mathbf{u}$), it is called an "acoustic analogy approach". If the complete right hand side is modeled we call it an "equivalent source approach". Maybe the first to apply a two point correlation to Lighthill's analogy was Ribner [94]. For an arbitrary acoustic analogy with the wave operator $\Box$, the acoustic unknown p' and the source on the right hand side q, one obtains

$$\Box p' = q \,. \tag{2.28}$$

The solution of this linear partial differential equation can be obtained by a convolution with the Green's function[2] $\hat{G}$ (here displayed in the frequency domain)

$$p'(\mathbf{x}, \omega) = \int\limits_{\Omega} \int\limits_{t} \hat{G}(\mathbf{x}, \mathbf{y}, \omega) q(\mathbf{y}, t_1) e^{i\omega t_1} \, \mathrm{d}t_1 \mathrm{d}\Omega \,. \tag{2.29}$$

The solution is evaluated at location $\mathbf{x}$ by integration over the time t and spatial domain Ω. In general this integrals are improper, but in a practical application it is enough to integrate over the region of interest, where the main acoustic sources occur. To obtain the spectrum of the acoustic unknown the two point correlation of this equation is build. This leads to

$$\underbrace{S(\mathbf{x}, \omega)}_{\text{spectrum of } p'} = \int\limits_{\Omega} \int\limits_{\Omega} \int\limits_{t} \underbrace{\hat{G}(\mathbf{x}, \mathbf{y}, \omega) \hat{G}^*(\mathbf{x}, \mathbf{y} + \mathbf{r}, \omega)}_{\text{acoustic propagation}} \times \underbrace{\langle q(\mathbf{y}, t) q(\mathbf{y} + \mathbf{r}, t + \tau) \rangle}_{\text{cross-correlation of the source}} e^{i\omega\tau} \, \mathrm{d}\tau \mathrm{d}\Omega \mathrm{d}\mathbf{r} \,, \tag{2.30}$$

where the acoustic propagation term is known. The cross-correlation of the source has to be modeled for example with empirical values, but the quantities of the acoustic source can be obtained by RANS simulations.

Although in theory this method should be applicable to all kinds of broadband noise (as long as a Green's function can be obtained), it is mainly used for jet-noise. For example in [109] a k-ϵ simulation and the Linearized Euler Equations are used to predict jet mixing noise from fine scale turbulence. In [65] a non causal Green's function and the Lilley equation was used to describe the spectral directivity of a jet.

The next kind of noise prediction methods is working in a very similar way as the SNT. But instead of solving the acoustic propagation with the Green's function in the frequency domain, it is solved in time domain and the right hand side of the acoustic analogy is modeled. These approaches are called stochastic noise source methods. Kraichnan [67] used Fourier modes to build a velocity field so that a turbulence spectrum $E(k)$ is realized. This also satisfies a certain cross-correlation in the physical domain. This was expanded later in the stochastic noise generation and radiation by a space-time evolution of the turbulent field [11]. The velocity field is computed as the sum of N modes

$$\mathbf{u}(\mathbf{x}, t) = 2 \sum_{n=1}^{N} \tilde{u}_n \cos\left[\mathbf{k}_n(x - t\mathbf{u}_c) + \psi_n + \omega_n t\right] \boldsymbol{\sigma}_n \,, \tag{2.31}$$

---

[2]The Green's function has to fulfill certain boundary conditions, which means that free radiation is easy to realize but for arbitrary boundary conditions, e.g. from sound hard walls and complicated geometries, an analytical solution may not be found.

where $\mathbf{u}_c$ is the convective velocity, the vector $\mathbf{k}_n$ is a randomly picked wave vector, ψ_n a randomly picked phase and $\boldsymbol{\sigma}_n$ a vector normal to $\mathbf{k}_n$ to satisfy incompressibility. The amplitude $\tilde{u}_n$ was computed from a modified Von Karman spectrum

$$\tilde{u}_n = \sqrt{E(k_n)\Delta k_n}\,. \tag{2.32}$$

This modeled velocity field was then used to compute the right hand side for the linearized Euler equations (LEE). The mean flow for the LEE was gained by a k-ϵ RANS simulation. The LEE are then solved numerically, so that reflection and convection effects can be taken into account. The propagation is therefore similar to class 3 methods, and the only difference is that the noise sources are modeled.

A different method to obtained the noise sources was introduced as the random particle mesh method in [33]. It is based on a spatial filtering of white noise. This method was improved in [32] and called fast random particle mesh method (FRPM). The FRPM method was adapted for unsteady simulations to predict broadband and tonal noise of a centrifugal fan [47]. This unsteady FRPM uses flow data from an unsteady RANS simulation to compute the source terms. This was combined with a boundary element method to compute the acoustic propagation.

2.3. Class 3 methods

The class 3 methods allow a separation and identification of different noise mechanisms. They use high fidelity information about the flow field which is normally obtained by scale resolving unsteady CFD simulations. The data from the flow field are then used to compute acoustic sources, which feed an acoustic analogy. With this analogy the acoustic propagation is computed. Therefore these methods are also called *hybrid aeroacoustic methods*. The advantage of the hybrid methods is that both, the unsteady CFD simulations and the CAA simulation can be solved individually and adapted to their individual requirements[3]. This methods are not restricted in the application to special geometries and can therefore also be applied to fan noise. Nevertheless, special treatment can be necessary in the numerics to account for the rotation, compared to the standard applications for stationary geometries.

In general the acoustic analogy is a partial differential equation or set of equations that are discretized and solved numerically, but for the standard wave equation (or Helmholtz equation in frequency domain) and free radiation, the solution can be obtained in an explicit integral formulation with the use of a Green's function. This can be used in the Lighthill and Ffowcs-Williams and Hawkings analogy. A special method is the boundary element method [80] where a solution exists in an implicit integral formulation. This method allows the description of reflecting geometry. A less often used method to obtain the far field acoustic is the ray tracing method that is for example applied in [116]. This method describes the acoustic propagation as rays in analogy to optics, which works well for high frequencies and can even be applied

---

[3]Requirements of CFD simulations are resolving of the flow in space and time, which means a refined discretization towards walls to resolve boundary layers and refinements to resolve turbulent structures, as well as a time step that resolves turbulent quantities and accounts for convective effects. Requirements for CAA simulations are resolving the acoustics in space and time, which means a uniform spatial discretization that accounts for the resolution of the acoustic waves in space and time.

to inhomogeneous media, and is also a very fast method. A restriction of this method is that diffraction effects are not described.

A special case is the combination of measurements and numerics. In this case the right hand side of the acoustic analogy is obtained from highly resolved measurement data like, particle image velocimetry. In [42] this method was applied to a rectangular cavity and combined with Curl's acoustic analogy. In [124] it was applied to an airfoil with a Gurney flap and Curl's analogy was used as well. In [75] the method was applied to human phonation using Lighthill's acoustic analogy. The combination of measurements and numerics is still an ongoing research topic, but so far no applications to fan noise are published.

2.3.1. Lighthill

Lighthill's acoustic analogy [73, 74] is one of the most famous ones. Lighthill derived his analogy in a similar way as the acoustic wave equation (see section 3.1.4) from the conservation of mass and the conservation of momentum without external forces in the form:

$$\frac{\partial \rho}{\partial t} + \frac{\partial \rho u_i}{\partial x_i} = 0 \,, \tag{2.33}$$

$$\frac{\partial \rho u_i}{\partial t} + c_0^2 \frac{\partial \rho}{\partial x_i} = -\frac{\partial T_{ij}}{\partial x_j} \,. \tag{2.34}$$

But in contrast to the acoustic wave equation he did not neglect the viscous stress tensor

$$T_{ij} = \rho u_i u_j + (p' - c_0^2 \rho')\delta_{ij} + \tau_{ij} \tag{2.35}$$

with δ_{ij} the Cronecker delta and the fluctuating quantities

$$p' = p - p_0 \,, \quad \rho' = \rho - \rho_0 \,. \tag{2.36}$$

By computing the time derivative of the first and the spatial derivative of the second and combining both, we arrive at Lighthill's equation

$$\frac{\partial^2 \rho'}{\partial t^2} - c_0^2 \nabla \cdot \nabla \rho' = \frac{\partial^2 T_{ij}}{\partial x_i \partial x_j} \,, \tag{2.37}$$

which does not contain the mean values anymore due to the derivation. In this sense the Lighthill stress tensor can be seen as the acoustic source for the acoustic wave equation. The term $\rho u_i u_j$ is often considered the main sound source, the term $(p' - c_0^2 \rho')\delta_{ij}$ results from entropy and the last contribution is simply from the stress tensor. For low Mach number flows, the source is therefore often reduced to

$$T_{ij} \approx \rho_0 u_i u_j \,. \tag{2.38}$$

For (2.37) an integral solution can be obtained with the Green's function. The fluctuating

density in time domain is then obtained by:

$$c_0^2 \rho'(\mathbf{x}, t) = \frac{1}{4\pi} \frac{\partial^2}{\partial x_i \partial x_j} \int_\Omega \frac{T_{ij}\left(\mathbf{y}, t - \frac{|\mathbf{x}-\mathbf{y}|}{c_0}\right)}{|\mathbf{x} - \mathbf{y}|} \, \mathrm{d}\Omega \qquad (2.39)$$

with $\mathbf{x}$ the receiver location and $\mathbf{y}$ the location in the source field Ω. This means that the sum of the fluctuating density at any receiver location consists of the individual source contributions of the whole source domain. To account for the different travel times from the sources to the receiver, the sources have to be evaluated at the retarded time $t - \frac{|\mathbf{x}-\mathbf{y}|}{c_0}$, which makes the evaluation of this integral costly in the time domain. The integral solution is given in [73] in different formulations, e.g. the solution in the far field, where $\mathbf{x} \ll \mathbf{y}$, can be simplified.

Lighthill's acoustic analogy is not restricted in the application, but the integral solution can just describe free radiation. Therefore, it is mostly applied to jet noise. An extension for solid surfaces was proposed by Curle [24]. The even more general FWH method is going to be addressed in section 2.3.2.

2.3.2. Ffowcs-Williams and Hawkings

The aeroacoustic analogy of Ffowcs-Williams and Hawkings (FWH) [118] is probably one of the most used ones for free radiation at the moment. The approach is similar to section 2.3.1, but the basic idea is to introduce an arbitrary surface Γ in the domain. This surface may represent a solid boundary or a transparent surface that covers a body. With this additional surface, the integral solution expands to a volume integral outside the surface and two surface integrals. If the surface represents a transparent surface that covers a body, it is called the hull formulation. The integral solution writes then as:

$$\begin{aligned}
c_0^2 \rho'(\mathbf{x}, t) = & \frac{1}{4\pi} \frac{\partial^2}{\partial x_i \partial x_j} \int_\Omega \left[\frac{T_{ij} J}{r|1 - \mathrm{Ma}_r|} \right] \mathrm{d}\Omega \\
& - \frac{1}{4\pi} \frac{\partial}{\partial x_i} \int_\Gamma \left[\frac{\rho u_i (u_j - v_j) + p'\delta_{ij} + \tau_{ij}}{r|1 - \mathrm{Ma}_r|} \right] n_j A \, \mathrm{d}\Gamma \\
& + \frac{1}{4\pi} \frac{\partial}{\partial t} \int_\Gamma \left[\frac{\rho(u_i - v_i) + \rho_0 v_i}{r|1 - \mathrm{Ma}_r|} \right] n_i \, \mathrm{d}\Gamma
\end{aligned} \qquad (2.40)$$

with J accounting for expansion of the volume, A accounting for expansion of surface, v the velocity of the surface, n the surface normal, r vector from surface to observer and Ma_r the Mach number in the direction of r. The terms in brackets have to be evaluated at retarded time. For solid body movement the surface is constant and therefore the expansion terms simplify to $J = A = 1$. If the surface includes all sources in the domain just the surface integrals are needed. This can simplify the numerical integration and reduce data to be stored.

If the surface is placed directly on top of the physical boundary it is called the surface formulation. Since the flow through the surface is zero or in other words the velocity at the

boundary must be the same as the velocity of the boundary $u = v$, the formulation writes as:

$$c_0^2 \rho'(\mathbf{x}, t) = \frac{1}{4\pi} \frac{\partial^2}{\partial x_i \partial x_j} \int_{\Omega_s} \left[\frac{T_{ij}J}{r|1 - \mathrm{Ma}_r|} \right] \mathrm{d}\Omega$$
$$- \frac{1}{4\pi} \frac{\partial}{\partial x_i} \int_{\Gamma_s} \left[\frac{p'\delta_{ij} + \tau_{ij}}{r|1 - \mathrm{Ma}_r|} \right] n_j A \, \mathrm{d}\Gamma \tag{2.41}$$
$$+ \frac{1}{4\pi} \frac{\partial}{\partial t} \int_{\Gamma_s} \left[\frac{\rho_0 v_i}{r|1 - \mathrm{Ma}_r|} \right] n_i \, \mathrm{d}\Gamma$$

In this formulation it can be seen that the first term of the integral contains sources from vortices in the fluid. The second term contains sources from forces on the surface and the third term contains a contribution from displacement of volume. It can be shown that the first term scales with Ma^8, the second with Ma^6 and the third with Ma^4. Therefore, the volume term is often neglected for low Mach number flows, which brings a significant reduction of storage and computation time.

The integral solution can be simplified for certain assumptions, for example the evaluation of the acoustic pressure in the far field. For low Mach number flow and uniform movement of the surface, the solution of Curl's analogy is obtained. The formulation used in this work is explained in section 4.3.7. The FWH integral solution has the restriction that the integration surface must surround all reflection walls and the mean flow field must be constant or zero.

Although this method is one of the most known ones, it should be mentioned that a first prediction for steady loading noise of fans was already published in 1936 [40] with a publication in English in [41]. With this method tonal noise and its directivity can be predicted.

2.3.3. Perturbation Equations

The perturbation equations are based on a perturbation ansatz. In addition to the splitting of the mean and fluctuating flow quantities,

$$\mathbf{u} = \bar{\mathbf{u}} + \mathbf{u}' \tag{2.42}$$
$$p = \bar{p} + p' \tag{2.43}$$

for example in section 2.3.1 or the Linearized Euler Equations, the fluctuating quantities are further divided in a component describing the flow and a component describing acoustics. The basic idea of this is to obtain acoustic conservation equation with the flow quantities on the right hand side and acoustic quantities as unknowns. There are several publications on the perturbation equations ([45, 85, 101]), but for the sake of compactness it is restricted here to the Acoustic Perturbation Equations (APE) by Ewert [34]. He derived perturbation equations based on flow filtering, to separate mean flow, fluctuating flow quantities and acoustic quantities. In the compressible case this means that the flow field is divided in a solenoidal vortical part (which is acoustically non radiating) and an irrotational acoustical part.

$$\mathbf{u} = \bar{\mathbf{u}} + \mathbf{u}' = \bar{\mathbf{u}} + \mathbf{u}^{\mathrm{v}} + \mathbf{u}^{\mathrm{a}} \tag{2.44}$$
$$p = \bar{p} + p' = \bar{p} + p^{\mathrm{v}} + p^{\mathrm{a}} \tag{2.45}$$

In incompressible flow the solenoidal part is purely incompressible

$$\mathbf{u}^{\mathrm{v}} = \mathbf{u}^{\mathrm{ic}} \tag{2.46}$$

$$p^{\mathrm{v}} = p^{\mathrm{ic}} \,. \tag{2.47}$$

Ewert derived in total four different perturbation equations. The first one (APE1) is a set of equations based on compressible flow data. It uses turbulent fluctuations, entropy inhomogenities and the interaction of mean vorticity and perturbation velocity as acoustic sources. The second one (APE2) is based on incompressible flow. It is the basis of the perturbed convective wave equation, which will be discussed in section 2.3.4. The full set of equations writes as [34]

$$\frac{\partial \rho'}{\partial t} + \nabla \cdot \left(\rho' \bar{\mathbf{u}} + \bar{\rho} \mathbf{u}^{\mathrm{a}} \right) = -\nabla \bar{\rho} \cdot \mathbf{u}^{\mathrm{ic}} \,, \tag{2.48}$$

$$\frac{\partial \mathbf{u}^{\mathrm{a}}}{\partial t} + \nabla \left(\bar{\mathbf{u}} \cdot \mathbf{u}^{\mathrm{a}} \right) + \nabla \left(\frac{p^{\mathrm{a}}}{\bar{\rho}} \right) = \nabla q_{\bar{\omega}} + T' \nabla \bar{s} - \nabla \bar{T} s' \,, \tag{2.49}$$

$$\frac{\partial p^{\mathrm{a}}}{\partial t} - \bar{c}^2 \frac{\partial \rho'}{\partial t} = -\bar{\rho} \frac{\partial \Phi}{\partial t} + \frac{\gamma \bar{p}}{c_{\mathrm{p}}} \frac{\partial s'}{\partial t} \,. \tag{2.50}$$

The acoustic sources on the right hand side of (2.48) is from fluctuations of the velocity field. For (2.49), the first term on the right hand side $q_{\bar{\omega}}$ is a function of vorticity and acoustic velocity and the second and third term are fluctuations of entropy s and temperature T. In (2.50) the first source term arises from turbulent fluctuations and has to be computed by a Poisson problem. The second term arises from the heat release with the specific heat capacity c_{p} and the heat capacity ratio γ. For vortex sound sources from incompressible pressure all sources disappear for low Mach number flow and the first source term of (2.50) can be approximated by the pressure fluctuation and the set of equation writes as [34]

$$\frac{\partial \rho'}{\partial t} + \nabla \cdot \left(\rho' \bar{\mathbf{u}} + \bar{\rho} \mathbf{u}^{\mathrm{a}} \right) = 0 \,, \tag{2.51}$$

$$\frac{\partial \mathbf{u}^{\mathrm{a}}}{\partial t} + \nabla \left(\bar{\mathbf{u}} \cdot \mathbf{u}^{\mathrm{a}} \right) + \nabla \left(\frac{p^{\mathrm{a}}}{\bar{\rho}} \right) = 0 \,, \tag{2.52}$$

$$\frac{\partial p^{\mathrm{a}}}{\partial t} - \bar{c}^2 \frac{\partial \rho'}{\partial t} = -\frac{\partial p^{\mathrm{ic}}}{\partial t} \,. \tag{2.53}$$

The third perturbation equations (APE3) are derived so that the acoustic variable is perturbed total enthalpy. This formulation is designed so that no Poisson problem has to be solved, to reduce computational effort. The fourth equations (APE4) use a vortex source term based on the Lamb vector.

2.3.4. Perturbed Convective Wave Equation

The Perturbed Convective Wave Equation (PCWE) [52, 62] is an exact reformulation of the APE2 equations as wave equation. Therefore, it uses the same splitting of the acoustic vari-

ables, but as the acoustic unknown the scalar acoustic potential

$$\mathbf{u}^{\mathrm{a}} = -\nabla \phi^{\mathrm{a}} \tag{2.54}$$

is used. With the acoustic potential, the PCWE can be written as:

$$\frac{1}{c_0^2} \frac{D^2 \phi^{\mathrm{a}}}{Dt^2} - \nabla \cdot \nabla \phi^{\mathrm{a}} = -\frac{1}{\rho_0 c_0^2} \frac{Dp^{\mathrm{ic}}}{Dt} \,. \tag{2.55}$$

The source term of this equation is the substantial derivative of the incompressible pressure, with the substantial derivative using the mean flow $\bar{\mathbf{u}}$

$$\frac{D}{Dt} = \frac{\partial}{\partial t} + \bar{\mathbf{u}} \cdot \nabla \,. \tag{2.56}$$

For rotating regions this velocity has to be corrected by the rotational velocity $\mathbf{u}_{\mathrm{r}}$ of the mesh.

$$\frac{D}{Dt} = \frac{\partial}{\partial t} + (\bar{\mathbf{u}} - \mathbf{u}_{\mathrm{r}}) \cdot \nabla \tag{2.57}$$

By the substantial derivative convective effects can be taken into account. But for low Mach numbers this effects are small and may be neglected. The acoustic pressure can be derived from the acoustic potential as a postprocessing step by

$$p^{\mathrm{a}} = \rho_0 \frac{D\phi^{\mathrm{a}}}{Dt} \,. \tag{2.58}$$

The PCWE has a reduced computational effort compared to the acoustic perturbation equations, since it is a single scalar equation. Therefore the computational operations to solve this equation and the memory for the system matrices is smaller. Furthermore it has just a scalar source term, which reduces the amount of storage for the CFD results. Due to the same splitting of variables in acoustic and flow quantities, the acoustic result can also be evaluated in the flow region, where acoustic and hydrodynamic quantities are superposed. The form of the PCWE as wave equation is appropriate to be solved by the finite element method (FEM). This equation is implemented in the research code Coupled Field Systems (CFS++) [60]. In contrast to wave equations, conservation equations are more difficult to solve with FE. This method was already successfully applied to fans in [53, 63]. In [61] a comparison of this acoustic analogy to other methods was applied to the sound radiated from a cylinder in a cross flow. It was also compared to Lighthill's analogy for the prediction of a radial fan in [110].

2.4. Class 4 methods

The class 4 methods base on the full resolution of all hydrodynamic and acoustic components of the compressible flow. This means that no modeling assumptions, except turbulence modeling, have to be made. Therefore, they are also called *direct acoustic simulations*. This also means, that hydrodynamic and acoustic fluctuations are superposed and can't be distinguished offhand. In regions with hydrodynamic fluctuations, the separation is possible with a splitting by wave numbers. The other possibility is to evaluate the acoustic fluctuations just outside the

flow region. For further acoustic propagation in the farfield, often FWH or Kirchhoff integrals are used. For the computations high fidelity simulations are needed to resolve the fluctuating quantities. Often large eddy simulations (LES) or detached eddy simulations (DES) are used. The high fidelity is not only needed to resolve the turbulence. It is also needed to resolve the small amplitudes of the acoustic fluctuations, which are orders of magnitude smaller than the hydrodynamic fluctuations. Furthermore, this small fluctuations have to be preserved to a propagation point where they can be evaluated. And finally the numerical scheme has to prevent dispersion in the wave propagation.

Since this methods include all compressible effects, the back coupling of the acoustics on the flow is also included. This is relevant for the simulation of acoustic feedback loops, where the acoustic waves perturb the original flow field and lead to turbulences, that again lead to the self sustaining acoustic loop. This feedback loops are well known for airfoil self noise (for example [10]), but it was also found to occur on a model of a side mirror [39]. The effect was found by a high order Discontinuous Galerkin LES simulation of the compressible flow around the mirror. The application of direct acoustic simulations is not restricted in Mach number, therefore they can be used to simulate sub- and supersonic flow. This makes it possible to use them for example for jet noise prediction. In [9] a subsonic jet with Ma = 0.75 was simulated with an LES simulation and for the farfield acoustics the propagation was computed with a Kirchhoff integral. In [71] a supersonic jet with Ma = 1.58 was simulated and screech noise investigated by a modal decomposition.

A recent development is that the direct acoustic simulation is also applied to low Mach number flows, where some years ago just methods of class 3 were used. The used algorithms are mainly based on the Lattice Boltzmann Method (LBM), which can be highly parallelized. For an introduction to LBM it is referred to [120]. In [119] this method was applied to self noise of a NACA 6512-63 airfoil at Ma = 0.25. For the application to fan noise several papers were published over the last years [77, 88, 89, 91]. These simulations were computed on several hundred to several thousand CPUs, for which a massive parallel computation environment is needed. This makes the application difficult and restricts it nowadays to research purposes.

Governing equations

In this section the physical basics of flow and sound, which are used in this work, are given. Furthermore, some considerations about the numerical application of the basic equations are discussed later on.

3.1. Physical basics of flow and sound

The basis for fluid dynamics are the conservation equations for mass, momentum and energy. For a Newtonian fluid (like air), this leads to the set of equations, called the flow equations. For the case of low Mach number flows, and a non reacting medium, the conservation of energy can be neglected. These conditions are satisfied for the applications in this work. Therefore, it is not going to be addressed here. For a detailed derivation of the flow equations it is referred to [26]. The flow equations not only describe flow, but inherently describe acoustics in the form of density and pressure fluctuations. From the compressible flow equations the linear acoustic wave equation can be derived as shown in section 3.1.4.

From dimensional analysis of the flow, the characteristic time period T, which is relevant for periodic processes, is related to a characteristic length L and the characteristic flow velocity $\bar{u}$

$$T \propto \frac{L}{\bar{u}} \,. \tag{3.1}$$

This leads to an inverse proportionality of the wave length λ to the Mach number Ma [28]

$$\lambda = c_0 T \propto c_0 \frac{L}{\bar{u}} = \frac{L}{\text{Ma}} \,, \tag{3.2}$$

where the Mach number describes the relation of the characteristic flow velocity $\bar{u}$ to the speed of sound c_0

$$\text{Ma} = \frac{\bar{u}}{c_0} \,. \tag{3.3}$$

This means that for small Mach numbers, the acoustic wave length is much larger than the characteristic length of the flow

$$\lambda \gg L \,. \tag{3.4}$$

This is called the disparity of scales. The disparity also occurs in the propagation velocities. The acoustic waves propagate with the speed of sound, whereas the hydrodynamical quantities propagate with a velocity in the order of the mean flow. Exactly this relation is expressed by the Mach number. The disparity of scales also occurs in the amplitude of flow and acoustic quantities. The audible acoustic pressure is in the range of $20\,\mu\mathrm{Pa}$ to $\approx 200\,\mathrm{Pa}$, where the atmospheric pressure alone is $101300\,\mathrm{Pa}$ on sea level.

This disparity of scales motivates the treatment of flow and acoustics in separate ways. For the numerical treatment of low Mach number flow the assumption of completely incompressible flow equations is beneficial. On the other hand the assumption of purely linear acoustics is beneficial for the acoustic computations, which are descried in the following sections.

3.1.1. Conservation of mass

The conservation of mass states, that the total mass of a body is constant and therefore does not change over time

$$\frac{\mathrm{d}m}{\mathrm{d}t} = 0 \,. \tag{3.5}$$

This holds true for a small volume element of the body where the mass is δm, as long as the continuum theory can be applied

$$\frac{\mathrm{d}\delta m}{\mathrm{d}t} = 0 \,. \tag{3.6}$$

To obtain an equation in field variables, the mass can be expressed as the product of density and volume $\delta \mathrm{V}$ of the element

$$\frac{\mathrm{d}\rho\delta \mathrm{V}}{\mathrm{d}t} = 0 \,. \tag{3.7}$$

The total derivative leads to the conservation of mass in the well known form:

$$\frac{\partial \rho}{\partial t} + \frac{\partial \left(\rho u_i\right)}{\partial x_i} = 0 \,. \tag{3.8}$$

This equation states, that the change of density over time, the change in density and velocity due to convection has to be zero. For an incompressible flow with $\rho = \rho_0 = \mathrm{const.}$ the derivative of the density vanish and this equation can be simplified to

$$\frac{\partial u_i}{\partial x_i} = 0 \,. \tag{3.9}$$

From (3.9) it can be seen, that the velocity field of an incompressible flow has to be divergence free.

3.1.2. Conservation of momentum

The conservation of momentum states that changes of the momentum δI_i arise from external forces f_i

$$\frac{\mathrm{d}\delta I_i}{\mathrm{d}t} = f_i \,. \tag{3.10}$$

The left hand side can be expressed in the field variables mass and velocity as

$$\frac{\mathrm{d}\delta I_i}{\mathrm{d}t} = \frac{\mathrm{d}}{\mathrm{d}t}\left(\delta m u_i\right) = \delta m \frac{\mathrm{d}u_i}{\mathrm{d}t} + u_i \frac{\mathrm{d}\delta m}{\mathrm{d}t}\,, \tag{3.11}$$

where the second term is zero because of (3.5), which leads with $\delta m = \rho \delta V$ to

$$\frac{\mathrm{d}\delta I_i}{\mathrm{d}t} = \rho \delta V \left(\frac{\partial u_i}{\partial t} + u_i \frac{\partial u_i}{\partial x_i}\right)\,. \tag{3.12}$$

The external forces consist of surface forces S, molecular momentum transport I_M and mass forces M

$$f_i = \sum \delta S_i + \frac{\mathrm{d}}{\mathrm{d}t}\delta I_{\mathrm{M}i} + \sum \delta M_i \,. \tag{3.13}$$

The mass forces can be written with the density, volume and g the acceleration

$$\delta M_i = \rho \delta V g_i \,. \tag{3.14}$$

The surface forces can be written as the difference of the pressure on both sides of the volume element

$$\delta S_i = -p(x_i)(-|\delta\Gamma_i|) - p(x_i + \delta x_i)(|\delta\Gamma_i|) \tag{3.15}$$

with the surface size $\delta\Gamma$. A Taylor expansion and neglecting of higher order terms leads to

$$\delta S_i = -\frac{\partial p}{\partial x_i}\delta V \,. \tag{3.16}$$

The forces due to molecular momentum transport entering in i direction and acting in j direction can be written as

$$\frac{\mathrm{d}}{\mathrm{d}t}\delta I_{\mathrm{M}i} = -\tau_{ij}(x_j)(-|\delta\Gamma_i|) - \tau_{ij}(x_j + \delta x_j)(|\delta\Gamma_j|) \,. \tag{3.17}$$

Again a Taylor expansion leads to the relation

$$\frac{\mathrm{d}}{\mathrm{d}t}\delta I_{\mathrm{M}i} = -\frac{\partial \tau_{ij}}{\partial x_j}\delta V \,. \tag{3.18}$$

If all the relations are inserted, the well known conservation of momentum equation is obtained by a division of δV

$$\rho\left(\frac{\partial u_j}{\partial t} + u_i \frac{\partial u_j}{\partial x_i}\right) = -\frac{\partial p}{\partial x_j} - \frac{\partial \tau_{ij}}{\partial x_i} + \rho g_j \,. \tag{3.19}$$

3.1.3. Navier-Stokes equations

To solve the conservation of momentum, information about the stress tensor is needed. For a Newtonian fluid, where the shear stress is a linear function of the shear rate and the viscosity, the shear tensor can be written in terms of the velocity and the dynamic viscosity μ

$$\tau_{ij} = -\mu \left(\frac{\partial u_j}{\partial x_i} + \frac{\partial u_i}{\partial x_j} \right) + \frac{2}{3} \delta_{ij} \mu \frac{\partial u_k}{\partial x_k} \, . \tag{3.20}$$

With (3.8) and (3.19) this forms a set of equations, which is called the compressible flow equations. This set of four equations has the five unknowns ρ, p and the three components of u_i, so an additional equation is needed. This problem is the so called closure problem. For compressible flows this can be achieved with the additional conservation of energy and an equation of state for the fluid.

For the special case of incompressible flow with a constant density and a constant viscosity $\mu = \mu_0 = \text{const.}$ this can be further simplified to

$$\rho_0 \left(\frac{\partial u_j}{\partial t} + u_i \frac{\partial u_j}{\partial x_i} \right) = -\frac{\partial p}{\partial x_j} + \mu_0 \frac{\partial^2 u_j}{\partial x_i^2} + \rho_0 g_j \, . \tag{3.21}$$

With eq. (3.9) the incompressible flow equations are formed. This set of four equations has just the four unknowns p and the three components of u_i. Therefore, this can directly be applied to model flow. The assumption of constant density and constant viscosity is often valid for low Mach number flows.

The assumption of an ideal fluid with no molecular momentum transport, leads to a simplification of (3.19)

$$\rho \left(\frac{\partial u_j}{\partial t} + u_i \frac{\partial u_j}{\partial x_i} \right) = -\frac{\partial p}{\partial x_j} + \rho g_j \, . \tag{3.22}$$

With (3.8) this forms the Euler equations. They are used as a starting point for some acoustic analogies.

3.1.4. Acoustic Wave Equation

For an ideal gas, the relation between pressure and density is temperature dependent

$$p = \rho RT \tag{3.23}$$

with the gas constant R. Acoustics is defined as isentropic. The relation between speed of sound, pressure and density is therefore

$$c^2 = \left. \frac{\partial p}{\partial \rho} \right|_{ds=0} = \kappa \frac{p}{\rho} = \kappa RT \tag{3.24}$$

with κ the adiabatic exponent. For standard values of $\kappa = 1.4$ and $T = 20°C$ a speed of sound of $c = 343\,\mathrm{m/s}$ can be computed. For linear acoustics, this relation can be simplified to

$$c_0^2 = \frac{p^a}{\rho^a}\,. \tag{3.25}$$

The acoustic equations can be derived from (3.8) and (3.22) by neglecting the volume forces

$$\frac{\partial \rho}{\partial t} + \frac{\partial (\rho u_i)}{\partial x_i} = 0\,, \tag{3.26}$$

$$\rho \left(\frac{\partial u_j}{\partial t} + u_i \frac{\partial u_j}{\partial x_i} \right) = -\frac{\partial p}{\partial x_j}\,. \tag{3.27}$$

A splitting in mean and acoustic (respectively fluctuating) quantities leads to (for simplicity the mean flow is neglected)

$$\frac{\partial(\rho_0 + \rho^a)}{\partial t} + \frac{\partial \left((\rho_0 + \rho^a)u_i^a\right)}{\partial x_i} = 0\,, \tag{3.28}$$

$$(\rho_0 + \rho^a) \left(\frac{\partial u_j^a}{\partial t} + u_i^a \frac{\partial u_j^a}{\partial x_i} \right) = -\frac{\partial(p_0 + p^a)}{\partial x_j}\,. \tag{3.29}$$

The derivatives of the mean quantities are zero and second order terms are neglected to derive a linear system of equations:

$$\frac{\partial \rho^a}{\partial t} + \rho_0 \frac{\partial u_i^a}{\partial x_i} = 0\,, \tag{3.30}$$

$$\rho_0 \frac{\partial u_j^a}{\partial t} + \frac{\partial p^a}{\partial x_j} = 0\,. \tag{3.31}$$

This first order system in time describes linear acoustics sufficiently. Nevertheless, it is often rewritten to obtain the actual wave equation. Therefore, the time derivative of the first equation and the spatial derivative of the second equation is derived. With the acoustic relation (3.25) this set of equations can be rewritten in a second order form as the acoustic wave equation:

$$\frac{\partial^2 p^a}{\partial t^2} - c_0^2 \frac{\partial^2 p^a}{\partial x_j^2} = 0\,. \tag{3.32}$$

3.2. Towards numerics

To solve (3.32) numerically, the Finite Element (FE) method is used. This method solves the equation in a weak form. Therefore the equation is multiplied with a test function φ and integrated over the computation domain Ω

$$\int_\Omega \varphi \frac{\partial^2}{\partial t^2} p^a \, \mathrm{d}\Omega - c_0^2 \int_\Omega \varphi \frac{\partial^2}{\partial x_i^2} p^a \, \mathrm{d}\Omega = 0\,. \tag{3.33}$$

To reduce the order of spatial derivatives it is integration by parts, which gives an additional integral over the surface of the domain Γ with normal vector n_i

$$\int_\Omega \varphi \frac{\partial^2}{\partial t^2} p^{\mathrm{a}} \, \mathrm{d}\Omega + c_0^2 \int_\Omega \frac{\partial}{\partial x_i} \varphi \frac{\partial}{\partial x_i} p^{\mathrm{a}} \, \mathrm{d}\Omega - c_0^2 \int_\Gamma \varphi \frac{\partial}{\partial n} p^{\mathrm{a}} \, \mathrm{d}\Gamma = 0 \,. \tag{3.34}$$

For simplicity the normal derivative of the boundary integral is written as

$$\frac{\partial}{\partial n} = \frac{\partial}{\partial x_i} \cdot n_i \,. \tag{3.35}$$

This boundary integral is used to incorporate boundary conditions in the simulations. For sound hard walls, this integral has to be zero. This can be seen from (3.31) as the acoustic velocity has to be zero at the wall. To obtain a spatially discretized form, the continuous unknown pressure and test function are approximated by the discrete sum of spatial dependent basis functions $N(x)$ and weights p_k^{a} and φ_l

$$p^{\mathrm{a}} \approx p^{\mathrm{a}h} \quad = \quad \sum_{k=1}^{n} N_k(x) p_k^{\mathrm{a}} \,, \tag{3.36}$$

$$\varphi \approx \varphi^h \quad = \quad \sum_{l=1}^{n} N_l(x) \varphi_l \,, \tag{3.37}$$

with n the number of unknowns. Substitution (3.36) and (3.37) in (3.34) gives the semi discrete Galerkin formulation, still continuous in time

$$\begin{aligned}
\int_\Omega \sum_{l=1}^{n} N_l \varphi_l \sum_{k=1}^{n} N_k \frac{\partial^2}{\partial t^2} p_k^{\mathrm{a}} \, \mathrm{d}\Omega + c_0^2 \int_\Omega \sum_{l=1}^{n} \frac{\partial}{\partial x_i} N_l \varphi_l \sum_{k=1}^{n} \frac{\partial}{\partial x_i} N_k p_k^{\mathrm{a}} \, \mathrm{d}\Omega \\
- c_0^2 \int_\Gamma \sum_{l=1}^{n} N_l \varphi_l \sum_{k=1}^{n} \frac{\partial}{\partial n} N_k p_k^{\mathrm{a}} \, \mathrm{d}\Gamma = 0
\end{aligned} \tag{3.38}$$

and the permutation of sums and integrals finally results in

$$\begin{aligned}
\sum_{l=1}^{n} \varphi_l \left(\sum_{k=1}^{n} \left(\frac{\partial^2}{\partial t^2} p_k^{\mathrm{a}} \int_\Omega N_l N_k \, \mathrm{d}\Omega + c_0^2 p_k^{\mathrm{a}} \int_\Omega \frac{\partial}{\partial x_i} N_l \frac{\partial}{\partial x_i} N_k \, \mathrm{d}\Omega \right) \right) \\
- c_0^2 \sum_{l=1}^{n} \varphi_l \left(\sum_{k=1}^{n} p_k^{\mathrm{a}} \int_\Gamma N_l \frac{\partial}{\partial n} N_k \, \mathrm{d}\Gamma \right) = 0 \,.
\end{aligned} \tag{3.39}$$

3.2.1. Effects of rotating domains

When rotating systems should be treated numerically, there are some special things to be considered. First of all, the numerical treatment depends on the modeling of time. If just an averaged result quantity is needed, the velocity in the rotating domain can be modeled as a relative velocity to a reference frame. This can be applied to RANS simulations, to obtain

an averaged flow field of the rotating domain. If the simulation is time dependent, a real motion of the mesh has to be done. This means in general, that the simulation setup consists of stationary and rotating domains, and mesh interfaces have to be used. Furthermore, the velocity defined on the grid is no longer the absolute velocity **u**, since the grid is moving itself with the grid velocity $\mathbf{u}_\mathrm{g}$. The convective velocity $\mathbf{u}_\mathrm{c}$ is then obtained by

$$\mathbf{u}_\mathrm{c} = \mathbf{u} - \mathbf{u}_\mathrm{g} \,. \tag{3.40}$$

For purely rotational movement of the mesh, the grid velocity reduces to the cross product of the rotational velocity $\boldsymbol{\omega}$ and radius from the rotational axis **r**

$$\mathbf{u}_\mathrm{g} = \boldsymbol{\omega} \times \mathbf{r} \,. \tag{3.41}$$

In StarCCM+, the velocity in the conservation equations is therefore corrected in the convective terms. This introduces additional flux terms, which are called grid fluxes.

In CFS++ this is done by an Arbitrary Lagrangian Eulerian (ALE) framework [25]. The Eulerian description uses a stationary reference system, in StarCCM+ called the laboratory reference frame. The motions and deformations of the material are observed relatively to the discretized reference system. This description of the system is suited to observe physical effects at certain spatial locations and is mainly used in fluid mechanics. The Lagrangian description uses a reference system bound to the material. It is therefore moving and deforming with the material, like a moving observer. This has the advantage to describe the behavior of certain material point, which is often applied in mechanics. The ALE formulation describes the system in an independent reference frame, which neither has to be stationary nor bound to the material. The three descriptions can be transformed into each other, but the substantial derivative depends on the actual reference system. In the Lagrangian description, the substantial derivative is simply the time derivative. In the Eulerian description, the substantial derivative is the time derivative with a convective change. In the ALE description, the substantial derivative is the time derivative with a convective change dependent on the convective velocity of (3.40).

The connection of rotating and stationary meshes can either be achieved with overlaying meshes, or so called chimera meshes [12]. They use a background mesh for the stationary domain, and overlay a mesh adapted to the moving geometry. In the simulation an interpolation between these two (or more) meshes is done. This method is often used for the simulations of helicopters, open rotors or moving wing flaps. The advantage of this method is that arbitrary movement can be modeled where on the down side the computational effort is larger compared to the sliding interface techniques. The sliding interface technique combines different meshes on surface regions, with a nonconforming interface (for example [36]). To realize mesh movement (without further manipulation of the volume meshes), just transversal or rotational movement can be realized. In practice this leads mostly to flat or cylindrical interfaces. In [38] a comparison is shown of these two methods for the simulation of an open rotor.

In CFS++ a sliding mesh interface is implemented. It uses a Nitsche type mortaring [44]. For two domains Ω_1 and Ω_2 connected with a common interface Γ_I, (3.34) can be written as

$$\int_{\Omega_1} \varphi_1 \frac{1}{c_0^2} \frac{\partial^2 p_1^\mathrm{a}}{\partial t^2} \, \mathrm{d}\Omega + \int_{\Omega_1} \frac{\partial}{\partial x_i} \varphi_1 \frac{\partial}{\partial x_i} p_1^\mathrm{a} \, \mathrm{d}\Omega - \int_{\Gamma_\mathrm{I}} \varphi_1 \frac{\partial p_1^\mathrm{a}}{\partial n_\mathrm{I}} \, \mathrm{d}\Gamma = 0 \tag{3.42}$$

and

$$\int_{\Omega_2} \varphi_2 \frac{1}{c_0^2} \frac{\partial^2 p_2^{\mathrm{a}}}{\partial t^2} \, \mathrm{d}\Omega + \int_{\Omega_2} \frac{\partial}{\partial x_i} \varphi_2 \frac{\partial}{\partial x_i} p_2^{\mathrm{a}} \, \mathrm{d}\Omega + \int_{\Gamma_{\mathrm{I}}} \varphi_2 \frac{\partial p_2^{\mathrm{a}}}{\partial n_{\mathrm{I}}} \, \mathrm{d}\Gamma = 0 \; . \tag{3.43}$$

Since a unique normal vector n_{I} is used, the sign of one surface term is inverted. A physical requirement at the interface is the equality of the velocity in normal direction, which results in the normal derivative of p^{a} in region Ω_1 and Ω_2

$$\frac{\partial p_1^{\mathrm{a}}}{\partial n_{\mathrm{I}}} = \frac{\partial p_2^{\mathrm{a}}}{\partial n_{\mathrm{I}}} \; . \tag{3.44}$$

By adding (3.42) and (3.43) and taking into account (3.44) the integral over Γ_{I} reads as follows

$$\int_{\Gamma_{\mathrm{I}}} (\varphi_2 - \varphi_1) \frac{\partial p_1^{\mathrm{a}}}{\partial n_{\mathrm{I}}} \, \mathrm{d}\Gamma \; . \tag{3.45}$$

Equation (3.45) leads to an asymmetric system matrix and therefor an additional term is added to restore the symmetry in the equation system

$$\int_{\Gamma_{\mathrm{I}}} \frac{\partial \varphi_1}{\partial n_{\mathrm{I}}} (p_1^{\mathrm{a}} - p_2^{\mathrm{a}}) \, \mathrm{d}\Gamma = 0 \, , \tag{3.46}$$

which has to be zero as the pressure on both sides of the interface has to be equal. To ensure the continuity at the interface an additional penalty term is added for every intersection element E_I to stabilize the numerical scheme

$$\beta \sum_{E_{\mathrm{I}}} \frac{1}{h_E} \int_{E_{\mathrm{I}}} (\varphi_1 - \varphi_2)(p_1^{\mathrm{a}} - p_2^{\mathrm{a}}) \, \mathrm{d}\Gamma = 0 \, . \tag{3.47}$$

This term is scaled by the size of the intersecting elements h_E and a penalty factor β. For further description of the implementation and the choice of the penalty factor see [52].

3.2.2. Turbulence modeling

For most technical applications it can be assumed that the flow is turbulent. Turbulent flows are highly three dimensional and have different ranges of scales in time, amplitude and space. To solve the incompressible flow equations with no further physical modeling, the time and spatial discretization, means to perform a direct numerical simulation (DNS). But in general the effort to resolve all necessary scales is very high, and restricts the application of DNS simulations to low Re-numbers or laminar flows. To overcome this limitation, the complexity of the simulations is reduced by physical models. This is referred to as turbulence modeling. With every model a certain amount of information is lost, but result detail and computational effort is always a trade-off. Maybe the most fundamental modeling approach is the Reynolds averaging. Reynolds' basic idea was to split the unknown quantities in an averaged (and

therefore time independent) and a fluctuating part

$$u_i = \bar{u}_i + u'_i, \quad p = \bar{p} + p', \quad \rho = \bar{\rho} + \rho'. \tag{3.48}$$

For incompressible simulations the density is constant and therefore

$$\rho = \bar{\rho}. \tag{3.49}$$

With this splitting, the flow equations can be written as (for simplicity the gravity is neglected here)

$$\frac{\partial \bar{u}_i}{\partial x_i} = 0, \tag{3.50}$$

$$\bar{\rho} \left(\frac{\partial \bar{u}_i}{\partial t} + \bar{u}_i \frac{\partial \bar{u}_j}{\partial x_i} \right) = -\frac{\partial \bar{p}}{\partial x_j} + \frac{\partial}{\partial x_i} \left(\mu \frac{\partial \bar{u}_j}{\partial x_i} - \bar{\rho} \overline{u'_i u'_j} \right). \tag{3.51}$$

For a large enough averaging time the mean flow becomes constant and the time derivative vanishes

$$\bar{\rho} \bar{u}_i \frac{\partial \bar{u}_j}{\partial x_i} = -\frac{\partial \bar{p}}{\partial x_j} + \frac{\partial}{\partial x_i} \left(\mu \frac{\partial \bar{u}_j}{\partial x_i} - \bar{\rho} \overline{u'_i u'_j} \right). \tag{3.52}$$

On the right hand side of (3.52) the term $\mu \frac{\partial \bar{u}_j}{\partial x_i}$ describes the laminar stress tensor and the term $-\bar{\rho} \overline{u'_i u'_j}$ describes the turbulent stress tensor or Reynolds stress tensor, with the entries

$$\overline{u'_i u'_j} = \begin{pmatrix} \overline{u_1'^2} & \overline{u'_1 u'_2} & \overline{u'_1 u'_3} \\ \overline{u'_2 u'_1} & \overline{u_2'^2} & \overline{u'_2 u'_3} \\ \overline{u'_3 u'_1} & \overline{u'_3 u'_2} & \overline{u_3'^2} \end{pmatrix}. \tag{3.53}$$

The trace of this tensor describes the turbulent kinetic energy

$$k = \frac{1}{2} \left(\overline{u_1'^2} + \overline{u_2'^2} + \overline{u_3'^2} \right). \tag{3.54}$$

The Reynolds stress tensor is symmetric and leads to six additional unknowns. Since the equation system still consists of four equations, the system is not closed and it can not be solved directly. A basic task of the turbulence modeling is to find a model for this Reynolds stress tensor.

A common assumption is to describe the transport of turbulence similarly to the molecular transport, which is called Boussinesq ansatz

$$\bar{\rho} \overline{u'_i u'_j} = -\bar{\rho} \nu_{\mathrm{t}} \left(\frac{\partial \bar{u}_j}{\partial x_i} + \frac{\partial \bar{u}_i}{\partial x_j} \right) \tag{3.55}$$

with the turbulent viscosity

$$\nu_{\mathrm{t}} = \mu_{\mathrm{t}} / \bar{\rho}, \tag{3.56}$$

this can be rewritten as a definition for the turbulent viscosity

$$\nu_{\mathrm{t}} = \frac{\overline{u_i' u_j'}}{\left(\frac{\partial \bar{u}_j}{\partial x_i} + \frac{\partial \bar{u}_i}{\partial x_j}\right)} \, . \tag{3.57}$$

Since the turbulent viscosity is herein modeled as a scalar, this means the modeled turbulence is isotropic. This turbulent viscosity is proportional to a characteristic velocity u_c and characteristic length l_c

$$\nu_{\mathrm{t}} \propto u_c l_c \, . \tag{3.58}$$

There are many different turbulent viscosity models available in literature [117]. The first three are based on the Boussinesq assumption and model the turbulent viscosity in different ways. They are often classified as:

Algebraic models

Algebraic models use an analytical approach to model the turbulent viscosity ν_{t}. Other algebraic models use the mixing length as turbulent quantity.

One equation models

One equation models use an analytical model for the characteristic length and an own transport equation for the turbulent kinetic energy. A famous model of this category is the Spalart-Allmaras (SA) model [106], with certain extensions of it.

Two equation models

Two equation models use additional transport equation for the characteristic length and the turbulent kinetic energy. The most famous model are the k-ϵ-model, where the energy dissipation rate ϵ is used as a second transport equation and the $k - \omega$-model, where the specific dissipation rate ω is used as a second transport equation.

Stress transport models

The stress transport models do not rely on the Boussinesq assumption but use transport equations for the turbulent stress tensor. Due to the increase in additional quantities, this models need more computational effort. According to [117], this methods are better suited to predict flows with sudden changes in mean strain rate, flow over curved surfaces, flow in ducts with secondary motion, flow in rotating fluids and three-dimensional flow.

Large eddy simulations (LES)

The large eddy simulations are based on the assumption that the large scale turbulence is anisotropic, but the small scale turbulence is isotropic. Therefore the LES simulations separate the large scale flow quantities $\bar{f}_{(r,t)}$ turbulences from smaller ones $f'_{(r,t)}$

$$f_{(r,t)} = \bar{f}_{(r,t)} + f'_{(r,t)} \, . \tag{3.59}$$

The turbulence of the large scales is resolved in the LES simulation and the smaller scale turbulences are modeled. The separation between the resolved large scales and the unresolved small or so called subgrid-scale is done by a spatial filtering, which can be written as an convolution integral

$$\bar{f}_{(r,t)} = \int_{\Omega} G_{(r,r',\Delta)} f_{(r',t)} \, \mathrm{d}\Omega' \tag{3.60}$$

with filter function G and filter width Δ. Smagorinsky was the first to provided a model for the subgrid stresses [105]. He modeled the subgrid turbulent stress tensor with the strain rate tensor of the resolved velocities

$$\tau_{ij} = 2\nu_{\mathrm{t}} S_{ij} \tag{3.61}$$

with

$$S_{ij} = \frac{1}{2} \left(\frac{\partial \bar{u}_i}{\partial x_j} + \frac{\partial \bar{u}_j}{\partial x_i} \right). \tag{3.62}$$

The turbulent viscosity also called Smagorinsky eddy viscosity itself is modeled with a constant C_s, the grid size and the strain rate

$$\nu_{\mathrm{t}} = (C_s \Delta)^2 |S_{ij}|. \tag{3.63}$$

According to the literature, the constant is supposed to be $0.1 \leq C_s \leq 0.24$. For applications of the LES method and comparison with DNS simulations see for example [17].

Detached eddy simulations (DES)

A drawback of the LES simulations is the increased computational effort. Especially to resolve boundary layers and shear flow, the mesh has to be refined drastically. The detached eddy simulations combine LES and RANS simulation to reduce the computational effort of the LES simulations. The RANS simulation is used to compute the boundary layer and the LES is used to resolve the large eddies in the free flow.

The DES models can differ in the used RANS model and the way they switch from one model to the other, which is commonly described as the "blending function". In StarCCM+ there are methods based on the Spalart-Allmaras model implemented. The Spalart-Allmaras delayed detached eddy simulation (DDES) is based on [107]. The default model is the improved delayed detached eddy simulation (IDDES), which is also used in this work, uses a formulation of [103]. Computational more expensive are the k-ω SST models. The available k-ω SST DDES model is based on [79], where the IDDES method also uses a formulation of [103].

3.2.3. Time stepping

To solve a time dependent differential equation numerically, a time stepping method is needed. For the solution of the incompressible flow equations, it is common to use a segregated flow solver. This solves for the individual unknowns iteratively and has less numerical effort than a coupled flow solver ([37, 55]). In StarCCM+ a SIMPLE algorithm is used for the coupling of pressure and velocity. The time integration is implicit of second order. This has the advantage, that it is unconditionally stable, even for large CFL numbers.

For hyperbolic equations that arise from wave equations in a form like

$$\mathbf{M}\ddot{p} + \mathbf{C}\dot{p} + \mathbf{K}p = \mathbf{F} \tag{3.64}$$

with a mass matrix $\mathbf{M}$, a damping matrix $\mathbf{C}$, a stiffness matrix $\mathbf{K}$, a forcing vector $\mathbf{F}$ as the right hand side and the unknown p. A common FE time stepping method is the Newmark method [60]. The dot quantities describe a time derivative. In the time stepping method, the time step size limits the frequency resolution. So if the right hand side contains high frequencies, with respect to the time step size, aliasing may occur. To avoid aliasing, the right hand side can be filtered or a time stepping method with frequency filtering properties, like the Hilbert-Hughes-Taylor method [49], can be used. This method is also called α-method. It is an adapted Newmark method, which is unconditionally stable and of second order accuracy for

$$\alpha \in [-1/3, 0]\,, \tag{3.65}$$

and the parameters of the original Newmark method

$$\gamma = (1 - 2\alpha)/2\,, \tag{3.66}$$
$$\beta = (1 - \alpha)^2/4\,. \tag{3.67}$$

The time discretized α-method writes then as

$$\mathbf{M}\ddot{p}_{n+1} + (1+\alpha)\mathbf{C}\dot{p}_{n+1} - \alpha\mathbf{C}\dot{p}_n + (1+\alpha)\mathbf{K}p_{n+1} - \alpha\mathbf{K}p_n = \mathbf{F}(t_{n+\alpha})\,, \tag{3.68}$$

with n denoting the previous time step, $n+1$ denoting the next time step and

$$t_{n+\alpha} = (1+\alpha)t_{n+1}\,. \tag{3.69}$$

Lower values of α increase the damping for under resolved frequencies. The method is supposed to filter frequencies with a ratio from time step size to period of $\frac{\Delta t}{T} \approx 0.1$.

The filtering behavior of the α-method is shown in Fig. 3.1. The transfer function H was computed in a pseudo 1-D duct with one meter length, a pressure excitation at one side and a non reflecting boundary condition at the receiver side. The mesh consisted of first order hexahedral elements and a sinus excitation with frequency steps of $100\,\mathrm{Hz}$ was used. The time step size was $\Delta t = 2 \cdot 10^{-5}s$ which results in a corner frequency of $f = 5\,\mathrm{kHz}$. For $\alpha = 0$ the standard implicit Newmark scheme is obtained and there is no damping. For frequencies above $5\,\mathrm{kHz}$, the transfer function gives unphysical results. For decreasing α values, the transfer function is slightly reduced from $2\,\mathrm{kHz}$ on and drops steeply above $5\,\mathrm{kHz}$ which matches with the approximated corner frequency of the filter. Thereby, the difference between $\alpha = -0.1$ and $\alpha = -0.2$ is still rather large, the difference between $\alpha = -0.2$ and $\alpha = -0.3$ doesn't seem to have a large influence.
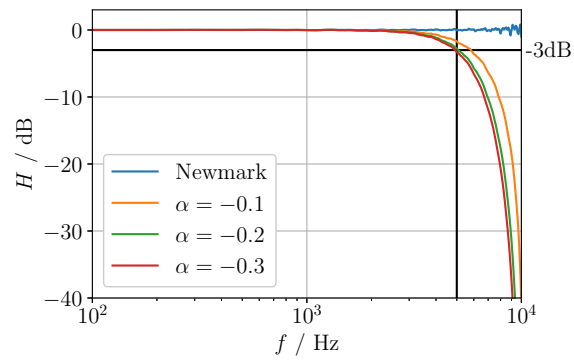
Figure 3.1.: Filtering of under resolved frequencies with the α-method for different α values.

Application

The application of numeric methods needs physical and geometrical modeling. Before numerically solving of the problem, the so called preprocessing has to be done. The main objective of is to set up a simulation in a way to obtain the desired information. The accuracy and amount of the simulation results are always a trade-off between computational time and accuracy. The results depend on the definition of the simulation domain. The simulation domain can't be infinite and has to be bounded. The further the boundaries are away from the region of interest, the less influence they have, but a larger domain will result in increased numerical effort. Therefore, it is necessary to define reasonable conditions on these boundaries, to reduce their unphysical influence on the solution and keep the size of the computational domain as small as possible. A further aspect of the preprocessing is the discretization of the simulation domain; a finer discretization leads to a better resolution of the solution, but also to increased numerical effort. The application of hybrid aeroacoustic methods, as described in section 2.3, consists of three main steps as shown in Fig. 4.1. Therefore it is useful to model every step individually to get the best balance of numerical effort and numerical error for every step.

In this work the PCWE formulation described in section 2.3.4 is used and therefore the description of the workflow is specialized on this analogy. The first step is the CFD simulation. In this work, the incompressible flow equations ((3.9) and (3.21)) are used. From the CFD simulation the incompressible flow field is obtained. This step is by far the most computational demanding one, since it needs a very fine mesh to resolve the instationary flow. Every computational error made in this step will effect the following steps. A detailed description of the CFD simulations and the flow results is done in section 4.2. The second step is the computation of the acoustic source terms from the flow results. This sources give a first insight in the acoustic characteristics, as strong source values indicate the location of the main acoustic mechanisms. The sources can be adapted before they are used further on, for example to only investigate sources from certain locations. It is also possible to reduce unphysical artifacts of the CFD simulation by blending source terms.

The computation can be done directly in the CFD solver or in an external step. The acoustic
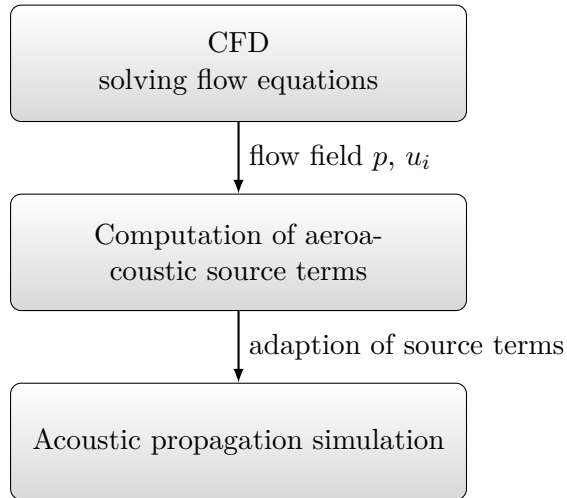
Figure 4.1.: Workflow for the hybrid aeroacoustic simulation.

simulation is the last step in this workflow. Here, the acoustic propagation into the far field is computed. The acoustic propagation computation does not have to be done on the very fine mesh of the CFD simulation, and it can be beneficial to use an adapted acoustic mesh. But an interpolation is needed, to transfer the hydrodynamic sources on the acoustic mesh.

The simpler a geometry is, the easier it is to model. Some applications can be modeled without any simplifications, but those are mostly generic applications that do not occur in reality. Although they are not practical applications, they can be used for fundamental investigations and validation. They are especially useful, if analytic solutions exist. For the purpose of validation of the workflow, a generic application is used in this work in section 4.3.1, 4.3.2 and 4.3.3.

For practical applications, the geometry is often very complex. Therefore, it can be necessary to simplify a geometry before it is used in a simulation. Care has to be taken, so that the simplifications do not alter the desired results. Small geometric details, away from the region of interest, are often neglected. The practical application in this work is described in section 4.1. It is used to show the applicability to engineering problems and the comparison to measurements and other prediction methods. It is also used to investigate the influence of simulation parameters and to gain insight in its physical behavior. The preprocessing for the CFD simulations is described in section 4.2 and for the acoustic simulation in section 4.3.4 and section 4.3.5.

4.1. Setup

The setup for the practical application is obtained from "A Benchmark Case for Aerodynamics and Aeroacoustics of a Low Pressure Axial Fan", which was presented in [123]. The paper provides a fan in a short duct with extensive amount of measurement data including aerodynamic performance (volume flow rate, pressure rise and efficiency), wall pressure fluctuations in the duct, fluid mechanical quantities on the fan suction and pressure side (velocity in three spatial

direction and turbulent kinetic energy) and acoustic spectra at different microphone positions upstream of the fan. The fan geometry and the measurement results were made publicly accessible on the platform *Benchmark Cases for Computational Acoustics* of the *European Acoustics Association* [31]. Further information about the benchmark platform can be found in [48].

The fan of the benchmark case was designed with the blade element theory for low solidity fans. In terms of size and operating conditions it is a typical fan to be used in commercial applications. Since the fan was designed as a benchmark case, the reproduction of the geometry was a goal. Therefore, the fan was designed with zero blade skew. Furthermore, the design

Table 4.1.: Fan design parameters

fan diameter	495 mm
hub diameter	248 mm
tip clearance	2.5 mm
blades	9
volumetric flow	$1.4 \, \mathrm{m^3/s}$
total-to-static pressure difference	150 Pa
rotational speed	1486 1/min
circumferential velocity hub	19.4 m/s
circumferential velocity tip	38.9 m/s
chord length hub	103 mm
chord length tip	58 mm
Reynolds number hub	$1.25 \cdot 10^5$
Reynolds number tip	$1.5 \cdot 10^5$

was not optimized for fluid dynamic or acoustic behavior. An optimization could for example be achieved by blade skew, the reduction of the tip flow by vortex generators or serrations. The blades consist of NACA 4510 profiles [70]. The further design parameters are shown in Tab. 4.1. The circumferential velocity at the blade tip corresponds to a Mach number of $\mathrm{Ma} \approx 0.113$, thus the flow can be considered incompressible. The Reynolds number is almost constant over the height of the blade. Its value indicates a turbulent flow [122].

The measurements were made in a standardized inlet test chamber (see Fig. 4.2) according to ISO 5801 [54]. The test chamber was equipped with anechoic walls for the acoustic measurements. The volumetric flow was adjusted by butterfly dampers and an auxiliary fan in the inlet section. The flow was rectified in the first half of the inlet chamber by a flow straightener. The duct was installed in the wall of the chamber, with the suction side facing inwards and the pressure side facing outwards. The fan was driven by an external electric engine outside of the measurement chamber. For more information about measurements in this setup see [69]. The measured pressure rise of the fan at the design volumetric flow is $\Delta p = 126.5 \, \mathrm{Pa}$. The design pressure difference is not completely reached due to unconsidered losses like tip flow. At the design point the efficiency according to (2.6) was $\eta = 53 \, \%$. This measurement data were also used in [58].

The available measurement results contain microphone signals with a sampling frequency of
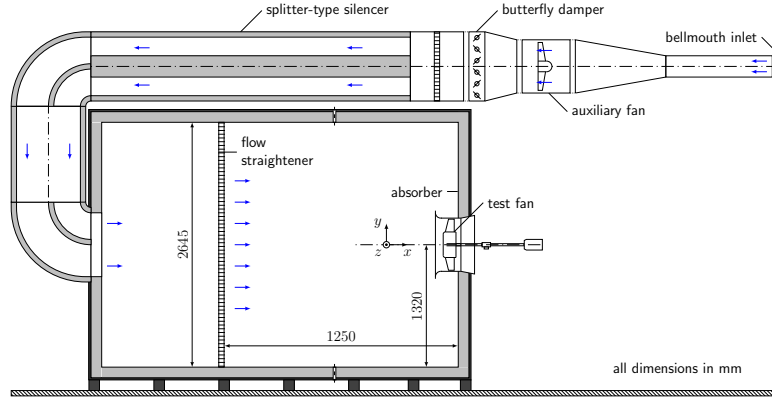
Figure 4.2.: Measurement chamber according to [123]

48 kHz and length of $T = 30$ s. In the measurement $N = 7$ microphones were installed in a half circle with a radius of 1 m in front of the nozzle of the duct. The sound power level was computed according to [2]:

$$L_{\text{W}} = \bar{L}_{\text{P}} + 10 \log \left(\frac{S_1}{S_0} \right) \, \text{dB} \,, \tag{4.1}$$

with the time averaged sound pressure level $\bar{L}_{\text{P}}$, the hull of the measurement area $S_1 = 6.28 \, \text{m}^2$ and $S_0 = 1 \, \text{m}^2$. The time averaged sound power level for all microphones is computed as

$$\bar{L}_{\text{P}} = 10 \log \left(\frac{1}{N} \sum_{n=1}^{N} \frac{1}{T} \int p_n^2 \, \text{d}t / p_0^2 \right) \, \text{dB} \,, \tag{4.2}$$

with the reference pressure $p_0 = 20 \, \mu\text{Pa}$. For a frequency range of 100 Hz to 10 kHz, the measured sound power level was $L_{\text{W}} = 87.3$ dB. The spectrum of the sound power level is shown in Fig. 4.3. The first Blade Passing Frequency (BPF) can be seen as a sharp peak
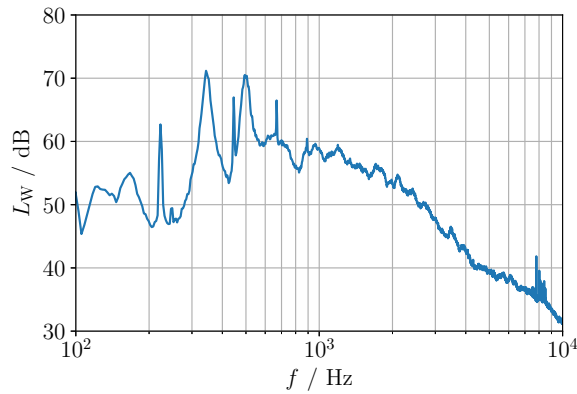
Figure 4.3.: Measured sound power level of the investigated fan.

at 223 Hz, the second BPF at 446 Hz and the third at 675 Hz. Broader peaks are around 340 Hz and 500 Hz that exceed the ones from the BPF. They are expected to result from the interaction of the tip flow with the blades. They are going to be referred to as the first and second visible subharmonic peak. Above 800 Hz, the spectrum consists of broadband noise.

4.2. Computational fluid dynamics

The CFD domain was derived from the CAD model of the measurement setup. The fan installed in the duct is shown in Fig. 4.4a, during the measurements of [123]. The geometry of

(a) Fan istalled in the duct measurement [123]   (b) Fan geometry of the CFD simulation
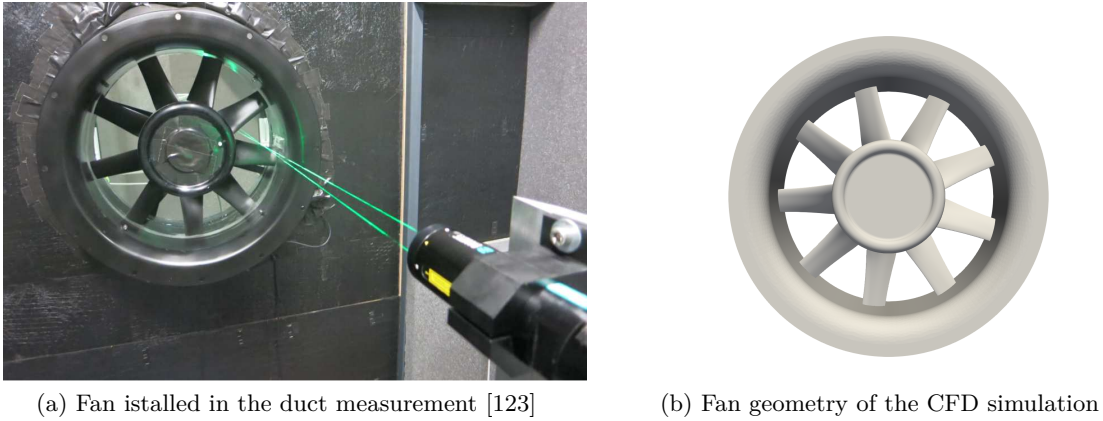
Figure 4.4.: Fan geometry of the measurement and simulation.

the fan used in the CFD simulations is shown in Fig. 4.4b. To adapt the CAD model to the need of the CFD simulation, some geometric simplifications were done. The holes in the inlet nozzle as well as the gaps and the front face of the hub are simplified. The electrical engine outside the measurement chamber is reduced to a cylinder with similar extent, to account for the blocking in the wake. For the same reason, the struts behind the rotor are preserved in shape. The blade geometry is not altered.

The whole simulation domain in shown in Fig. 4.5, with the flow direction from left to right. The inlet domain has an extent of 2.32 m × 2.4 m × 2.4 m which is about the size of the inlet chamber in the measurement after the flow straightener. The inlet domain is stationary and contains the nozzle of the test section. The inlet domain is connected with nonconforming interfaces to the rotating domain. The rotating domain contains the straight section of the duct, including the fan. After the rotating region, a second stationary region is connected with a further nonconforming interface. Directly after the interface, the diffusor leads the flow in the outlet region. The outlet domain has an extent of 2.0 m × 2.4 m × 2.4 m which is the same cross section as the inlet domain and a length of $4D$ with D the duct diameter.

The volume flow rate of the design point results in a mean inlet velocity of 0.24 m/s. Therefore, the influence of an inlet velocity profile was considered negligible and a volume flow rate boundary condition was used. Due to the prescribed flow rate, errors in the numerical simulations result in an error of the pressure rise of the fan. On the outlet surface perpendicular to
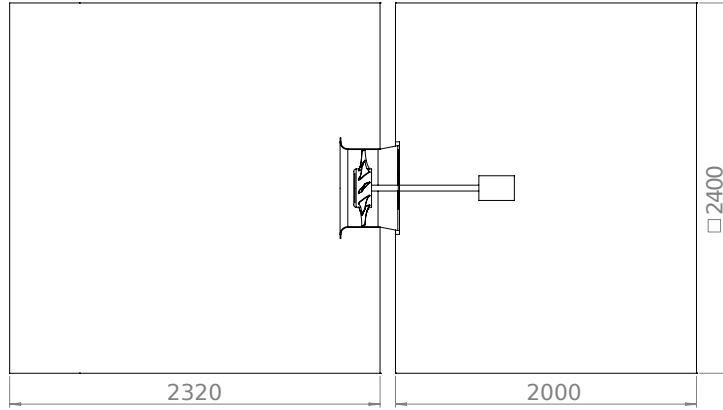
Figure 4.5.: CFD simulation domain, with simplified engine.

the main flow direction a pressure outlet with zero pressure was applied. All other boundaries were modeled as no slip walls.

The used CFD code was Star-CCM+ v.12.06 [104]. It is a highly parallelized finite volume code. It was not only used to solve the CFD simulation, but also for mesh generation. It also contains an aeroacoustic module, which is able to compute the FWH integrals and the Curle integral and Proudman acoustic source terms shown in section 5.

In the CFD simulations a cut cell mesh approach was used, also referred to as trimmed mesh. It uses mainly hexahedral elements, which are subdivided for mesh refinement, which leads to a mesh with hanging nodes. The geometry is resolved by a non orthogonal cutting of the elements, and leads to polyhedral elements. The hexahedral elements have a lower dissipation error than tetrahedral or polyhedral elements, which is important for high accuracy simulations. On the boundary of the fan and duct, prism layers are applied to resolve the boundary layer. The CFD mesh is shown in Fig. 4.6. The rotating domain is discretized with a constant mesh size, which is referred to as the base size h. The nozzle and the diffusor are also discretized with the base size. Therefore, the nonmatching interfaces have the same cell size on both sides. Downstream of the nozzle, the mesh size is $4h$ for $1.8D$ to resolve the turbulent wake of the fan. Upstream of the nozzle, the same mesh size is applied for $0.5D$. Outside of this refinement regions, the mesh gradually increases to a maximum cell size of $50h$. For the duct four prism layers with a total height of $0.5h$ and a stretching ratio of 1.5 were used (for a base size of $h = 2\,\text{mm}$ this leads to an initial height of $6 \cdot 10^{-5}\,\text{m}$). At the fan blades five prism layers with a total height $1/3h$ and a stretching ratio of 1.6 were used (for a base size of $h = 2\,\text{mm}$ this leads to an initial height of $2 \cdot 10^{-5}\,\text{m}$). The target surface size on the fan blades was $0.5h$.

In Fig. 4.7 a slice of the instationary velocity field is shown. Upstream of the fan, the velocity field is relatively smooth, which is the reason why less refinement is necessary. The largest velocity amplitudes occur directly at the blade tips. An increased velocity towards the lower duct wall can be seen which results from the tip flow. At the hub, large turbulent structures can be seen, which arise from the horseshoe vortices at the blade roots. Downstream of the fan, the flow is characterized by large scale turbulences which are convected through the duct. The turbulent structures are dissipated as the mesh size increases towards the outlet.
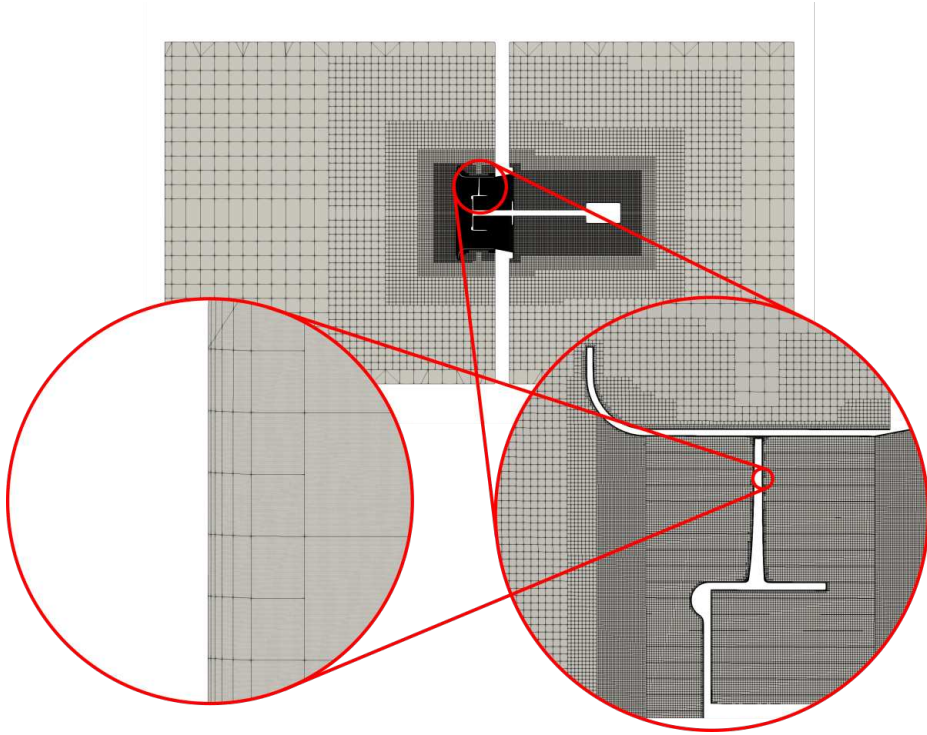
Figure 4.6.: CFD mesh with a close up of the rotating domain and the prism layers on the fan blades.

The CFD simulations were initialized with a RANS simulation. The RANS simulation was run for $10\,\mathrm{k}$ iterations, after which the pressure raise and momentum (and therefore efficiency) of the fan was constant. The resulting pressure and velocity fields were used as the initial conditions for the transient simulations. The transient simulations used a time step size of $\Delta t = 10\,\mathrm{\mu s}$. This time step size leads to a maximal rotation of $\Delta \alpha = 0.089°$ per step. At the outer radius of the rotating domain this corresponds to a movement of $0.39\,\mathrm{mm}$, which is between $15\% - 40\%$ of the used mesh sizes at this location. A second order time stepping was used and each time step was solved with 10 inner iterations. The time step size directly influences the Courant–Friedrichs–Lewy (*CFL*) number

$$CFL = \frac{u\Delta t}{\Delta h}\,,\tag{4.3}$$

which can be interpreted as how many cells a fluid particle is crossing in one time step. For explicit solving methods, the *CFL* number is a stability criterion and is required to be $CFL < 1$. In other words, a fluid particle should not cross more than one cell per time step. For implicit solving methods, as used in this work, the *CFL* number is only a criteria of accuracy. For most regions of the CFD simulations $CFL < 1$ was fulfilled and the maximum value was $CFL_{\max} = 150$.

The simulation was run for $0.1\,\mathrm{s}$ or 2.48 revolutions of the fan (respectively $10\,\mathrm{k}$ time steps)
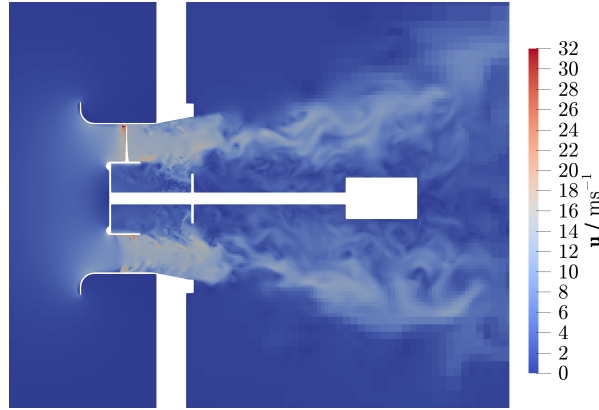
Figure 4.7.: Instationary velocity field of the duct and wake area.

to obtain a stationary operating point in the solution. After that, every second time step was exported. A total of 0.4 s or 9.9 revolutions (respectively 20 k time steps) were exported. The computations were performed on the Vienna Scientific Cluster (VSC-3). It was installed 2014 and has a total of 2020 compute nodes with 2 x Intel Xeon IvyBridge-EP E5-2650v2 each with 8 2.6 GHz cores. Each node was equipped with 64 GB RAM. The nodes were connected with an Intel QDR-80 dual-link high-speed InfiniBand. The statistics for the CFD simulation are summarized in Tab. 4.2.

The results of the CFD simulation were evaluated at the same locations as the measurements in [123]. The geometry of the fan and duct and the evaluation areas are displayed in Fig. 4.8. The two measurement plains for the evaluation of the flow velocity are displayed in green. They are directly for and after the root of the fan blades. In the measurement, a total of 15 transducers were used to measure the wall pressure fluctuation. In the figure four selected transducer positions are displayed in black. The transducers were installed 15 mm after the end of the nozzle, with a spacing of 10 mm Transducer 2 (25 mm behind the nozzle) of the measurement is upstream of the fan close to the nozzle, 7 (75 mm behind the nozzle) is directly in front of the blade tip, 9 (95 mm behind the nozzle) is in the middle of the duct where the blade tips pass and 13 (135 mm behind the nozzle) is downstream of the fan close to the diffusor. The suction side of measurement plane is located 20 mm behind the hub and suction side measurement plane is located 110 mm behind the hub.

4.2.1. Turbulence

A DES simulation was used to model the turbulent flow in this work. The DES simulation blends between a URANS simulation near the wall and an LES simulation outside the boundary layers (as described in section 3.2.2). The blending function f_{DES} is shown in Fig. 4.9, where $f_{DES} = 0$ stands for a complete LES simulation and $f_{DES} = 1$ for a complete URANS simulation. It can be seen that the URANS model is used just directly at the walls of the duct and the fan and the rest of the domain is treated as LES. Among other things, the blending is depending on the mesh size as can be seen at the top and bottom of the figure at the wall and at the right part of the shaft. For too coarse meshes, the blending function can treat too

Table 4.2.: CFD simulation statistics.

Mesh	
Base size	2 mm
Cells in stationary domain	9411028
Cells in rotating domain	14033434
RANS simulation	
CPUs	64
Iterations	10000
Wall clock time	9 h
Core hours	576 h
DES simulation	
CPUs	256
Exported time steps	20000
Time step size	10 µs
Wall clock time for export	225.5 h
Core hours	57732 h
Exported data	32.1 TB

much areas as URANS simulations. Therefore, the blending has to be checked depending on the simulation.

For the simulation of wall bounded flows, it is important to simulate boundary layers adequately. The turbulent boundary layer is described by the non dimensional wall distance y^+ and the non dimensional wall parallel velocity u^+. Figure 4.10 shows the relation of u^+ and y^+. The turbulent boundary layer can be divided in three different regions. First the viscous sub layer, directly at the wall where the viscous forces are dominant. In this region, the boundary layer is laminar and the relation is

$$u^+ = y^+ \,. \tag{4.4}$$

In Fig. 4.10 this region is up to $y^+ \approx 5$. In the outer region, the turbulent effects increase and the logarithmic relation

$$u^+ = \frac{1}{\kappa} \ln\left(E' y^+\right) \tag{4.5}$$

connects the velocity with the wall distance, with the von Karman constant $\kappa = 0.42$ and

$$E' = \frac{E}{f_{\mathrm{r}}} \tag{4.6}$$

with the constant $E = 9.0$ and f_{r} the roughness function (with $f_{\mathrm{r}} = 1$ for smooth walls). This region extends up to $y^+ \approx 30$. Between both regions is the buffer layer, which is a transition
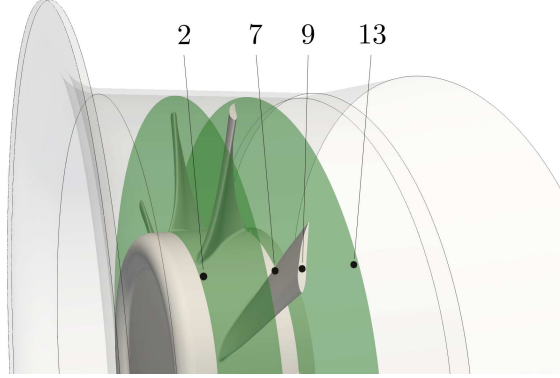
Figure 4.8.: Measurement locations for the evaluation of the flow results with the measurement plains in green and the positions of four selected transducers in black.
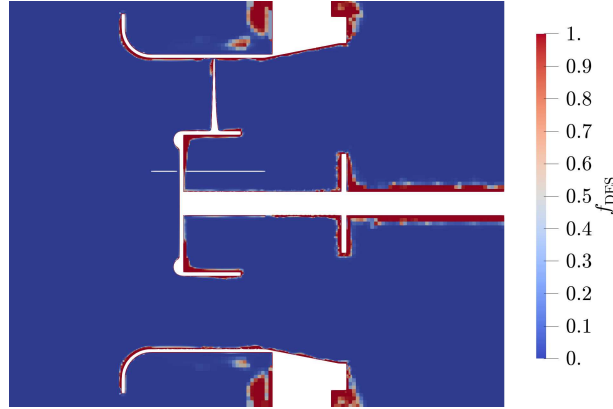
Figure 4.9.: DES blending between LES and URANS simulation.

between both models. Reichardt's law [93] is a function to describe all three regions as

$$u^+ = \frac{1}{\kappa} \ln\left(1 + \kappa y^+\right) + C \left(1 - \exp\left(-\frac{y^+}{D}\right) - \frac{y^+}{D} \exp\left(-by^+\right)\right), \qquad (4.7)$$

with

$$b = \frac{1}{2}\left(\frac{D\kappa}{C} + \frac{1}{D}\right), \qquad (4.8)$$

$$C = \frac{1}{\kappa} \ln\left(\frac{E'}{\kappa}\right), \qquad (4.9)$$

and D the intersection of viscous and turbulent region. For smooth walls this value is $D = 11.2$.

In CFD, there exist two main approaches to simulate boundary layers. The first is to resolve
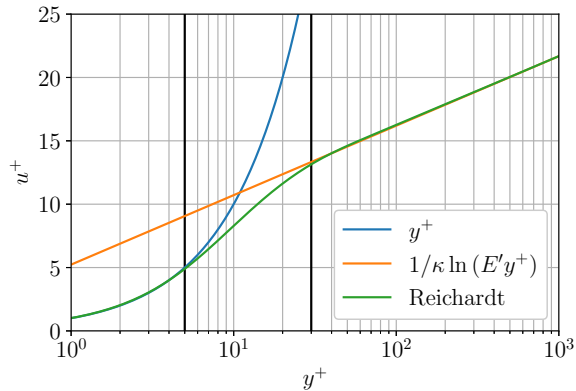
Figure 4.10.: Non dimensional velocity u^+ in the boundary layer according to [93]

the boundary layer good enough to resolve the velocity profile in all three layers. Therefore, the first prism layer has to be in the viscous sub layer. This is satisfied with the $y^+ = 1$ criterion. The second approach is to place the first prism layer in the logarithmic boundary layer, which is satisfied for $y^+ > 30$. Then a so called wall function is used, to represent the missing information of the viscous sub layer and buffer layer. In fan simulations, the rotation leads to very different flow velocities along a blade. This yields strong demands on a mesh to resolve the boundary layer in all regions adequately. In StarCCM+ the all y^+-treatment offers an automatic switching between high y^+- and low y^+-treatment. This option was used to cover regions where the $y^+ = 1$ criterion is not fulfilled. The y^+ values of the CFD simulation are shown in Fig. 4.11. The highest y^+ values occur at the suction side of the blades at the outer
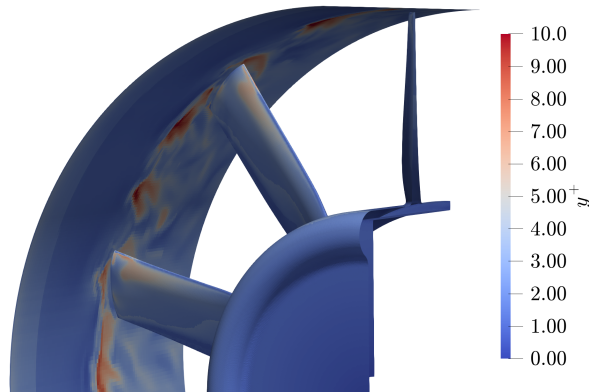
Figure 4.11.: y^+ criterion on the fan and duct.

radius and where the flow interacts with the duct, with a global maximum value of $y^+ = 14$.

A further aspect of the simulation of the boundary layers is the used turbulence model. For the URANS simulation in StarCCM+ there are two different models available. First the SA model and second the k-ω SST model. Both methods were tried. The comparison of the time

43

averaged velocity in axial direction on the suction side is shown in Fig. 4.12. On the suction
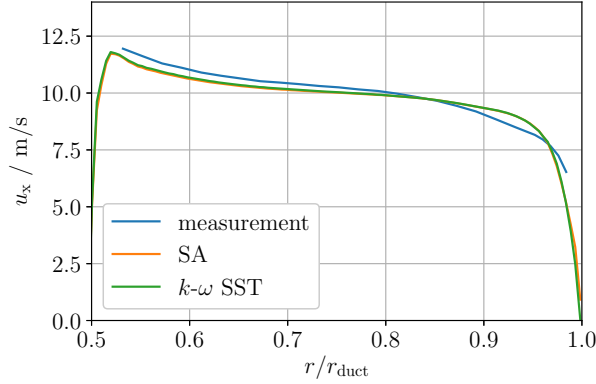
Figure 4.12.: Time averaged velocity in axial direction on the suction side.
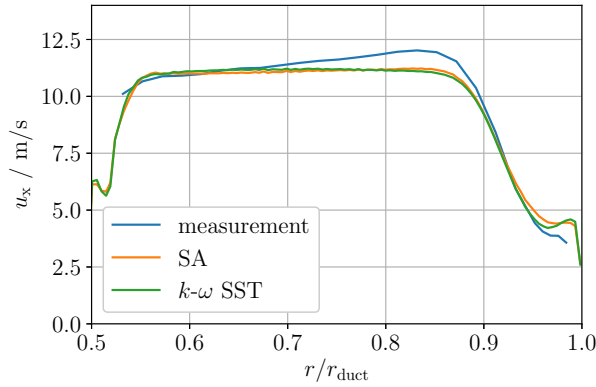
Figure 4.13.: Time averaged velocity in axial direction on the pressure side.

side, the velocity profiles are almost identical. On the pressure side shown in Fig. 4.13, a small deviations occurs around $r/r_{\text{duct}} = 0.95$ but over all, the result is the same. Especially on the largest deviations to the measurement in the region $6.5 < r/r_{\text{duct}} < 0.9$ the turbulence model does not have an effect. But due to the higher numerical effort the k-ω SST model is 10 % slower, therefore, the Spalart-Allmaras (SA) model is used.

The flow off the walls is modeled by LES (for $f_{\text{DES}} = 0$). The LES resolves the large turbulences and models the subgrid scale turbulence. How much of the eddies is really resolves by the LES depends on the mesh resolution. For too coarse meshes, too less eddies are resolved and too much turbulence is modeled by the sub grid model. The relation of resolved turbulent kinetic energy k_{res} to the modeled turbulent kinetic energy of the sub grid model k_{sgs} is a

common criterion to estimate the quality of the resolution used in the form

$$LES_{\mathrm{res}} = \frac{k_{\mathrm{res}}}{k_{\mathrm{res}} + k_{\mathrm{sgs}}} \, . \tag{4.10}$$

This gives a criterion between 0 and 1. For higher values (commonly used value is 0.8 or higher) most turbulent kinetic energy is resolved. Since StarCCM+ does not provide k_{sgs} directly in DES simulations, a criterion according to [22] was used. This criterion uses a relation of viscosity μ and turbulent viscosity μ_{turb} in the form

$$LES_\mu = \frac{1}{1 + \alpha \left(\frac{\mu + \mu_{\mathrm{turb}}}{\mu} \right)^n} \, , \tag{4.11}$$

with $\alpha = 0.05$ and $n = 0.53$ providing similar values as (4.10). For the DES simulation this criterion is just valid in regions where the LES model is used. Therefore, the values in the boundary layer should be neglected. The result of (4.11) is shown in Fig. 4.14. Upstream of
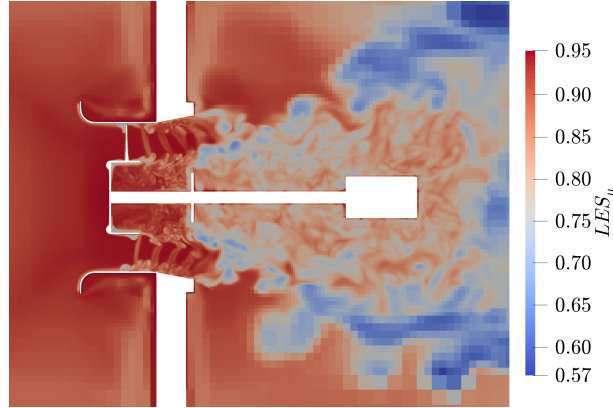
Figure 4.14.: Resolution of the DES simulation with values above 0.8 show a recommended resolution.

the fan, over 85 % of the turbulent kinetic energy is resolved. In the vortex core resulting of the tip flow, it is about 70 %. In the diffusor, it is between 80 % and 95 %. In most regions of the wake, it is between 70 % and 80 % and in the outer shear layer of the wake, especially towards the coarse cells at the outlet, the values are between 57 % and 70 %.

4.2.2. Convergence

For the numerical simulation, the domain has to be approximated by a discretized model. This discretization introduces an error to the simulation. The finer the discretization is, the smaller the error becomes and the discretized solution converges to the continuous solution. The convergence is shown in a convergence study. For a fine enough discretization, the result does not change due to a change in the mesh, which is called mesh independence of the solution.

In practice a fully converged mesh can just be obtained for very simple problems. For real

Table 4.3.: Used mesh sizes and cell numbers for the investigation of convergence.

	coarse	middle	fine	extra fine
base size h in mm	4	3	2	1.5
cell number n in M	6.8	9.8	23.4	41.5

application problems, the finer and finer meshes lead to a rapidly increasing demand of computational power, where the error is decreasing but not zero. So a completely converged grid will never be reached. A common practice is to perform at least three simulations with different mesh sizes and use a Richardson extrapolation (without higher order terms) to estimate the real solution f as

$$f = f_{\mathrm{h}} + ch^p \tag{4.12}$$

from the discretized solution quantity f_{h}, a constant c and the mesh size h with an exponent p (which should theoretically be $p \approx 2$). From the three simulations the three unknowns can be computed, but this works only if the solutions are in the region of convergence. It should be noted, that (4.12) lacks if the cell size h is not refined uniformly in space as pointed out in [97]. In general this method is used for integrated solution quantities like lift or drag coefficient from RANS simulations (for example in [96]).

In this work, four different mesh sizes were used to investigate the mesh convergence, so (4.12) can not be solved directly and it is not of interest to calculate the exact rate of convergence. Therefore, a nonlinear curve fitting algorithm was used to extrapolate the simulation results. The cell numbers and the base mesh sizes are displayed in Tab. 4.3. Except the prism layers, the other regions are specified relatively to the base mesh sizes. So the refinement is mostly uniform in space.

The results of the convergence investigation are shown for the initial RANS simulations as well as for the DES simulations. The results of the DES simulations were time averaged. The result quantities are displayed over the cell number $n^{-\frac{2}{3}}$, which is commonly used as a non dimensional cell size to the power of two (see for example [114]). Figure 4.15 shows the pressure rise of the different meshes and simulation types. Both simulation types show a monotone convergence, where the extrapolated RANS simulation underestimates the pressure rise by 7.6 % and the DES simulation overestimates the pressure rise by 11.3 %. Figure 4.16 shows the total-to-static efficiency η according to (2.6). The convergence is again monotone, and the extrapolated result of the RANS simulation underestimates the efficiency by 8.3 % and the DES simulation overestimates the efficiency by 3.4 %. Figure 4.17 shows the shaft power P. The DES solution has an extrapolated error of 7.1 %. The RANS solution has an error of 1.0 % but does not converge monotonically. An explanation can be that for the shaft power, the coarse mesh has a too large mesh size, to be in the region of convergence. The shaft power is computed from the torque of the fan, which itself results from the drag of the profiles, which is more difficult to calculate then for example the lift of the profiles. All investigated quantities are time averaged and it is questionable what information can really be obtained from them for the actual objective of the transient simulation, which are the sources for the acoustic propagation simulation. For computational aeroacoustics time dependent results are
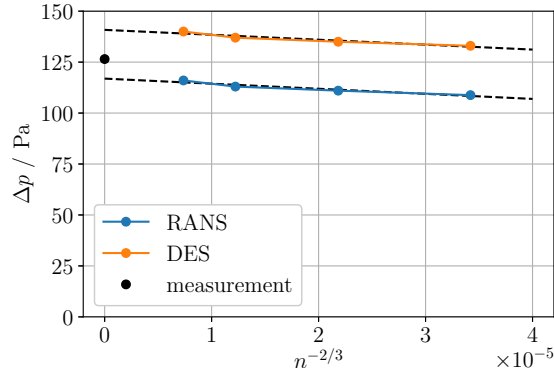
Figure 4.15.: Convergence of the pressure rise Δp for RANS simulations (blue) and DES simulations (orange).
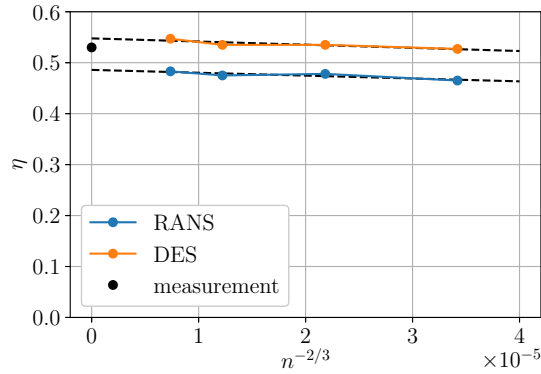

Figure 4.16.: Convergence of the total-to-static efficiency η for RANS simulations (blue) and DES simulations (orange).

needed and for time dependent quantities a convergence can not be evaluated as simple as for integral quantities. In fact, the important quantities for the aeroacoustic computation are the computed source terms of the acoustic method. These are transient field quantities, which should be evaluated in a spectral manner to represent the spectral result. This would require a Fourier transformation of the complete exported quantities, or the aeroacoustic result could be used as a criteria for the convergence of the simulation. But this result is just obtained at the very end of the forward coupled simulation. So not just the CFD simulation has to be stationary in time for the evaluation, but also the complete CFD results, source term computation and acoustic propagation simulation have to be done. This is an immense effort, since this has to be done for at least three different meshes and - at the current point of simulation time - is not possible in a real world application.

For the DES simulations it is possible to evaluate spectral quantities at certain points of interest, if there is enough simulation time. In general the simulation time for the convergence
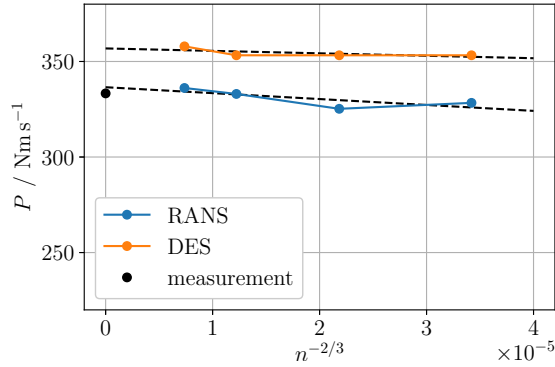
Figure 4.17.: Convergence of the shaft power P for RANS simulations (blue) and DES simulations (orange).

investigation is held as short as possible and therefore the frequency resolution is poor. The results can give some insight in the fluctuating quantities which result in the acoustic sources, but it gives no direct information about the convergence. In this work the pressure transducer 7 from the measurements was used, since there occur high pressure fluctuations and large acoustic source terms can be expected at this position. The comparison of the PSD from the different simulations is shown in Fig. 4.18. The frequency resolution is coarse due to the
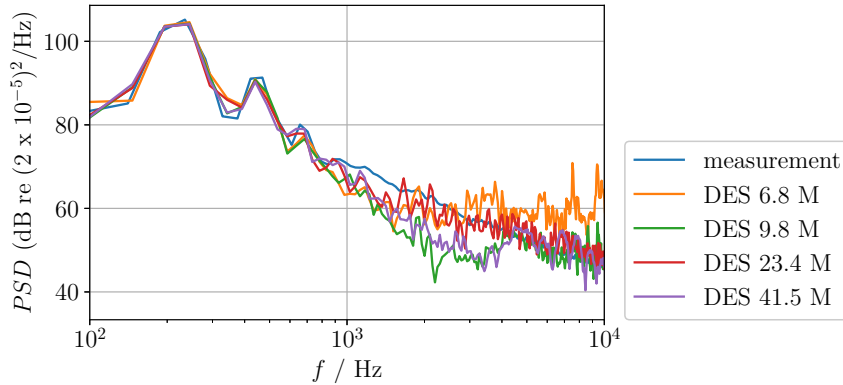
Figure 4.18.: Power spectral density dependent on cell number.

short simulation time. Until 1 kHz all simulations are similar and represent the BPF and its first harmonic. The coarse simulation overestimates the PSD in the high frequency range. The other simulations reproduce the decline between 4 and 10 kHz. Between 1 and 4 kHz the simulations underestimate the PSD but no trend can be seen according to the mesh size.

Furthermore, in this work the convergence was observed with the time averaged axial velocity profile between the hub and the duct. Figure 4.19 shows the simulation results on the suction side. The coarse simulation shows a faster reduction towards the duct wall than the other
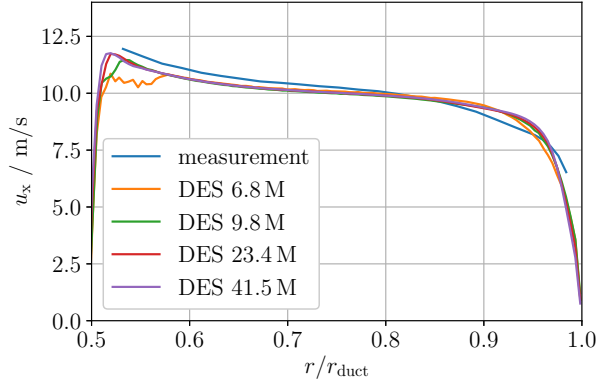
Figure 4.19.: Time averaged velocity in axial direction on the suction side.

simulations. At the hub, the coarse and the middle simulation show a rough velocity profile, where between the fine and the very fine simulation almost no difference occur. Figure 4.20 shows the results on the pressure side. The coarse simulation deviates from the other simulation
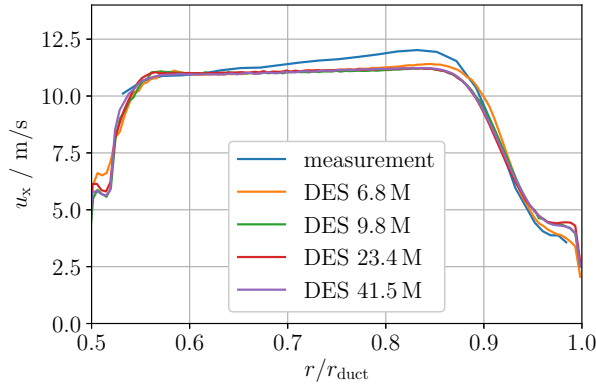

Figure 4.20.: Time averaged velocity in axial direction on the pressure side.

results directly at the duct and for $r/r_{\text{duct}} > 0.8$. The rest of the simulations deviate only slightly directly at the hub and the duct wall. For both sides the measurement result is not completely met, but the influence of the mesh seems very small between the fine and very fine mesh. Therefore, no improvement is expected from further mesh refinement. From here on, the CFD simulations are done with the fine mesh.

4.2.3. Flow properties

In Fig. 4.21 the wall pressure fluctuations are shown from the measurement and the CFD simulation for the selected transducers. The CFD simulation time for the evaluation of the spectral results was 0.1 s. Upstream of the fan at transducer position 2, the spectrum is

(a) Measurement position 2

(b) Measurement position 7

(c) Measurement position 9

(d) Measurement position 13
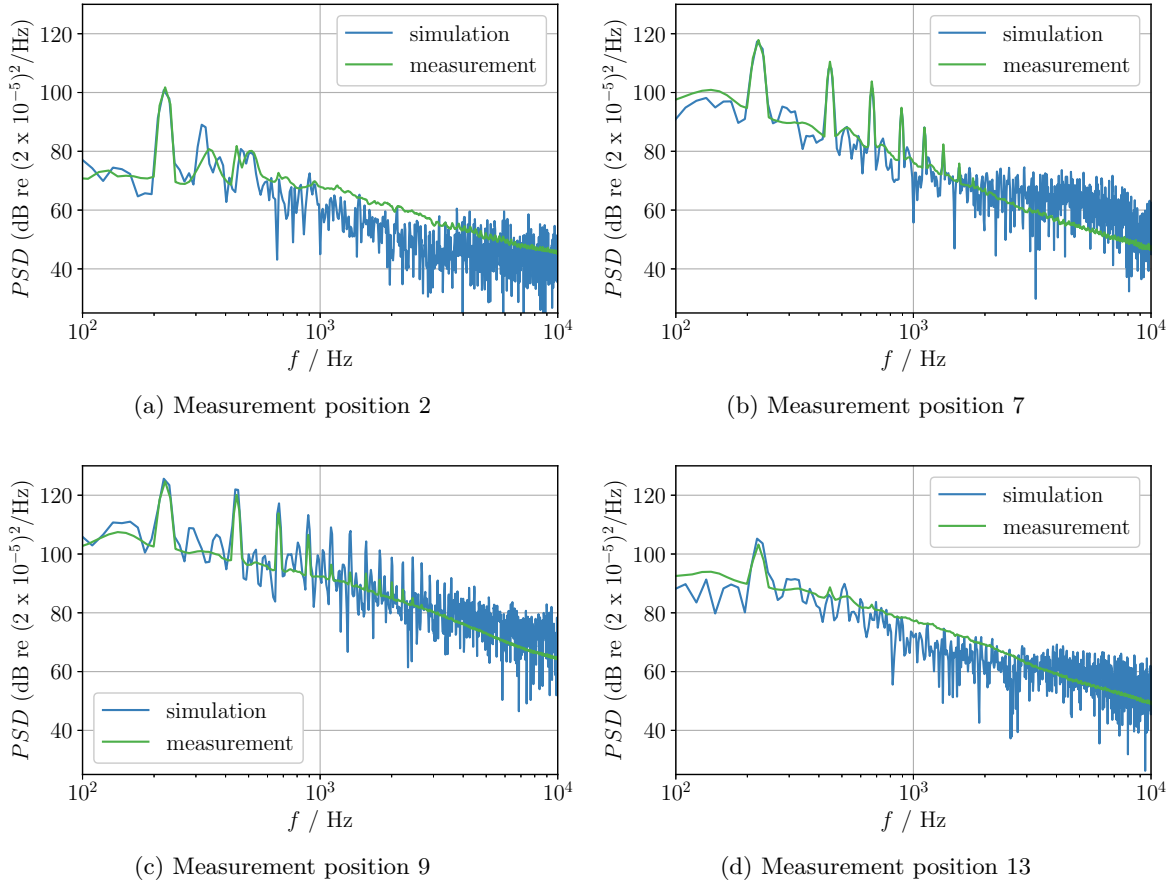
Figure 4.21.: Comparison of wall pressure fluctuations from measurement and simulation.

dominated by a peak at the BPF. The BPF peak is met by the simulation, but the broadband noise above 1 kHz is underestimated. For the positions in the middle of the duct, the overall level is higher and the higher harmonics of the BPF are visible. For transducer 7 the higher harmonics are met, but for transducer 9 the harmonics of order 4 and higher are overestimated. For both positions the broadband noise is slightly overestimated. The highest wall pressure levels occur at transducer 9. Downstream of the fan the first BPF is similar in amplitude to the upstream spectrum, but the broadband noise is much higher over the whole spectrum.

In Fig. 4.22 the velocity results in axial direction on the measurement plains are displayed, where the figures on the left side are measurement results from Laser Doppler Anemometry and on the right side CFD simulation results. The first row are results on the suction side upstream of the fan and the second row are results on the pressure side downstream of the fan. On the suction side the velocity is underestimated by the CFD simulation close to the wall, where the over all amplitude and shape of the velocity profile are reproduced. On the pressure side, the velocity is higher close to the wall but lower towards the middle of the duct. On the pressure side, the wake profile from the fan blades is reproduced in shape.
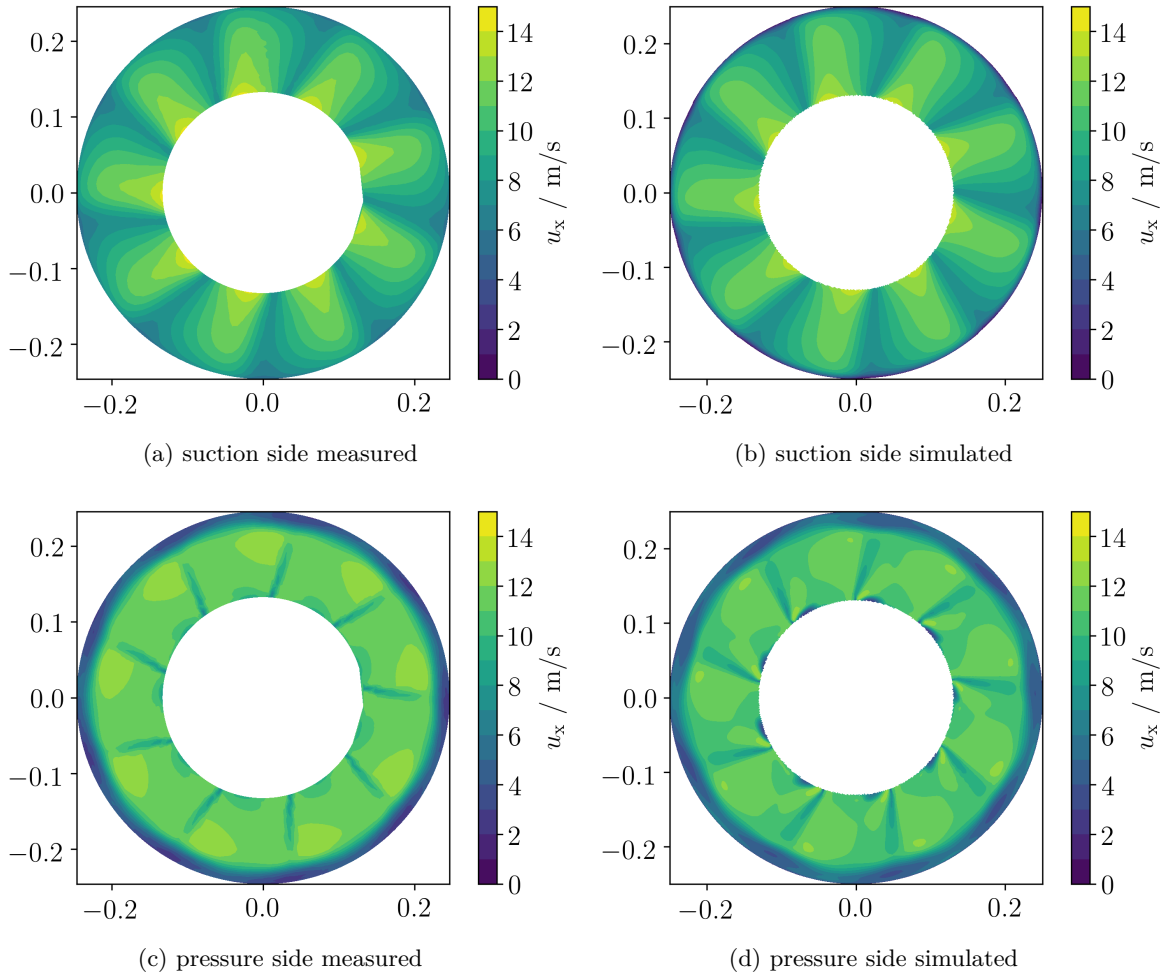
(a) suction side measured   (b) suction side simulated

(c) pressure side measured   (d) pressure side simulated

Figure 4.22.: Mean flow velocity in axial direction.

4.3. Computational aeroacoustics

The acoustic propagation simulation was solved in time domain. For a moving system it is in general not possible to derive a model in the frequency domain. For special cases, for example where the moving system can be transformed to a stationary one, with a moving frame of reference, the modeling in frequency domain is possible. But therefore the simulation domain has to be completely rotational symmetric, which is not given for the rectangular measurement chamber, as well as the struts supporting the fan. Therefore, the used time domain formulation is the PCWE. This formulation allows the investigation of aeroacoustic sources, to deduce the sound producing mechanisms. With its splitting of acoustic and incompressible pressure fluctuations it is also possible to investigate the acoustic results in the source domain. Furthermore, it takes into account reflections and refractions. This is necessary since the geometry of the duct and the nozzle have a strong impact on the radiation. For monopole sources in the

duct, integral solutions like from section 2.3.1 would result in a non directional radiation. In contrast to that, the section 2.3.4 method is capable to resolve the refraction and reflection from the duct as shown is section 5.1.

4.3.1. Validation with the rotating vortex pair

As a validation example the rotating vortex pair is used. The velocity and pressure field of the vortex pair is computed with the two dimensional potential flow (see appendix section A). The schematic of the vortex pair is displayed in Fig. 4.23. The two vortices rotate in a two
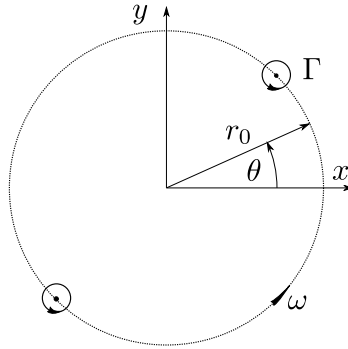
Figure 4.23.: Schematic of the rotating vortex pair.

dimensional plane around a common center with the radius r_0. Both vortices have a circulation intensity Γ. The angular velocity is $\omega = \Gamma/(4\pi r_0^2)$ (respectively the circumferential velocity is $u_\theta = \Gamma/(4\pi r_0)$), which leads to a rotation period of $T = 8\pi^2 r_0^2/\Gamma$ and a rotational Mach number $\mathrm{Ma}_\theta = u_\theta/c_0 = \Gamma/(4\pi r_0 c_0) = 2\pi r_0/T c_0$. The flow field of the rotating vortex pair results in an acoustic rotating quadruple radiation. The radiation behavior is a standard example for code validation (for example see [72] or [30]).

The rotating vortex pair is generated by the superposition of two potential vortices. The polar coordinates with the radius r and the angle θ are described with Euler's formula as the complex coordinate z

$$z = re^{i\theta}\,. \tag{4.13}$$

The position of one vortex is described by

$$b = r_0 e^{i\omega t}\,. \tag{4.14}$$

The complex velocity potential F for the two vortices at the positions $\pm b$ can be written as

$$F(z) = \frac{\Gamma}{2\pi i}\ln(z-b) + \frac{\Gamma}{2\pi i}\ln(z+b) = \frac{\Gamma}{2\pi i}\ln(z^2 - b^2)\,. \tag{4.15}$$

4. Application

The resulting velocity field is obtained by the derivative with respect to the complex coordinate

$$\frac{dF}{dz} = u - iv = \frac{\Gamma}{\pi i}\frac{z}{z^2 - b^2} \,, \tag{4.16}$$

and the resulting incompressible pressure field can be computed according to (A.6) as

$$p^{ic} = p_0 - \rho_0\frac{\partial\Re F}{\partial t} - \frac{1}{2}\rho_0\left(u^2 + v^2\right) \,, \tag{4.17}$$

with a constant mean pressure p_0 and $\Re$ describing the real part. The mean pressure gives a constant offset and can be neglected for the investigation of the fluctuating pressure field later on. The second term on the right hand side is

$$\frac{\partial\Re F}{\partial t} = \frac{r_0\omega\Gamma(r_0^2 - r^2\cos(2t\omega - 2\theta))}{\pi(r^4 + r_0^4 - 2r^2r_0^2\cos(2t\omega - 2\theta))} \,, \tag{4.18}$$

and the velocity part of the third term on the right hand side is

$$u^2 + v^2 = \frac{r^2\Gamma^2}{\pi^2(r^4 + r_0^4 - 2r^2r_0^2\cos(2t\omega - 2\theta))} \,. \tag{4.19}$$

An analytic solution for the rotating vortex pair was derived in [83]. With a matched asymptotic expansion, the far field pressure fluctuation can be computed as:

$$p' = \frac{\rho_0\Gamma^4}{64\pi^3 r_0^4 c_0^2}\left[J_2(2kr)\cos(2(\omega t - \theta)) - Y_2(2kr)\sin(2(\omega t - \theta))\right] \,, \tag{4.20}$$

with second order Bessel functions of first and second kind and $k = \omega/c_0$.

For the numerical validation a two dimensional computational domain was used (see Fig. 4.24). It consists of a round source region (in red) with a radius of $4.95\,\text{m}$ where the incompress-
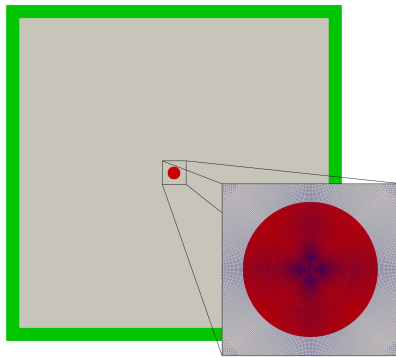

Figure 4.24.: Acoustic mesh regions, with the PML in green, propagation region in gray and the source region in red.

ible pressure field is applied, propagation region of 240 m by 240 m (in gray) and a Perfectly Matched Layer (PML) region (in green) with a thickness of 10 m to account for the free radiation. The distance of the vortices to the center was chosen to be $r_0 = 1$ m and the density to be $\rho_0 = 1\,\text{kg/m}^3$. The circular intensity was chosen as $\Gamma = 2\pi\,\text{m}^2/\text{s}$, which results in a rotating speed of $\omega = 0.5\,1/\text{s}$. With a speed of sound of $c_0 = \sqrt{10}\,\text{m/s}$, the resulting wave length is $\lambda = 19.76$ m and the rotational Mach number $\text{Ma}_\theta = 0.158$. The mesh size on the circular path of the vortices was 0.03 m, at the interface it was 0.09 m and in the propagation region 1.67 m. Therefore each wave was resolved with over 20 linear elements. The time step used was $\Delta t = 0.09$ s and the total simulation time was 54 s (or about 11 rotations).

A numerical computation of the incompressible pressure fluctuations with (4.17) is not possible directly, since the incompressible pressure is unbounded at the center of the vortex cores, which results from the infinite velocity in the potential vortex core. This can be seen in the zero value in the denominator of (4.18) and (4.19) for $r = r_0$ and $2t\omega = 2\theta$. This leads to unphysical results in the numerical solution. The singularity in the vortex core is a known property of the potential vortex and some alternative vortex models are described in section A.3. They are used to model a more physical vortex behavior and are therefore better suited to be treated numerically. The modified equations for the incompressible pressure field used in this work are

$$\tilde{p}^{ic} = p_0 - \rho_0 \frac{\widetilde{\partial \Re F}}{\partial t} - \frac{1}{2}\rho_0 \left(\widetilde{u^2 + v^2} \right), \tag{4.21}$$
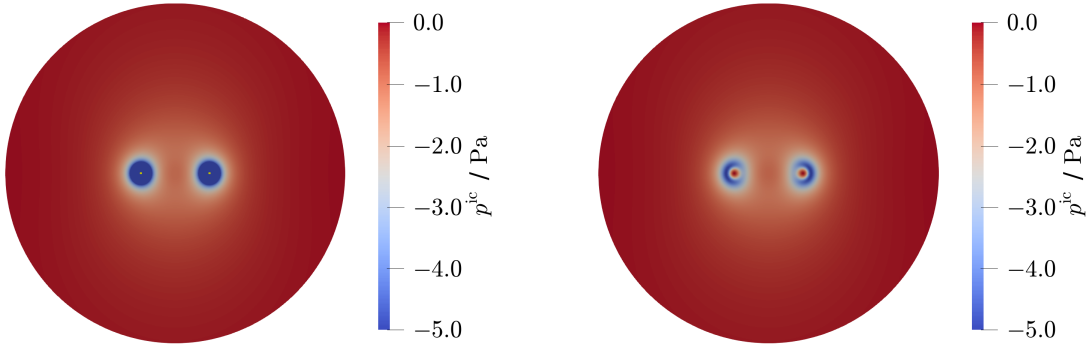
with

$$\frac{\widetilde{\partial \Re F}}{\partial t} = \frac{r_0 \omega \Gamma (r_0^2 - r^2 \cos(2t\omega - 2\theta))(r^4 + r_0^4 - 2r^2 r_0^2 \cos(2t\omega - 2\theta))}{\pi(r_c^2 + (r^4 + r_0^4 - 2r^2 r_0^2 \cos(2t\omega - 2\theta))^2)} \tag{4.22}$$

and

$$\widetilde{u^2 + v^2} = \frac{r^2 \Gamma^2 (r^4 + r_0^4 - 2r^2 r_0^2 \cos(2t\omega - 2\theta))}{\pi^2 (r_c^2 + (r^4 + r_0^4 - 2r^2 r_0^2 \cos(2t\omega - 2\theta))^2)}. \tag{4.23}$$

They were desingularized in a similar manner as the Scully vortex model, by the introduction of the constant r_c. Outside of the core, this model approximates the potential vortex. With a linear search, the constant was found to suite well for $r_c = 0.15$ m. The numerically computed incompressible pressure field from (4.17) is shown in Fig. 4.25. The mean pressure outside the vortices is $p_0 = 0$ Pa. The pressure is dropping towards the two vortex cores, due to the increasing velocity. The two small yellow dots in the middle of the vortices denote Not a Number (NaN) values that arise numerically due to the division with a zero value. The numerically computed incompressible pressure field from (4.21) is shown in Fig. 4.25b. The outer field is not altered, but in the vortex cores the pressure is reduced smoothly to the mean pressure.

The source terms are computed according to section 2.3.4 as the substantial derivative of the incompressible pressure. The numerical computation was done in two different ways. In the first simulation, a stationary mesh was used and the rotating pressure field was computed on the stationary source domain. In the second simulation, a stationary pressure field was computed on a rotating source domain. Since the mesh is stationary in the first simulation and the mean flow field is negligible the spatial derivative reduces to a simple time derivative. For the rotating mesh, the substantial derivative has to be computed with the grid velocity. Figure 4.26 shows the acoustic source terms for both simulations for the same moment in

(a) Original potential vortices with singularities in the vortex cores.

(b) Desingularized vortex cores with $r_c = 0.15\,\mathrm{m}$.

Figure 4.25.: Incompressible pressure field of the rotating vortex pair in the source region.

time. The time derivative on the stationary mesh, as well as the substantial derivative on the
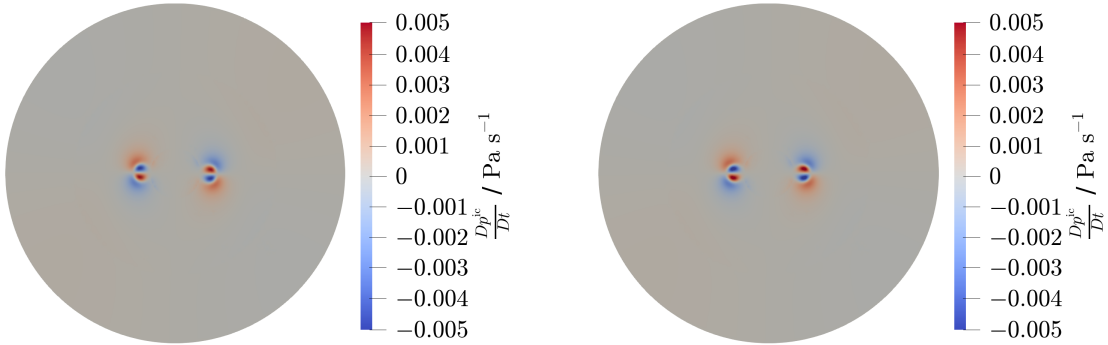
(a) Time derivative on the stationary mesh.

(b) Substantial derivative on the rotating mesh.

Figure 4.26.: Acoustic source term derived from the incompressible pressure field.

rotating mesh lead to the same acoustic source terms. From the acoustic source, the quadrupole structure can already be seen. In the middle of the sources the phase is changed, due to the desingularization.

For the acoustic propagation simulation, the propagation region and PML region were used additionally to the source region. In the simulation with the stationary mesh a conforming mesh interface was used. The fluctuating pressure field is shown in Fig. 4.27a. In the simulation with the rotating mesh a nonconforming interface had to be used as described in section 3.2.1. The result is shown in Fig. 4.27b. Both simulations show identical acoustic results and no influence of the interface is visible. The quadrupole radiation pattern can be seen clearly, and the wave length agrees with its prediction. Furthermore, the PML absorbs the outgoing

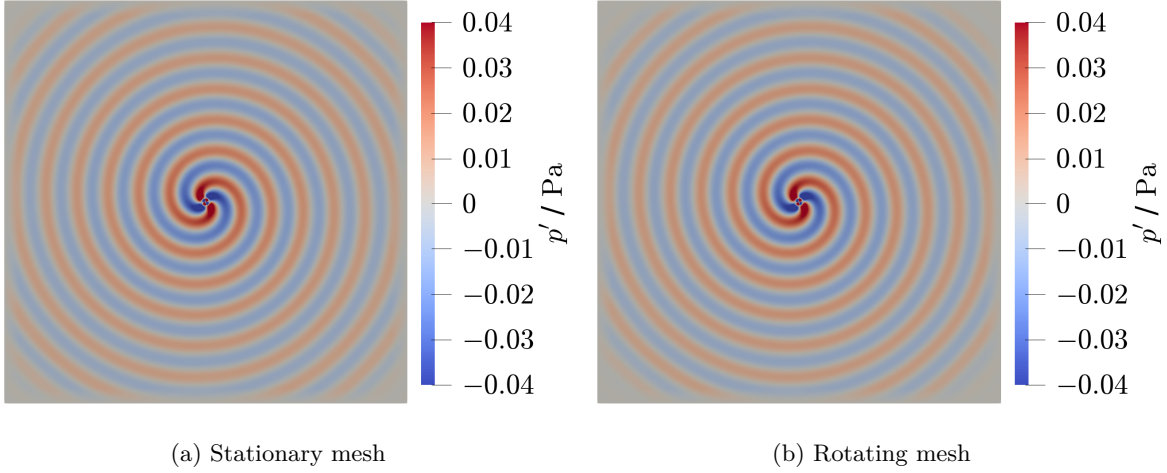(a) Stationary mesh

(b) Rotating mesh

Figure 4.27.: Acoustic pressure field of the propagation simulation on the stationary and rotating mesh.

waves without any visible reflection. In Fig. 4.28 the fluctuating pressure of both simulations is compared with the analytic solution. The evaluation point is a distance of 10 m from the center of rotation. The sources of the simulations are blended in slowly, which is the reason
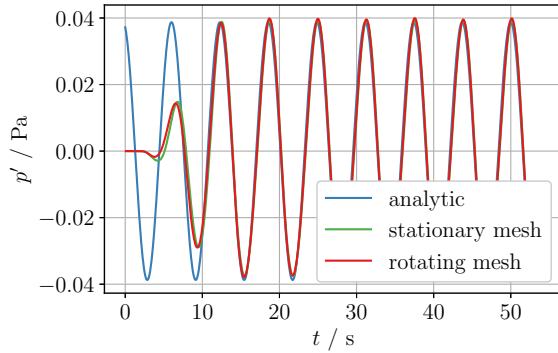

Figure 4.28.: Analytic solution (blue) compared with the simulation result from the stationary mesh (green) and the rotating mesh (red) in a distance of 10 m.

why the full amplitude is just reached after 15 s. In the blending time a small deviation between the stationary mesh (green) and the rotating mesh (red) can be seen. After that, almost no difference occurs between the two simulations. Compared to the analytical solution (blue) a small offset occurs in both simulations. This is interpreted as a result from the desingularization. This shows (for this specific application), that the implementation of the PCWE formulation, the nonconforming interfaces, the ALE formulation of the rotating domain

and the PML give correct results.

4.3.2. Computation of source terms

The computation of acoustic source terms involves the derivation of fluid quantities. Depending on the acoustic analogy, this may be spatial derivatives (like in (2.37)), time derivatives (like in (2.53)) or both (like in (2.55)), where the fluid quantities are commonly obtained not from analytical fields like in section 4.3.1, but from CFD simulations. All of these acoustic analogies can use a different acoustic mesh for the propagation simulation than the CFD mesh. Therefore, the question arises on which of those two meshes the derivation is more reasonable. In general the CFD mesh is finer and spatial resolution is lost by the interpolation on the acoustic mesh. But the coarser acoustic mesh reduces the computational effort of the derivatives.

The interpolation of the flow quantities from one mesh to another is a weighted mapping. Figure 4.29 illustrates the mapping of two values f_1 and f_2 on a common node with the weights a and b. The resulting value is $af_1 + bf_2$. If we apply a differential operator $\mathcal{D}$ on the initial
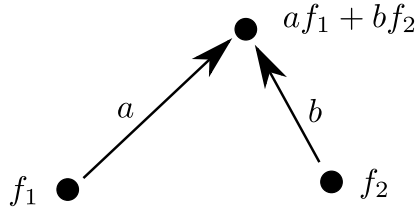

Figure 4.29.: Mapping of two values on one node.

quantities, and do the mapping, we obtain as a result $a\mathcal{D}f_1 + b\mathcal{D}f_2$. The same result is obtained if the mapping is permuted with the differential operator, as long as the operator is linear and the mapping is constant:

$$a\mathcal{D}f_1 + b\mathcal{D}f_2 = \mathcal{D}\left(af_1 + bf_2\right). \tag{4.24}$$

The differential operators are clearly linear for the above mentioned sources. Whether the mapping is constant or not, depends if the relation of target and original mesh are constant. For all rigid meshes this is satisfied. For the discrete computation, the derivative is approximated by

$$\mathcal{D}_\mathrm{h} = \mathcal{D} + e(h), \tag{4.25}$$

with an error $e(h)$ depending on the mesh size h. For the interpolation on a mesh with different mesh size $\tilde{h}$, (4.24) becomes

$$a\left(\mathcal{D}_\mathrm{h} + e(h)\right)f_1 + b\left(\mathcal{D}_\mathrm{h} + e(h)\right)f_2 = \mathcal{D}_\mathrm{h}\left(af_1 + bf_2\right) + \tilde{e}(\tilde{h}). \tag{4.26}$$

The results are equal except for the error of the derivative. For decreasing mesh sizes, the results become more and more similar. To reduce the numerical error, it is beneficial to do the derivative first and the interpolation second.

For the time derivative, there exists no dependence on the spatial resolution. For the validation example of section 4.3.1 with the pure time derivative as source term, the results of the

permutation of derivation and interpolation are shown in Fig. 4.30. The results are equal to the limit of machine precision.
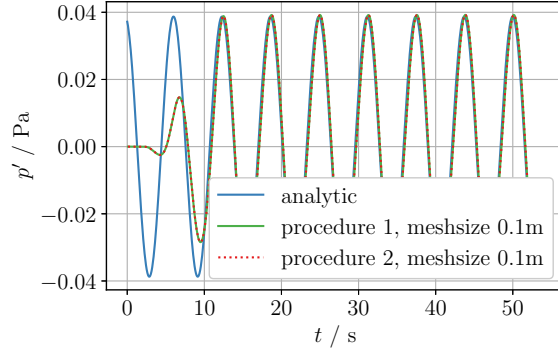

Figure 4.30.: Permutation of source derivation and integration.

Although it is in general more precise to do the derivatives first and the interpolation second, it can be beneficial to permute these two. The computational effort for the interpolation and derivation depend on the number of variables. For a mesh with N nodes an upper limit for the derivation order is $\mathcal{O}(N^2)$. For the interpolation on a target mesh with M nodes an upper estimation is $\mathcal{O}(MN)$. If the target mesh is coarser than the original mesh, it is computationally more efficient to do the interpolation first and the derivation second. It should be mentioned, that this are estimations for the upper limit. Special methods might reduce the computational effort for derivation and interpolation .

For the FE formulation, the acoustic sources have to be integrated. For (2.55), the weak form of the right hand side writes as

$$\int_\Omega \varphi \frac{Dp^{\mathrm{ic}}}{Dt} \, \mathrm{d}\Omega \,. \tag{4.27}$$

Here a permutation of differentiation and integration may influence the boundaries of the integral. In 1D this is seen as the Leibniz integral rule. In 3D this is described as the Reynolds transport theorem. For a scalar quantity f it can be written with the normal vector n_i and the velocity of the boundary v_i and the flux over the boundary can be rewritten with Gauß integral theorem

$$\frac{d}{dt} \int_{\Omega(t)} f \, \mathrm{d}\Omega = \int_{\Omega(t)} \frac{\partial}{\partial t} f \, \mathrm{d}\Omega + \int_{\Gamma(t)} f v_i \cdot n_i \, \mathrm{d}\Gamma = \int_{\Omega(t)} \left(\frac{\partial}{\partial t} f + \frac{\partial}{\partial x_i} (f v_i) \right) \, \mathrm{d}\Omega \,. \tag{4.28}$$

For general movements of the mesh, the permutation of integration and differentiation is not equal. In the special case of a cylindrical rotating domain the boundary velocity is orthogonal to the boundary and therefore

$$v_i \cdot n_i = 0 \,, \tag{4.29}$$

which leads to

$$\frac{d}{dt} \int\limits_{\Omega(t)} f \, \mathrm{d}\Omega = \int\limits_{\Omega(t)} \frac{\partial}{\partial t} f \, \mathrm{d}\Omega \,. \tag{4.30}$$

So, for the special case of cylindrical rotating domains, the integration and differentiation can be permuted.

In this work, the source computation was done before the interpolation and integration. This was done for increased accuracy but also because the sources were then used to interpolate on different meshes afterwards, without the need to do the source computation every time.

4.3.3. Interpolation

For the transfer of the results from the CFD mesh to the CAA mesh an interpolation is needed. In general the CFD mesh is finer than the CAA mesh since it has to resolve fine turbulent structures. For the CAA mesh the limiting quantity is the (for low Ma number) relatively large acoustic wave length. As long as the CFD mesh is finer than the CAA mesh, a cell centroid based interpolation can be used. It interpolates the nodal values of all CFD cells contained in a CAA cell in a FE sense. If the CFD meshes are at some point coarser than the CAA mesh, some CAA cells do not contain complete CFD cells, which leads to problems as pointed out in [50]. Some similar investigations have been done in [56]. For this case an improved interpolation algorithm, the so called cut-volume cell approach, can be used. It uses a volume weighting of the CFD cells contained in the CAA cell to overcome this restriction.

The following investigations were already published in [99]. In order to determine how coarse the acoustic grid can be compared to the CFD grid, the cut-volume cell approach is verified numerically. For this verification, two-dimensional analytic pressure fields are used, where the pressure distributions are given in (4.31)–(4.33). These equations correspond to a monopole, dipole, and quadrupole, respectively, and are determined solely by the coordinates x and y, and the spatial parameter $\sigma = 0.75 \,\mathrm{m}$.

$$p_{\mathrm{MP}} = \frac{1}{\sqrt{2\pi\sigma^2}} \, e^{-\frac{x^2+y^2}{2\sigma^2}} \tag{4.31}$$

$$p_{\mathrm{DP}} = \frac{-x}{\sqrt{2\pi\sigma^2} \cdot \sigma^2} \, e^{-\frac{x^2+y^2}{2\sigma^2}} \tag{4.32}$$

$$p_{\mathrm{QP}} = \frac{xy}{\sqrt{2\pi\sigma^2} \cdot \sigma^4} \, e^{-\frac{x^2+y^2}{2\sigma^2}} \tag{4.33}$$

These pressure fields are used as acoustic source fields, which are prescribed on the source region of the source mesh (see Fig. 4.31a). The simulation region is identical to section 4.3.1. All used meshes are unstructured meshes. The propagation domain is discretized in a way that allows to correctly resolve the acoustic wave propagation. The cell size of the source mesh is chosen such that it is half of the cell sizes of the finest target mesh, which is also used as the reference mesh.

Based on this source mesh, the pressure is interpolated on the acoustic target mesh. For the numerical investigation, different mesh resolutions are used as acoustic target meshes. Figures 4.31b and 4.31c show the finest and coarsest target mesh. The different mesh sizes of the

(a) Mesh of the analytic source.

(b) Finest target mesh.
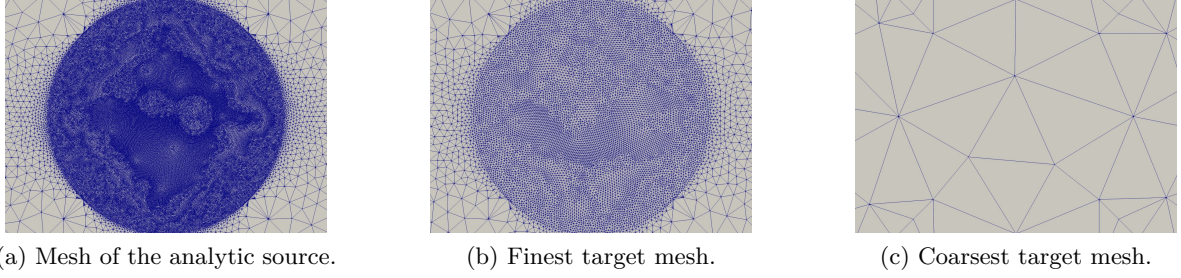

(c) Coarsest target mesh.

Figure 4.31.: Different meshes for the interpolations, with a very fine mesh of the analytic source, and the finest and coarsest target mesh.

source domains used for this verification are listed in Tab. 4.4. The last column of this table describes the relation of the element size to the spatial parameter σ of the analytic sources.

Table 4.4.: Different meshes used in the source region to investigate the cut-volume cell interpolation.

	Number of Cells	Number of Nodes	Element size in m	Element size / σ
Reference Mesh	77416	39021	0.05	$0.0\bar{6}$
Mesh 1	18378	9346	0.1	$0.1\bar{3}$
Mesh 2	4626	2392	0.2	$0.2\bar{6}$
Mesh 3	1160	621	0.4	$0.5\bar{3}$
Mesh 4	292	167	0.8	$1.0\bar{6}$
Mesh 5	82	52	1.6	$2.1\bar{3}$
Mesh 6	56	37	2	$2.\bar{6}$
Mesh 7	12	11	4	$5.\bar{3}$

The interpolated pressure field on the acoustic target mesh is then used as a right hand side for an acoustic propagation simulation, which is solved in the frequency domain. The evaluation of the acoustic radiation for the three different source fields is shown in Fig. 4.32. The amplitudes are scaled with the solution of the reference mesh. It can be seen, that the acoustic result is almost identical for mesh sizes up to 0.8 m, or to a ratio of the mesh size to spatial parameter σ of about 1, respectively. For larger ratios of mesh size to σ, the radiation patterns are represented correctly; however, the amplitude clearly shows deviations from the real value. The interpolation only fails for the coarsest mesh with a mesh size of 4 m. From these results, it can be seen that the cut-volume cell approach can be applied to a large range of acoustic mesh sizes. The upper limit of the acoustic mesh size is given by the source size, which is the spatial parameter σ in this verification example.

In addition to the interpolation with the cut-volume cell approach, the same numerical experiment was done with the cell centroid interpolation approach. Since the same meshes were used, the difference in the acoustic radiation is solely resulting from the interpolation. The difference of the acoustic results are shown in Fig. 4.33. The maximum difference between
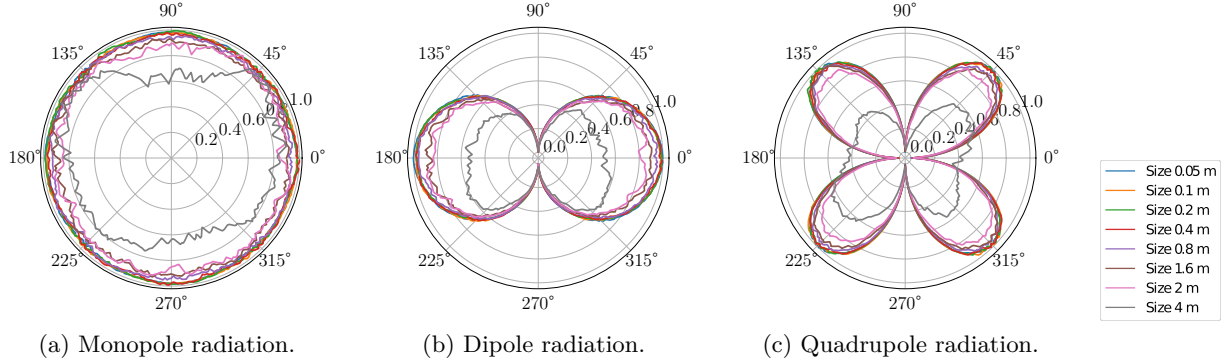
(a) Monopole radiation.   (b) Dipole radiation.   (c) Quadrupole radiation.

Figure 4.32.: Results of the different discretizations for the generic sources.

(a) Monopole radiation differ-   (b) Dipole radiation difference.   (c) Quadrupole radiation differ-
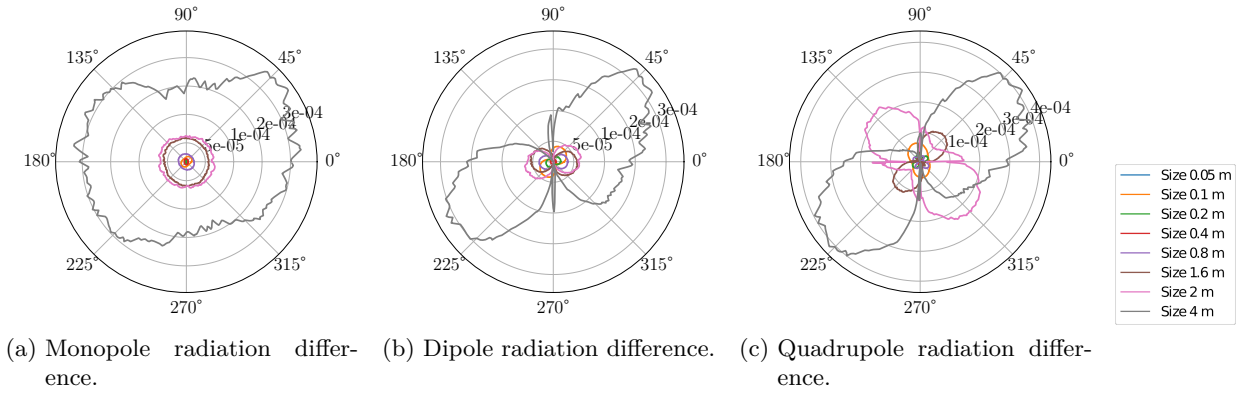ence.   ence.

Figure 4.33.: Difference between the cut-volume cell and cell centroid interpolation approach
for the generic sources.

both approaches is for the coarsest mesh for all three sources around $4 \cdot 10^{-4}$. The monopole source shows a unidirectional difference, the other two sources show nonuniform differences. Up to a mesh size of $0.8\,\text{m}$ all differences (except for the $0.1\,\text{m}$ mesh of the quadrupole source) are below $5 \cdot 10^{-5}$.

4.3.4. Acoustic domain

For the application to fan noise prediction, the geometry has to be represented in the acoustic domain. This means, that not only the source domain has to be represented correctly, but also scattering elements in the propagation domain. Therefore, the used acoustic domain contains all scattering elements like the fan, duct, nozzle, shaft, strut and engine, but the propagation domain was cropped to reduce the computational effort. An overview of the acoustic domain is shown in Fig. 4.34. The rotating region (in red) is exactly the same as in the CFD simulation. The inlet region is cropped to still include all the microphones of the measurement (in black) and the outlet region is dimensioned to contain the engine. The microphones are arranged in front of the nozzle on a half circle with a radius of $1\,\text{m}$. The whole domain is surrounded
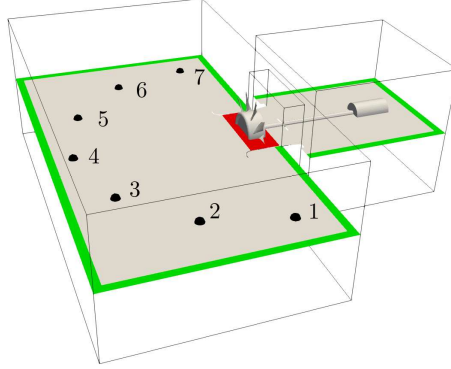
Figure 4.34.: Acoustic mesh regions, with the PML in green, stationary inlet and outlet regions in gray, the rotating region in red and the microphone positions in black.

with a Perfectly Matched Layer (PML) [51, 59] displayed in green to satisfy the free radiation. The resizing of the domain is possible, since the wall in the inlet chamber were non reflecting (as it was covered with acoustic absorbers) and the outlet region was a free radiation into the measurement hall.

4.3.5. Mesh discretization

The accuracy of the numerical solution depends on the used mesh discretization and the used polynomial order of the finite elements. The finer the mesh becomes, the more accurate the solution becomes. In contrast to the CFD mesh, where regions with strong gradient in the solution need mesh refinement (like the boundary layers), the acoustic mesh needs a uniform mesh size to preserve the acoustic waves in the whole propagation domain. As a rule of thumb the smallest acoustic wavelength has to be discretized with 10 to 20 points in space and the shortest period has to be discretized with 10 to 20 steps in time. From the measured spectrum in Fig. 4.3 the tonal components of the fan can be seen under 1 kHz, where above broadband noise occurs. In the broadband noise region [123] provides beamforming results. Therefore, the main information that can be gained from simulations is below 2 kHz. In this work three different mesh resolutions were used in the acoustic propagation simulations. For the finest resolution of the propagation domain a spatial resolution of 15 linear elements was chosen for a frequency up to $f_{\max} = 1500\,\mathrm{Hz}$. The wave length computes as

$$\lambda = \frac{c}{f_{\max}} \tag{4.34}$$

and with a standard speed of sound $c = 343\,\mathrm{m/s}$ and the maximum frequency the wavelength computes as $\lambda = 0.228\bar{6}\,\mathrm{m}$. Therefore a maximum mesh size of $h \approx 0.015\,\mathrm{m}$ was used. To investigate the effect of coarser meshes a second mesh with a maximum frequency of $f_{\max} = 1000\,\mathrm{Hz}$ was chosen, which leads to a maximum mesh size of $h \approx 0.023\,\mathrm{m}$ with 15 elements per wave length. A third mesh for the same maximum frequency and just 10 elements, which

leads to $h \approx 0.034\,\mathrm{m}$ was chosen.

For harmonic simulations an estimation for the needed discretization exists. A relation between the element order q, the wave number k, the spatial resolution h and constant c is given in [6] as

$$q + \frac{1}{2} > \frac{kh}{2} + c(kh)^{1/3}\,. \tag{4.35}$$

The constant can be assumed as $c = 1$. This function is displayed in Fig. 4.35. For a given element order, the maximum wave number can then be extracted. For the chosen mesh sizes,
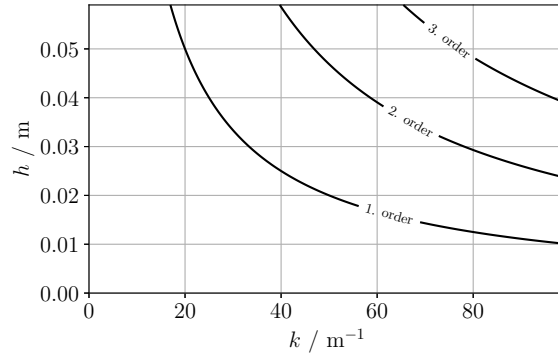

Figure 4.35.: Relation of the spatial resolution h and the wave number k.

this inequality gives maximum frequencies for the fine mesh of $f_{\max} = 3607.7\,\mathrm{Hz}$, for the middle mesh of $f_{\max} = 2352.8\,\mathrm{Hz}$ and for the coarse mesh of $f_{\max} = 1591.5\,\mathrm{Hz}$. The mesh statistics for the acoustic simulations are shown in Tab. 4.5.

Table 4.5.: Different meshes used for the acoustic propagation simulation.

	Total elements	Max. element size	Elements rotating	Elements stationary
Mesh 1	1020318	$0.034\,\mathrm{m}$	857422	162896
Mesh 2	1697374	$0.023\,\mathrm{m}$	857738	839636
Mesh 3	3929011	$0.015\,\mathrm{m}$	1188196	2740815

The numerical accuracy and efficiency depends not only on the resolution, but also on the kind of used elements. In the FEM the hexahedral elements are best in terms of accuracy an efficiency. To improve the computations, the large inlet and outlet regions are meshed with pure hexahedral elements. These regions are mainly for the propagation and have little to no contribution of sound producing source terms. In the inlet region it is possible to create a purely block structured mesh, but in the outlet region the complex geometry of the strut leads to highly skewed elements. Therefore, a combination of a block structured mesh and swept mesh blocks is used. Surface meshes can always be generated with pure quadrilateral element
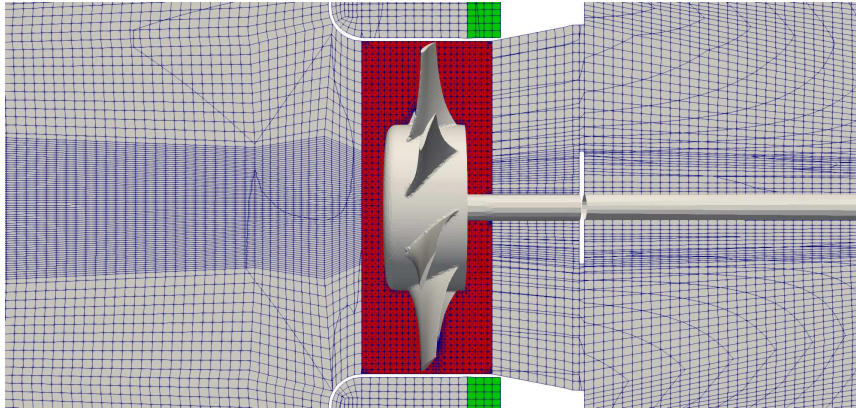
Figure 4.36.: Acoustic mesh, with pure hexahedral meshes in the inlet and outlet region (gray) and a tethrahedral mesh in the rotating region (red).

and these elements are then extruded to a three dimensional block with pure hexahedral elements. The acoustic meshes were created with ANSYS ICEM CFD 18.0.

The rotating region contains the fan, which is a very complex geometry, and therefore very difficult to mesh in a structured way. In this region the ability of FEM to use different kinds of elements is very beneficial and this region can be meshed with tetrahedral elements. This leads to an unstructured mesh with a larger number of elements but it decreases the time used for meshing and improves the overall mesh quality. The acoustic mesh is shown in Fig. 4.36, with the hexahedral inlet region on the left, the tethrahedral rotating region in the middle and the hexahedral outlet region on the right.

The needed mesh size in the source region is not known a priori, since it is not only relevant for the wave propagation but also for the resolution of the occurring acoustic source terms. As shown in section 4.3.3 the sources can be resolved in the order of the mesh size. So the first guess is to discretize this region with the same resolution as the propagation region and to refine where small scale source terms are assumed. This is mainly in the tip gap and close to the boundary of the fan. Afterwards a mesh refinement is done in a similar way to a mesh convergence study in CFD. Results of this investigation will be discussed in section 5.7.

An important aspect in the meshing process is the underlying geometry. In the CFD meshing this is mostly the geometry from a CAD program. Since the meshing always includes some kind of defeaturing, where small details are neglected, the underlying geometry for the CAA meshing should be the defeatured geometry. This is done by taking the surface mesh from the CFD simulation and using this as the underlying geometry.

4.3.6. Blending

In numerical simulations the computation domain has to be finite. This leads to an introduction of additional boundaries that truncate the physical field. The truncation of the areoacoustic source changes the acoustic solution, which increases the computational error. In the FWH analogy such a domain truncation can be interpreted as an additional surface source. Such truncations occur often in the turbulent wake of flow simulations, where hydrodynamical fluc-

tuation are convected downstream without actually radiating sound. If these fluctuation pass a truncation surface, additional acoustic sources occur. This truncations may occur due to the outflow boundary of the CFD simulations or a numerical truncation of the source domain. For an abrupt truncation of the source domain some correction techniques are derived (for example [78]). But sometimes the truncation of acoustic sources is desirable to reduce the impact of non-physical sources. This can be if just some sources should be investigated, but more often non-physical sources result from numerical errors. For example in the far field, no acoustic source terms should occur. For this purpose it is common to use blending functions for example [87] or [14] to suppress unphysical sources, because a smooth blending function reduces the unphysical sources in the blending area and leads to less unphysical acoustic radiation.

In this work, two different blending functions were investigated. The first is shown in Fig. 4.37. It is designed to utilize the sources in the rotating domain and drop sharply to cancel out the sources before the nonconforming interfaces. This should reduce the unphysical sources, which occur due to numerical errors at the interfaces. The second blending function
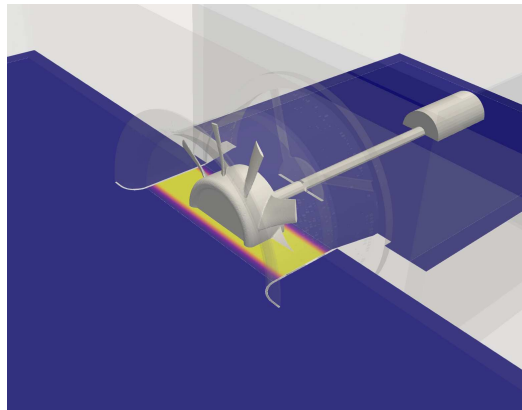

Figure 4.37.: First blending function reducing the sources steeply before the nonconforming interface.

is shown in Fig. 4.38. It is designed to reduce the sources slowly behind the interfaces. This should reduce unphysical sources, which occur in the wake of the fan due to the grid coarsening. To blend the sources, the blending functions are multiplied with the actual source value. In the actual source domain, the blending function is one, where power of cosine functions were used to smoothly reduce the values to zero.

A similar truncation of the simulation occurs in time, where the abrupt beginning and end of the simulation can be seen as a multiplication of the sources with a Heavyside function in time. For the end of the simulation this is negligible, since this jump of acoustic sources can not propagate anymore. But at the beginning of the simulation, this can lead to high acoustic impulses propagating through the domain. In Fig. 4.39 the used blending function in time is shown in blue. For the very first 0.5 ms all source terms are suppressed. This is to remove any numerical artifacts from the beginning of the simulations, like time derivatives with not enough time steps for the complete derivation stencil. In the second 0.5 ms, the sources are increased smoothly to their actual value. In contrast to that, a second simulation used no
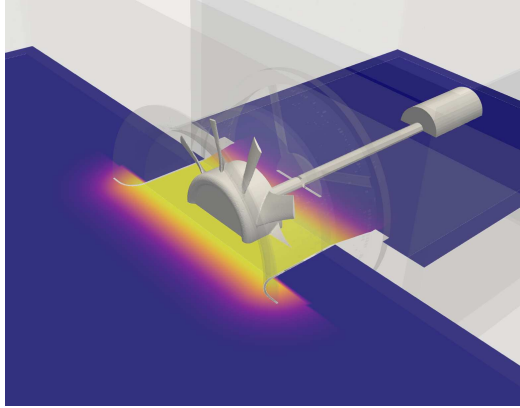
Figure 4.38.: Second blending function reducing the sources slowly after the nonconforming interfaces.
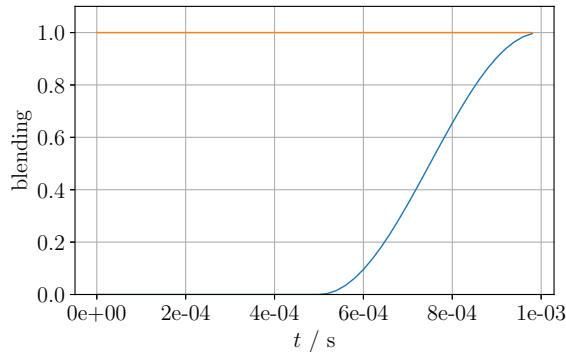

Figure 4.39.: Blending in time, with complete suppression of sources at the beginning of the simulation and a smooth transition afterwards.

blending, which is equivalent to a constant blending function (in orange).

4.3.7. Ffowcs-Williams and Hawkings analogy of incompressible flow simulations

The application of the original FWH analogy yields some challenges in the simulation. The most significant one is that the evaluation at the retarded time makes it necessary to store the time history of the field quantities. Especially for the volume integral this can led to large amounts of data. One possibility to circumvented this is by the use of the hull formulation. When the hull is chosen large enough to contain all main sound sources, it is enough to just evaluate the surface integrals, which also reduces the necessary data. But when a large hull surface is used, it has to be ensured that the acoustic fluctuation are propagated correctly until the surface. Furthermore, the integrals of the surfaces do not distinguish fluctuating flow and acoustic quantities. So, if vortices are convected through the integration surface, this

fluctuations are propagated in combination with the acoustic fluctuations. Another possibility to circumvent the storage of large amounts of field quantities is to use the surface formulation and simply neglect the volume terms. This is a valid assumption for low Mach number flows. In StarCCM+ Farrassat's formulation 1A [16, 35] is implemented. This formulation gives the total fluctuating pressure from the surface as a contribution from the thickness and the loading of the surface

$$p'_S(\mathbf{x}, t) = p'_T(\mathbf{x}, t) + p'_L(\mathbf{x}, t).$$ (4.36)

The thickness term is given as

$$p'_T(\mathbf{x}, t) = \frac{1}{4\pi} \left(\int_\Gamma \left[\frac{\rho_0 \dot{U}_n}{r(1 - \mathrm{Ma}_r)^2} \right] \, \mathrm{d}\Gamma \right. $$
$$\left. + \int_\Gamma \left[\frac{\rho_0 U_n \left(r\dot{\mathrm{Ma}}_r + c_0(\mathrm{Ma}_r - \mathrm{Ma}^2) \right)}{r^2(1 - \mathrm{Ma}_r)^3} \right] \, \mathrm{d}\Gamma \right), $$ (4.37)

with the distance from source to receiver $r = |\mathbf{x} - \mathbf{y}|$. The Mach number Ma_r in direction of the receiver, the dot quantities are derivatives with respect to the source time and the terms in square brackets are evaluated at the retarded time. The vector U_n is defined as

$$U_n = \left((1 - \frac{\rho}{\rho_0})v_i + \frac{\rho}{\rho_0}u_i \right) \cdot n_i.$$ (4.38)

The loading term is given as

$$p'_L(\mathbf{x}, t) = \frac{1}{4\pi} \left(\frac{1}{c_0} \int_\Gamma \left[\frac{\dot{L}_r}{r(1 - \mathrm{Ma}_r)^2} \right] \, \mathrm{d}\Gamma + \int_\Gamma \left[\frac{L_r - L_M}{r^2(1 - \mathrm{Ma}_r)^2} \right] \, \mathrm{d}\Gamma \right.$$
$$\left. + \frac{1}{c_0} \int_\Gamma \left[\frac{L_r \left[r\dot{\mathrm{Ma}}_r + c_0(\mathrm{Ma}_r - \mathrm{Ma}^2) \right]}{r^2(1 - \mathrm{Ma}_r)^3} \right] \, \mathrm{d}\Gamma \right), $$ (4.39)

with the blade loading vector

$$L_i = (p - p_0) \cdot n_i + \rho \cdot u_i(u_n - v_n),$$ (4.40)

which is applied in the direction of the receiver $L_r = L_i \cdot r_i$ and the direction of the surface movement $L_M = L_i \cdot v_i/|\mathbf{v}|$. The terms of order $1/r$ are considered the far field terms and the terms of order $1/r^2$ are considered the near field terms. For transient rotating motion Farrasad's formulation 1A is implemented in StarCCM+ for impermeable integration surfaces only. This means, that the integration surfaces have to coincide with solid surfaces and the fluid velocity and normal velocity are equal and therefore the equations simplify with $u_n = v_n$.

A further simplification occurs for low Mach number flow, where the flow equations are considered to be incompressible. With this simplification, the density reduced to a constant and acoustic waves can not be resolved. Therefore the hull formulation can not be used for incompressible simulation data and the surface formulation is the only viable choice. Theo-

retically the constant density leads to an infinite speed of sound, since pressure fluctuations propagate instantly through the whole domain. This means, that in the surface formulation all $1/c_0$ terms vanish. Therefore, the acoustic results are just valid for compact sources.

Results

In this section, the results of the applied hybrid aeroacoustic methods are going to be shown. First, the influence of the surrounding geometry is investigated for the setup. Second, the influence of different numeric procedures in the hybrid aeroacoustic method on the acoustic result is investigated. Third, the acoustic results are compared with prediction methods of class 1 and 2. Finally, the acoustic source terms of the hybrid aeroacoustic method are investigated to gain insight in the acoustic source mechanisms of the setup.

5.1. Acoustic directivity of the duct

The acoustic result in the measurement chamber depends on the radiated sound of the fan and the interaction with the surrounding geometry. The geometry influences the acoustic directivity of a source by reflections and diffractions of the propagating waves. The interactions of the acoustic wave and the geometry is dependent on the proportion of one to another. For the acoustic wave, the wavelength λ is the characteristic parameter and for the geometry the duct diameter D is a reasonable choice. As long as the wavelength is larger than the duct diameter, the interaction of the acoustic propagation with the geometry has a small effect. But when wavelength and duct diameter are similar in size, interaction can be expected.

The directivity was computed with a harmonic simulation on the fine acoustic mesh, where an artificial excitation was applied on a single node on the rotation axis in front of the fan. This has the behavior of a monopole source, and for free radiation the resulting directivity is uniform. The amplitude was evaluated at the microphone positions of the measurement setup. The result is displayed in Fig. 5.1 for different relations of the wave length and the duct diameter. The directivity in the measurement chamber is displayed in the left half of the diagram, with the rotational axis of the fan at the horizontal line. Outside of the measurement chamber (respectively on the right half of the diagram) there were no anechoic conditions in the measurement. Therefore, the results were just evaluated inside the chamber. It can be seen that for lower frequencies the radiation is almost non directional. In Fig. 5.1a the

(a) $D = 0.15\lambda$

(b) $D = 1.03\lambda$

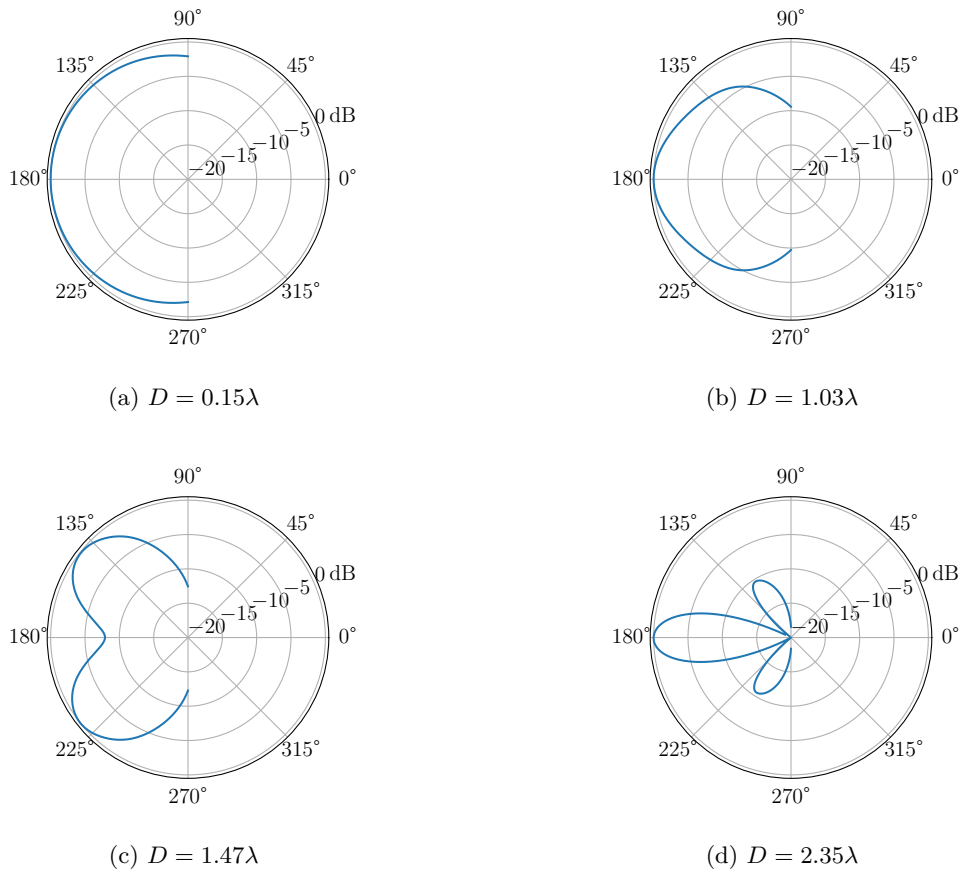(c) $D = 1.47\lambda$

(d) $D = 2.35\lambda$

Figure 5.1.: Directivity depending on the wave length

wavelength is much larger than the duct diameter and therefore almost not influenced by it. From the measurements it is known that in this region, the tonal components of the acoustic spectrum occur. Therefore, the influence on the directivity is supposed to be small for the tonal components. When the wavelength comes in the range of the duct diameter (which is at 700 Hz) the acoustic radiation starts to be influenced by the duct and nozzle geometry and the directivity towards the rotational axis increases. From the measurements it is known that above this frequency the acoustic spectrum contains mostly broadband noise. Therefore, the broadband noise is supposed to be influenced by the geometry. With higher frequency and therefore shorter wave length side lobes start to form. For $D = 1.47\lambda$ (which is at 1000 Hz) this leads to a directivity, which has its main lobes not at the rotational axis but at 40° to it. For $D = 2.35$ (which is at 1600 Hz) a very strong directivity towards the rotational axis forms, where the side lobes are about 10 dB smaller than the main lobe. This directivity behavior is similar to a loudspeaker mounted in a wall [46] or a moving piston [86]. Additionally to that, the nozzle has an amplifying effect on the result, since it is almost formed like an exponential horn [84].

5.2. Comparison with Class 1 and 2 methods

A comparison of the measured sound power level and prediction from class 1 and 2 is shown in Tab. 5.1. The two methods of class 1 are in a range of ± 2 dB, where VDI 2081 is underestimating and VDI 3731 is overestimating the emitted sound power level. The best agreement with the measurement has the prediction of Sharland, which differs just 0.9 dB. From (2.8) it can be derived that the contribution from the turbulent inlet accounts for 94.3 % of the sound contribution. This is mainly dependent on the turbulent intensity of the inflow. The vortex shedding accounts for another 5.7 % and the influence of the turbulent boundary layer is marginal with a contribution of 0.03 %.

Table 5.1.: Predicted sound power level from class 1 and 2 methods compared with the measurement results.

	L_W dB	ΔL_W dB
Measurement	87.3	–
VDI 2081	85.6	1.7
VDI 3731	88.7	1.4
Sharland	86.4	0.9

A comparison of the measured power spectral density and the prediction of Költzsch is shown in Fig. 5.2. The measurement result is obtained from the microphone position 4, which is one meter in front of the rotor on the axis of rotation. The black line shows the measurement result of the whole measurement time of 30.0 s. The spectrum was calculated with a Welch's algorithm using a Hanning window and 50 % overlap to improve the result quality, since the measurement result is always flawed with noise.
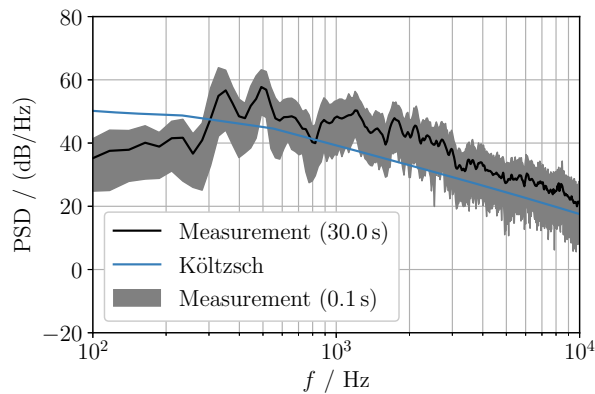

Figure 5.2.: Comparison of the Költzsch prediction method with the measurement results.

The grey band shows the bandwidth of the measurement signal cut in 300 single signals each with a measurement time of 0.1 s. This is a realistic signal length for simulations and should give an impression on the different behaviors of measurement and simulation results and is not meant to be a confidence interval. The measurement result is noisy, but can use the averaging

of the Welch algorithm to get a better result. Hence, the sharp peaks from the BPF and its harmonics are not visible in the spectrum. The main two visible peaks in the figure are the subharmonic peaks.

The prediction of Költzsch is beginning at 50 dB at 100 Hz and slowly falling in the low frequency range. Above 150 Hz and again above 600 Hz the slope is getting steeper. The low frequency spectrum is overestimated and the tonal components can not be reproduced by this method. In the higher frequency range, the estimation converges towards the measurement, but the slope is not met.

The class 1 and 2 methods give predictions for the sound power level, with very little effort. For the not optimized fan geometry, the agreement with the measurements is surprisingly good. On the one side this means that for acoustically optimized fans the agreements is supposed to be less good, since the measured sound would be reduced but the prediction of these methods is not changed. On the other side, nothing keeps us from adapting the used formulas to account for the acoustic "quality" of a fan, since that are (semi-)empirical formulas anyways. A disadvantage of this prediction methods is that they are only able to predict the sound power level at the design point. The maximum sound power level for the given fan was measured at a volume flow rate of $\dot{V} = 1.0 \, \mathrm{m^3/s}$ with a value of 93 dB. The VDI 3731 predicts at this point $L_\mathrm{W} = 88.7 \, \mathrm{dB}$, an almost similar sound power level as in the design point and the VDI 2081 predicts $L_\mathrm{W} = 84.6 \, \mathrm{dB}$ and therefore predicts a too low value.

5.3. Comparison with the Ffowcs-Williams and Hawkings analogy and the perturbed convective wave equation

In this section, the results of the PCWE equation and FWH integral solution of the complete simulation are shown at the different microphone positions. The results were sampled after 5 revolutions of the rotor and cover 7.5 revolutions (respectively 0.3 s). For the PCWE equation the acoustic propagation was computed on the coarse mesh and the first blending function was used. The results at the different microphone positions are displayed in Fig. 5.3, where the blue curve shows the result from the acoustic propagation simulation with the PCWE equation and the yellow curve shows the result of the FWH acoustic analogy computed in StarCCM+. The microphone position 1 is shown in Fig. 5.3a, which is the outermost position. The low frequency range is underestimated by both prediction methods. This can result from the coarse frequency resolution due to the short simulation time. The first subharmonic peak is underestimated by the PCWE analogy, but the FWH analogy meets the measurement well. The second subharmonic peak is met by both analogies, and from 1 kHz to 2.5 kHz the graph of both analogies are similar, but the PCWE equation has one peak at 1.7 kHz. Above 2.5 kHz the PCWE result drops sharply, where the FWH result stays at the same level but gets more and more noisy. Similar behavior, but at a higher amplitude, can be observed for microphone position 2 (Fig. 5.3b) and 3 (Fig. 5.3c), which are closer to the axis of rotation. For this two positions, the low frequencies are predicted better by the FWH analogy, but the PCWE analogy is a bit closer to the measurements in the higher frequency range. Microphone position 2 shows the same peak at 1.7 kHz as position 1 and an additional peak at 4.2 kHz. For position 3 these peaks are not visible. Microphone position 4 is directly on the axis of rotation (Fig. 5.3d). The PCWE analogy is slightly overestimating the frequency range between 500 Hz and 5 kHz, where

the FWH analogy is underestimating up to a frequency range of 3 kHz after which the signal is dominated by noise. At this location, the largest differences between the two prediction methods occur. The microphone position 5 to 7 are arranged symmetrically to the positions 3 to 1. Although the positions are symmetrically, the result is not completely identically (in the measurement and in the simulation).

Summarizing it can be said that the FWH analogy yields better results for the first subharmonic peak and gives reasonable results up to a frequency of 2-3 kHz. Above that, maybe the results are distorted because of the simplifications of the surface formulation with the incompressible flow simulation. In the higher frequency range, this analogy is underestimating the PSD and the most differences to the measurement occur directly at the axis of rotation. This might be due to the influence of the surrounding geometry. At low frequencies this influence is small but at high frequencies, the amplitudes directly in front of the nozzle get increased. The PCWE analogy is closer to the measurements in the high frequency range, but underestimating the first subharmonic peak. Since this is estimated better with the FWH analogy, it can be assumed that it is not a problem of underlying CFD simulation. Furthermore, due to the high resolution it is unlikely that it is a problem of the acoustic propagation simulation. For the first subharmonic peak, the wavelength is $\lambda \approx 1$ m and even with the coarse discretization of $h = 0.034$ m this means that the smallest wavelength is discretized with 29 linear elements, which is a very fine resolution. It may be that the difference results from the computation of the source terms where the mean velocity was neglected in the formulation. This is because the mean velocity in the stationary domain is not consistent with the mean velocity of the rotating domain. Theoretically a phase averaged mean velocity would be needed, but this violates the splitting in a constant mean velocity and fluctuating velocity in (2.45). Since the FWH analogy is incorporated in the flow solver, it uses very little additional effort to obtain these results, compared to the PCWE analogy, but it can not take the surrounding geometry into account and does not enable an investigation of the acoustic source mechanisms. The outermost microphone positions are hardest to predict in the high frequency range for both analogies.

In addition to the spectral analysis of both prediction methods, the time signal can be used to compute the over all sound power level with (4.1). The sound power level gives an insight how good the prediction agrees with the measurement in an energetic sense. The results are shown in Tab. 5.2. The PCWE method has a deviation of only 0.6 dB compared to the measurements

Table 5.2.: Predicted sound power level from the FWH and PCWE methods compared with the measurement results.

|	L_{W} dB	ΔL_{W} dB
Measurement	87.3	–
PCWE	86.7	0.6
FWH	85.2	2.1

and is therefore closer to the measurement results as the prediction methods of class 1 and 2. The FWH analogy has a deviation of 2.1 dB compared to the measurements and has therefore a larger deviation as the prediction methods of class 1 and 2, but this may result from to the used simplifications described section 4.3.7. The better agreement of the PCWE prediction
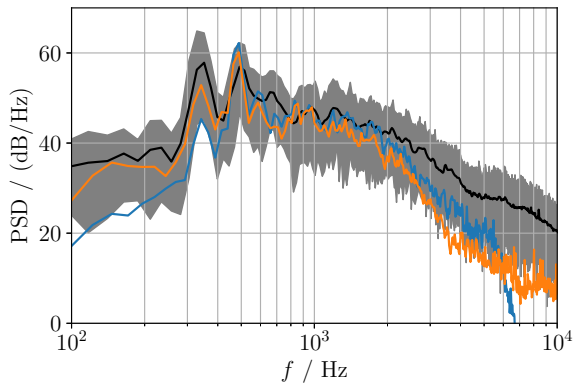
origins from the higher predicted PSD levels at the second subharmonic peak and in the mid to high frequency range.
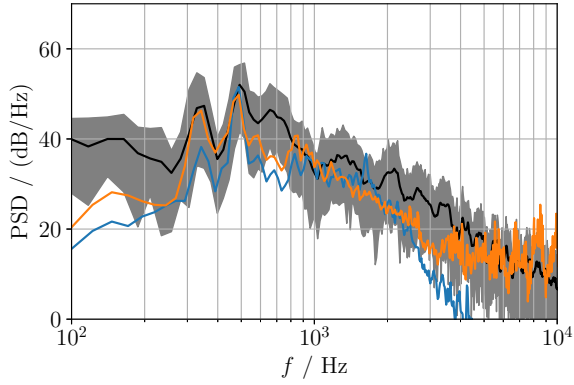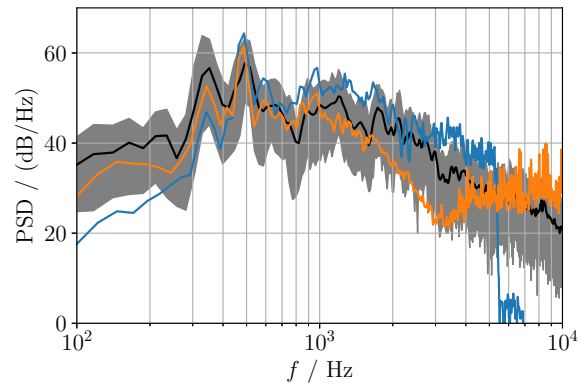

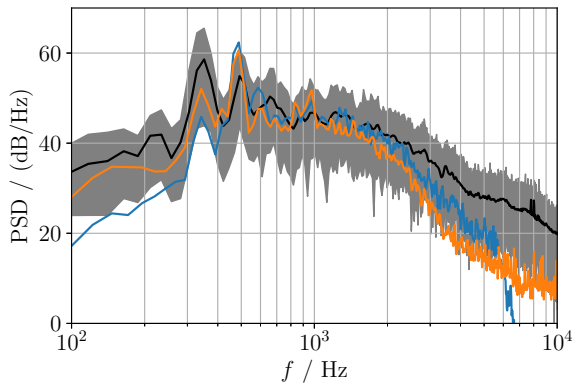(a) Microphone position 1
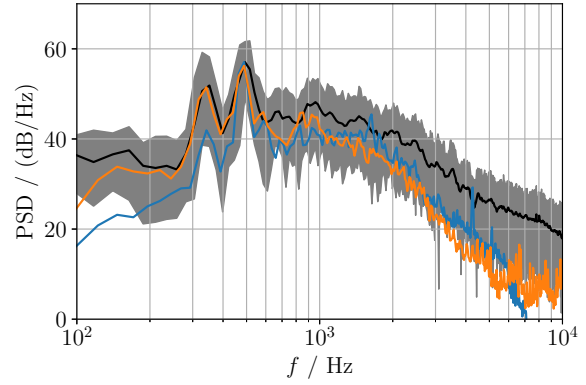
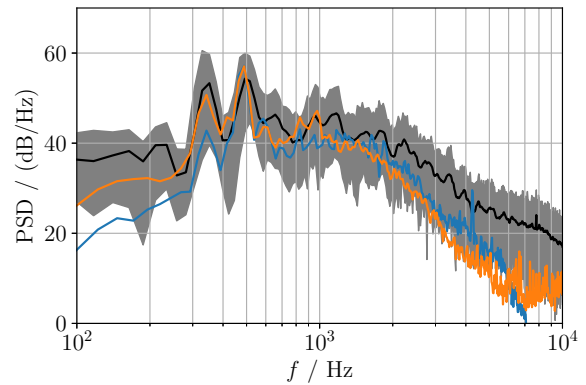(b) Microphone position 2

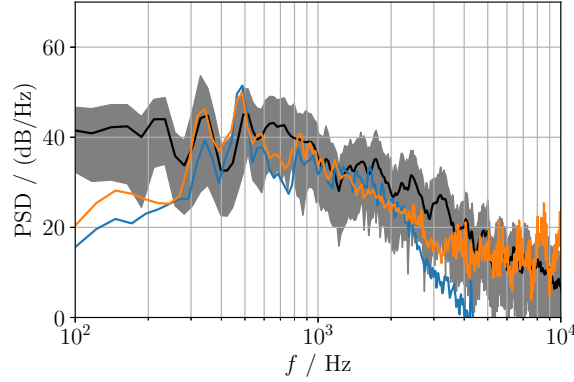(c) Microphone position 3

(d) Microphone position 4

(e) Microphone position 5

(f) Microphone position 6

(g) Microphone position 7

Figure 5.3.: Results of the aeroacoustic simulations at the different microphone positions, with the PCWE result in blue and the FWH result in orange.

5.4. Influence of interpolation

The source term computation and interpolation can be done in arbitrary order, as described in section 4.3.2. To do the interpolation first can be computationally more efficient at the cost of reduced accuracy. In this work the computation of the source terms was done before the interpolation, to investigate different interpolation procedures. All interpolation were performed on one node of the VSC with 16 CPUs. The application of CFS++ is restricted to single nodes, since it uses shared memory parallelization. For the interpolation the cut-volume cell and cell centroid interpolation algorithms were available as described in section 4.3.3. In this investigation, the acoustic sources were interpolated from the CFD mesh on the coarse acoustic mesh. The cell centroid interpolation is restricted to interpolations where the target mesh is coarser than the source mesh. The ratio of the cell size from the CFD with a base mesh size of $h_{\mathrm{CFD}} = 2\,\mathrm{mm}$ to the CAA with a cell size of $h_{\mathrm{CAA}} = 34\,\mathrm{mm}$ is

$$\frac{h_{\mathrm{CAA}}}{h_{\mathrm{CFD}}} = 17.0\,, \tag{5.1}$$

and even for the coarser mesh region of the CFD simulation, like the wake, the relation is

$$\frac{h_{\mathrm{CAA}}}{4h_{\mathrm{CFD}}} = 4.25\,, \tag{5.2}$$

which justifies the application of the cell centroid interpolation. Just outside of this finer mesh regions, where the CFD cell size increases towards the inlet and outlet, this ratio is not fulfilled anymore. But there are very little to none contribution to the acoustic sources anymore. The cut-volume cell interpolation has no restriction in the relation of interpolation cell sizes, and therefore is robust in the application. The difference in the interpolation results of the two algorithms is shown in Fig. 5.4 for the same time step in the fan plane, normalized with the maximum value of the interpolation result. The most deviations occur at the outer radius

of the duct. The difference is about $\pm 0.3\%$ of the amplitude of the source terms. Therefore the different interpolation algorithms have no visible effect on the PSD of the propagation simulation. Although the both interpolation algorithms lead to almost identical results, they
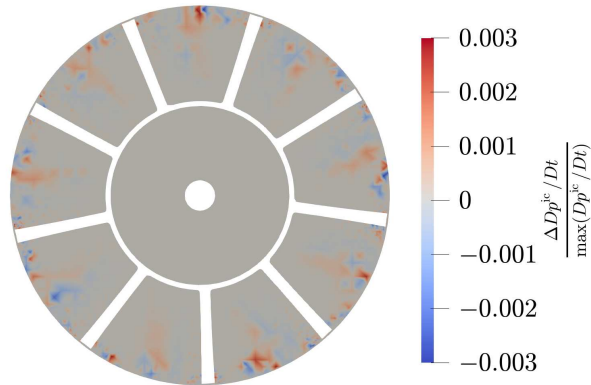

Figure 5.4.: Difference in the interpolation result for the cut-volume cell and the cell centroid interpolation algorithms normalized with the maximum value of the substantial derivative.

differ in the computational effort. For the cut-volume cell algorithm an intersection of both meshes has to be done, which can take a significant amount of time for large meshes. After the intersection, the interpolation is performed equally for both algorithms and therefore they have the same computational effort. The additional time for the mesh intersection was in this case 12 min. For short simulations, this can be the main contribution. But in this case with 20000 interpolation steps and a total wall time of 56.6 h, the nonrecurring intersection accounts for 0.35% of the total wall time. Due to the negligible increase of interpolation time and the increased robustness, the cut-volume cell interpolation was used for all other investigation in this work.

The interpolation time is mainly dependent on the mesh size of the finer mesh. In this work this is clearly the CFD mesh, which contains 23 times more elements than the coarse, about 14 times more than the middle and still 6 times more than the fine acoustic mesh. The computation of the 20000 time steps of the acoustic sources was done on the CFD mesh. After the source computation, the data was stored in a compressed HDF5 data format, which had a total size of 4.4 TB, which is 13.7% of the original exported data from the CFD simulation. The source computation exceeded the time for the interpolation by far. This is because on the one hand the interpolation is numerically easier than the computation of the derivatives. On the other hand, for the interpolation the necessary file input/output is reduced due to the reduced data. The stored sources were then interpolated on the different meshes. The statistics for the source term computation and interpolation on the different acoustic meshes is shown in Tab. 5.3. The interpolation on the acoustic meshes with a smaller number of elements, brings a further, significant reduction of the data. From the coarse to the fine mesh the reduced data size is between 1.6% to 9.1% of the original sources.

Table 5.3.: Source term interpolation statistics.

Source computation on CFD mesh	
Wall clock time	357.2 h
Core hours	5715.7 h
Source data	4.4 TB
Interpolation on coarse mesh	
Wall clock time	56.6 h
Core hours	904.0 h
Interpolated data	74 GB
Interpolation on middle mesh	
Wall clock time	62.4 h
Core hours	997.6 h
Interpolated data	143 GB
Interpolation on fine mesh	
Wall clock time	85.2 h
Core hours	1363.7 h
Interpolated data	409 GB

5.5. Influence of simulation time

For the acoustic propagation simulations special compute nodes with an extended RAM of 128 GB, but the same CPUs were used on the VSC3. The additional memory is needed to solve the large system matrices of the CAA equation system.

The simulation duration determines the obtained signal length and therefore influences the resolution in the frequency domain. Besides that, transient effect of the underlying CFD simulation can influence the result at a specific simulation time. For (cyclo-) stationary simulations like the flow field of the fan, the transient effects should not influence the spectral result from one revolution to another. But since all simulations start from certain initial conditions, transient effects occur if the stationary state is not fully reached. For the mean quantities of a CFD simulation it is straight forward to determine if they reached a steady state, but not for the fluctuating quantities that result in the acoustic sources later on. For the CFD simulations it was sufficient to simulate 2.5 revolution of the fan (respectively 10 k time steps) to obtain such a steady state. After that, the export of flow quantities and the acoustic propagation simulation was started. To investigate the convergence to a steady state in the acoustic simulation, the acoustic behavior was investigated over the simulation time. For that reason, the total simulation time was divided in batches of 1.24 revolutions (respectively 5 k steps or 0.05 s) and from the acoustic result of each of this batches, the PSD of the PCWE simulation and FWH analogy was computed. The PSD of the first four batches is shown in different colors in Fig. 5.5. Except for the frequency resolution, the display of the measurement results is the same as before. This investigation was done at microphone position 4 and for the PCWE simulation the coarse acoustic mesh was used. Since the simulation time of each batch is very

(a) Result of the PCWE simulation

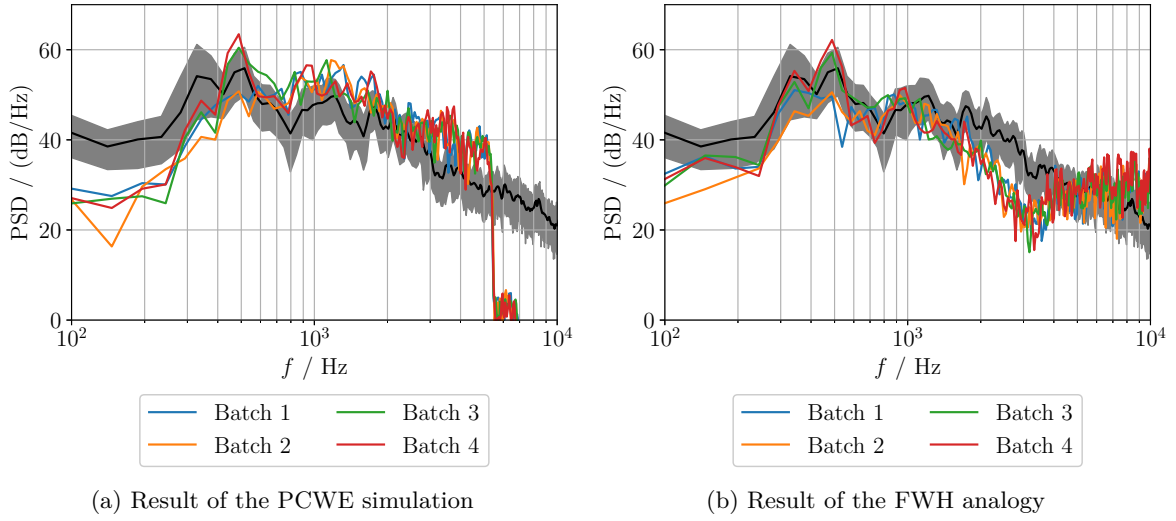(b) Result of the FWH analogy

Figure 5.5.: Acoustic result of the first four batches from the simulation compared to the measurement at microphone position 4.

short, a frequency resolution of $\Delta f = 32\,\mathrm{Hz}$ has been used in the evaluation. All batches of the PCWE simulation underestimate the measured PSD below $400\,\mathrm{Hz}$ and overestimate it slightly above $600\,\mathrm{Hz}$. For the first two batches, the subharmonic peaks can not be identified. In batch 3 and 4, the subharmonic peaks are forming, although the first subharmonic peak is underestimated and the second one is overestimated. The results of the FWH analogy have higher amplitudes at the low frequencies, but distinct subharmonic peaks also occur just for batch 3 and 4. Hence, it can be assumed that the simulation reaches a steady state in the acoustic sense, after this 2.5 revolutions of export time or a total of 5 revolutions of the fan (respectively $20\,\mathrm{k}$ iterations or $0.2\,\mathrm{s}$). Therefore, the results are evaluated from revolution 5 on. Since the subharmonic peaks result in the interaction of the tip flow and the following blades, it can be assumed, that this interaction takes longer to fully develop in the CFD simulation than the other flow phenomena. The frequencies above $600\,\mathrm{Hz}$ do not seem to have a trend over the simulation time. Above $1\,\mathrm{kHz}$ the measurement signal decays by $30\,\mathrm{dB/decade}$ which is $9\,\mathrm{dB/octave}$[1].

The second four batches are shown in Fig. 5.6. The acoustic result of these four batches show no trend over the simulation time. Surprisingly the first subharmonic peak decreased for both prediction methods. For the PCWE simulation the peak is not visible anymore and the low frequencies stay at a similar amplitude as in the first four batches. The FWH analogy has still higher amplitudes in the low frequency range and the peak is just visible in batch 5 and 8. Since the prediction of the PCWE simulation and the FWH analogy show similar behavior of the first subharmonic peak, it can be assumed that this is a phenomenon occurring in the

---

[1]For an impulse excitation it can be shown that a rectangular impulse function leads to an amplitude spectrum with a decay of $6\,\mathrm{dB/octave}$ and a triangular excitation with the same total impulse leads to an amplitude spectrum with a decay of $12\,\mathrm{dB/octave}$.

(a) Result of the PCWE simulation
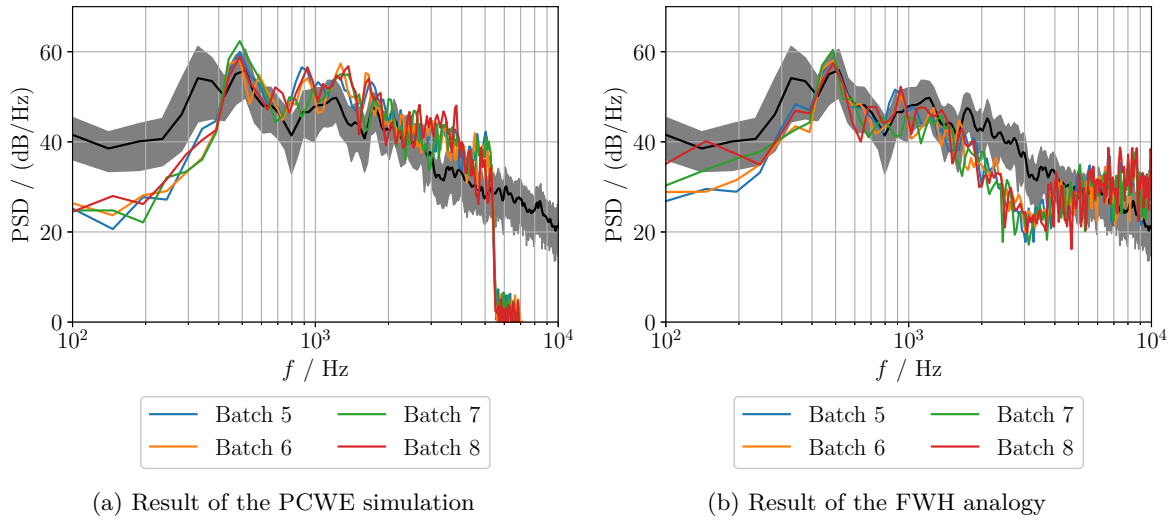
(b) Result of the FWH analogy

Figure 5.6.: Acoustic result of the second four batches from the simulation compared to the measurement at microphone position 4.

underlying CFD data. Whether this phenomenon is physical or not can not be judged. A further investigation of the source behavior over the simulation time is done in section 5.8. The better prediction of the first subharmonic peak of the FWH method results in the over all higher amplitudes of this prediction method in the low frequency range.

5.6. Influence of blending

The blending, as described in section 4.3.6, is supposed to improve the result of the acoustic simulation. The results of the different spatial blending functions is shown in Fig. 5.7 for microphone position 4. The yellow curve shows the result with no spatial blending. Compared to the measurements, the second subharmonic peak and higher frequencies are overestimated. The blue curve shows the result with the first spatial blending, where the sources were blended directly before the interfaces. It reduces the PSD between two and three dB in a broad frequency range between 100 Hz and 1.5 kHz. This means, that the blended sources are radiating in a very broad frequency range. Such broadband noise sources might occur in turbulent jets, but it is more likely that it results from numeric noise. Although the reduction is not reasonable below 400 Hz, where the PSD is already underestimated, the overall result improves. In the high frequency range, between three and four kHz, the PSD is increased by the blending, where in the simulation without blending a dent occurs in the signal. This is supposed to result from the interaction of the blending function with the actual sources in the blending region. The green curve shows the result of the second spatial blending. It leads to an increase of about 10 dB up to 500 Hz and of about 5 dB between 500 Hz and 1 kHz. In the higher frequency range, it comes to varying reduction of the amplitude. Although the first subharmonic peak is met better with the increased PSD, the increase due to the blending is not physical. The
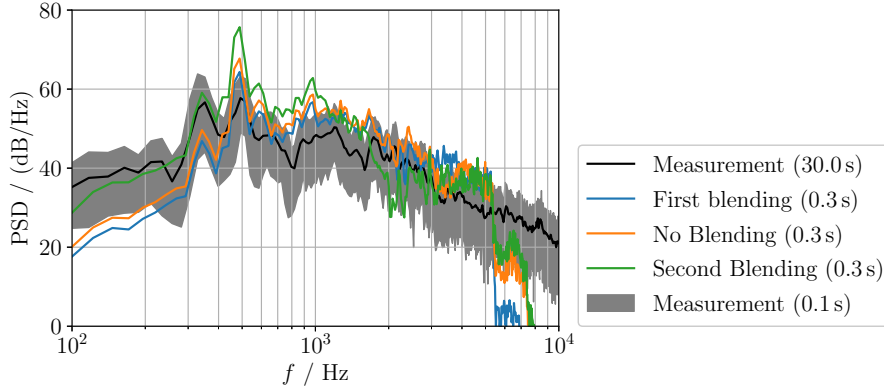
Figure 5.7.: Influence of different blending functions on the acoustic result at microphone position 4.

increase is supposed to result from the interaction of the blending function with (unphysical) noise sources. Due to the suppression of unphysical noise sources the first spatial blending was used in all simulations except this investigation.

The blending in time is supposed to omit unphysical artifacts at the beginning of the simulation. In Fig. 5.8, the time signal of the acoustic pressure at microphone position 4 is shown at the beginning of the simulation. The blue curve shows the acoustic pressure from a simulation with time blending and the orange curve shows the acoustic pressure from a simulation without time blending. For the simulation without blending, the first signal arrives at $t = 0.002\,\text{s}$. This means that the acoustic signal results from a source closer than $1\,\text{m}$, which is outside the test section and the nozzle (since the microphone is located $1\,\text{m}$ in front of the nozzle), and therefore is likely to result from numerical noise at the beginning of the simulation. After the first arriving signal, huge acoustic pulses are recorded in the time between $0.002 < t < 0.004$. They result from the initial jump of the sources in the source region around the fan. Afterwards, the acoustic pressure starts to decrease as the initial pulses leave the simulation domain through the PML and just secondary pulses from reflection at the geometry are detected. For the blended simulation, the first signal arrives at $t = 0.0028\,\text{s}$ and increases slowly. The acoustic amplitude is overshooting the rest of the signal at $t = 0.004\,\text{s}$ slightly, but normalizes very quickly afterwards. The difference between both simulation is shown in Fig. 5.9, again for microphone position 4. It can be seen, that the largest differences are vanished at a time of $t = 0.01\,\text{s}$, but the error decreases asymptotically and persists for a longer time period. The huge pulses at the beginning of the simulation could be cropped in the signal. For the used setup, the short time at the beginning plays a minor role for the PSD of the complete simulation. But as the simulation time is costly (and mostly too short anyways), this is not wanted. Furthermore, no clear time can be defined after which the signal can be considered physical since this depends on the reflections of the geometry. For example in pipe systems, the reflections of the initial pulses can persist very long. Although the blending function alters the acoustic field at the beginning of the simulation, it reduces unphysical effects, and is therefore very useful to improve the results. All simulation results except for this investigation were
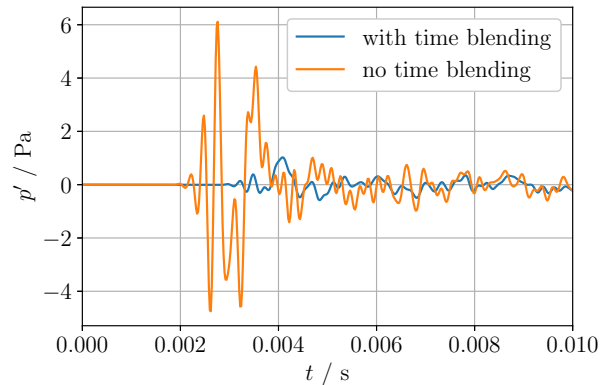
Figure 5.8.: Acoustic pressure at the beginning of the simulation at microphone position 4.

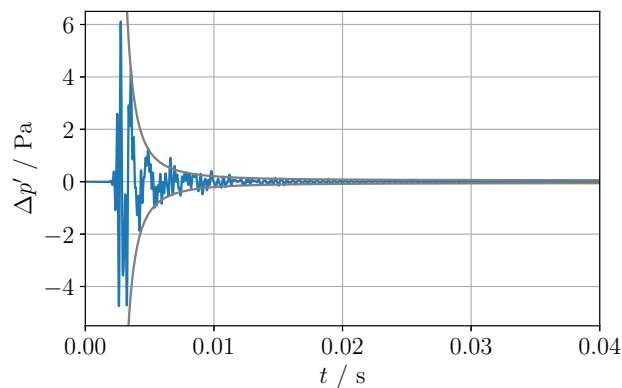obtained using this temporal blending function.

Figure 5.9.: Decaying difference between the simulation with and without blending at microphone position 4.

5.7. Influence of mesh discretization

The mesh discretization has influence on the spatial resolution of the simulation, the acoustic result and the computational effort. In the acoustic propagation simulation, different acoustic mesh discretizations have been investigated as described in section 4.3.5. The acoustic result from the different meshes at microphone position 4 is shown in Fig. 5.10. Over all the different acoustic meshes lead to very similar results. The similar results in the frequency range below 1 kHz are expected, since all meshes were designed to resolve this range well. It also means, that the mesh in the source region is fine enough to resolve the spatial characteristics of the sources. In the high frequency range between 2 and 5 kHz, small deviations occur in the acoustic results where the results of the fine mesh are slightly closer to the measurement. In the frequency
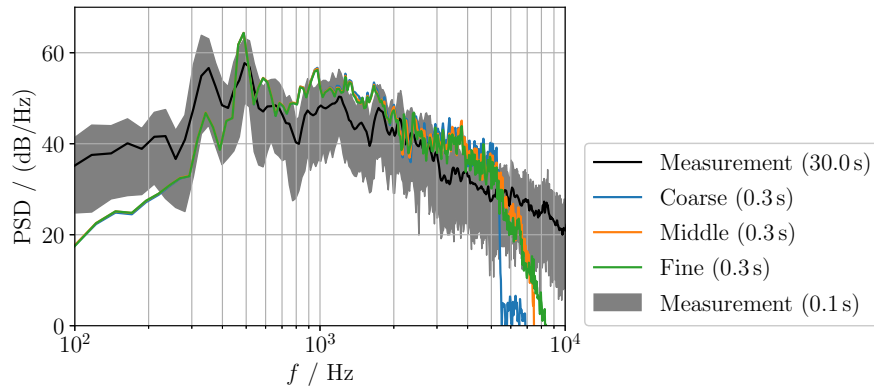
Figure 5.10.: Influence of the mesh discretization on the acoustic result at microphone position 4.

range above 5 kHz the simulation on the coarse mesh is stronger influenced by the filtering of the α-method than the simulations on the finer meshes.

From a design point of view, only the fine mesh is capable to resolve the acoustic propagation in the high frequency range accurately. Insight brings an investigation of the acoustic propagation in the pseudo 1-D duct used in section 3.2.3. On this mesh the acoustic propagation was used with elements of different cell sizes. The comparison of the fine and coarse mesh are shown on Fig. 5.11. The curve of the fine discretization with hexahedral elements is shown
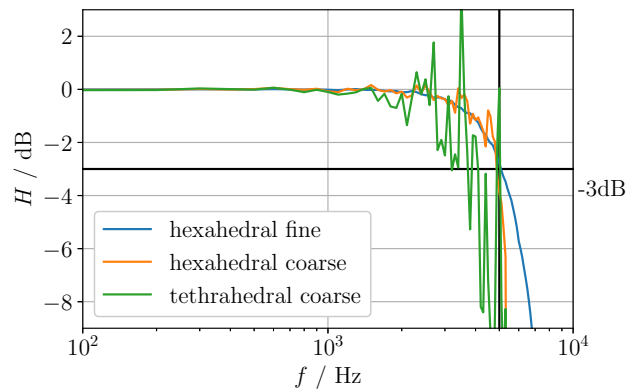

Figure 5.11.: Transfer function H for different discretizations in the pseudo 1-D duct.

in blue. The yellow line describes the coarse discretization with hexahedral elements. It can be seen, that the differences occur as expected above 1 kHz but are in the range of ± 1 dB up to the corner frequency of 5 kHz. This surprisingly good agreement results from the plane propagation through the hexahedral elements. The green curve shows the result from a discretization with tethrahedral elements of the same edge length as the coarse hexahedrals. The differences to the fine discretization rise rapidly above 1 kHz. In the fully 3-D propagation of

the fan simulation, it can be expected that the hexahedral elements do not perform as good as in the pseudo 1-D case. Nevertheless, the good agreement of the simulations with fine, middle and coarse mesh are expected to result from the usage of hexahedral elements with very low skewness which was obtained by the block structured mesh in the propagation region.

The statistics for the acoustic propagation simulations with different mesh sizes are shown in Tab. 5.4. The propagation simulations were again performed on single nodes of the VSC3

Table 5.4.: CAA simulation statistics.

CAA simulation	
CPUs	16
Exported time steps	20000
Time step size	20 µs
coarse mesh (1.0 M elements)	
Wall clock time for simulation	68.7 h
Core hours	1099.7 h
Exported data	86 GB
middle mesh (1.7 M elements)	
Wall clock time for simulation	129.2 h
Core hours	2066.4 h
Exported data	176 GB
fine mesh (3.9 M elements)	
Wall clock time for simulation	427.7 h
Core hours	6842.7 h
Exported data	490 GB

with 16 CPUs. The computational effort in simulation time and exported data rise strongly with the total element number. For the coarse mesh, the simulation time is in the order of the interpolation time, but for larger meshes the simulation time exceedes the interpolation time and for the fine mesh the solution time is even higher than the source computation time on the CFD mesh.

5.8. Analysis of source terms

The stochastic noise prediction methods can not predict tonal noise and are therefore just of limited suitability for the prediction of fan noise. Nevertheless, they can give insight in the (at least stochastic) noise sources. The stochastic noise sources were obtained from a RANS simulation, which is computationally cheap, compared to the transient simulations. Therefore this sources could be used for a numerical optimization. The volume sources of Proudman computed with (2.26) are shown in Fig. 5.12. The iso surfaces show values of the same source level. The highest values occur in the tip gap of the blades. High values also occur behind the blade tip, where the tip flow is following the blades. It can be expected that a modification of
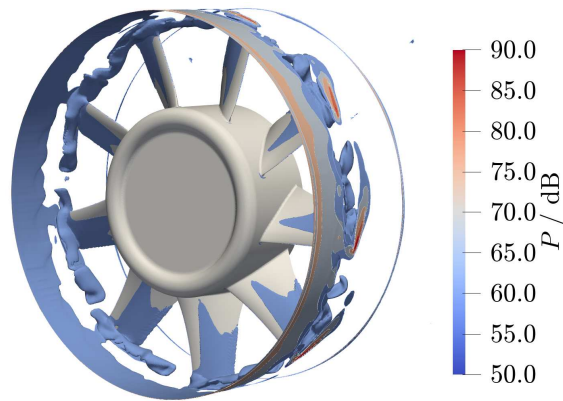
Figure 5.12.: Iso surfaces of the acoustic power contribution of Proudman in the volume.

the tip flow has a direct influence on the radiated sound of this fan. Therefore, this would be a starting point for acoustic optimizations. At the beginning of the duct, moderate noise sources occur around the whole circumference. This can result from the boundary layer entering from the nozzle, or from numerical noise due to the nonconforming interface. Further noise sources occur at the rear part of the blades, which is supposed to result from the turbulent boundary layer.

The surface sources of Curle computed with (2.25) are shown in Fig. 5.13. The highest
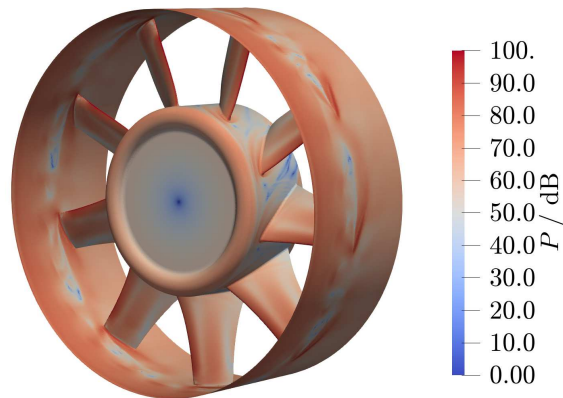

Figure 5.13.: Generated acoustic power contribution of Curle on the surface.

values of the source level on the surface occur at the leading edges of the blades and at the duct in the tip region. This sources indicate, that a modification of the leading edge of the blades can reduce the emitted sound. In fact, there are ongoing researches for modified leading edges to reduce airfoil noise and recently also for fan noise (see for example [68]).

More detailed information about the actual sound sources can be gained by the sources of the PCWE equation. For one time step iso surfaces are shown in Fig. 5.14. Large sources are at the leading edges of the blades, constantly distributed from the root to the tip. From a theoretical
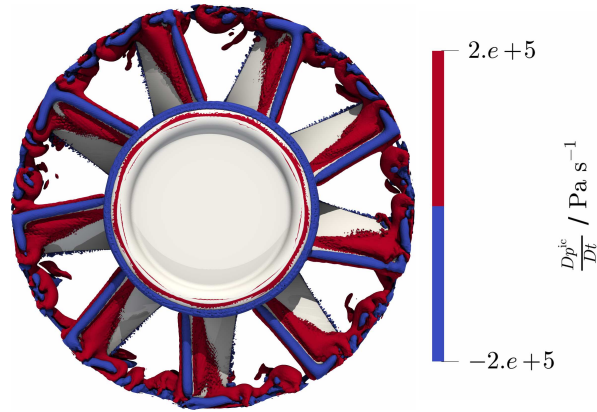
Figure 5.14.: Acoustic sources of the PCWE equation at a certain time step.

point of few, the leading edge noise sources are responsible for the tonal components at the BPF. Smaller sources are at the outer radius of the duct, covering the whole circumference. They are expected to result from turbulent flow structures of the tip flow. Very small noise sources occur at the trailing edges of the blades, which are supposed to result from vortex shedding. In addition to that, are sources at the beginning of the hub, where the question arises what the acoustic source mechanism should be at this location. To show the frequency behavior of the sources, the whole sources were transformed in the frequency domain. To perform the Fourier transformation of the rotating geometry, a moving reference frame was used. Some results for batch 1, 4 and 7 are shown in Fig. 5.15. The iso surfaces have the same values in all figures and show the real part of the acoustic source amplitude multiplied with the phase. The short simulation time restricts the frequency resolution of the Fourier transformation. Therefore, the closest frequency to the BPF of 223 Hz is 220 Hz, shown on the left side. The Fourier transformation of the sources at the first subharmonic peak are shown on the right side. The first row shows the result from the first batch, where no clear tonal components could be observed in the spectrum, the second row from the fourth batch, where distinct peaks occurred and the third row from the fourth batch, where no peak was visible anymore. At the BPF there are large sources at the leading edge for the first batch. At the outer radius, long stretched sources occur in circumferential direction. With further simulation time, these sources grow stronger, especially at the leading edge and at the outer part of the fan blades. At the seventh batch, the sources at the blade are reduced drastically and the source field is dominated by the sources at the outer radius. For the first subharmonic peak, the sources are in general weaker at the leading edge and a similar behavior with the simulation time can be seen. At the outer radius the sources are more compact, due to the higher frequency. At the hub between the blades sources can be seen, but the sources at the beginning of the hub do not occur at this frequency. The transient behavior in the source terms is mostly visible at the leading edge and can only result from the CFD data, since similar behavior occurs in the PCWE simulation and FWH analogy. Where this transient behavior comes from is not known. A simple explanation would be errors in the CFD simulation, but also a transient phenomenon in the tip flow structures could be the reason. Unfortunately it
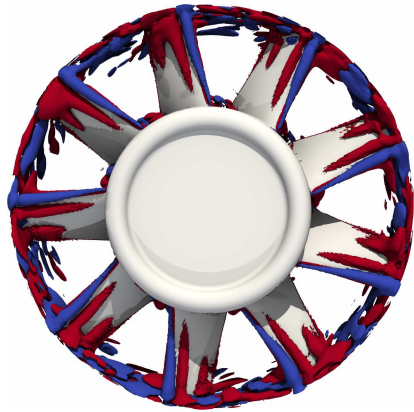
(a) Sources of the first batch at 220 Hz close to the first BPF
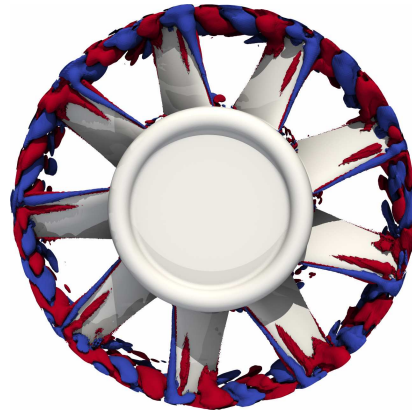
(b) Sources of the first batch at 340 Hz at the first subharmonic peak
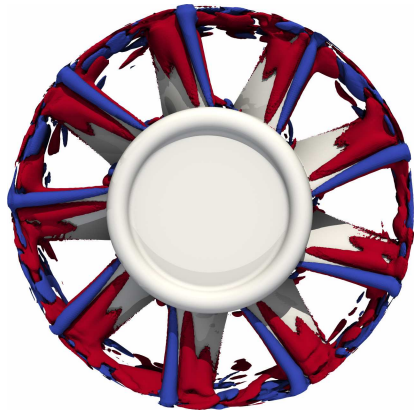
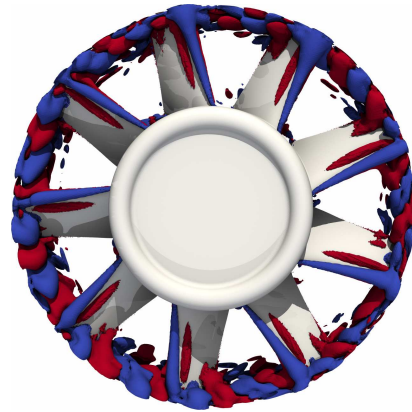(c) Sources of the fourth batch at 220 Hz close to the first BPF
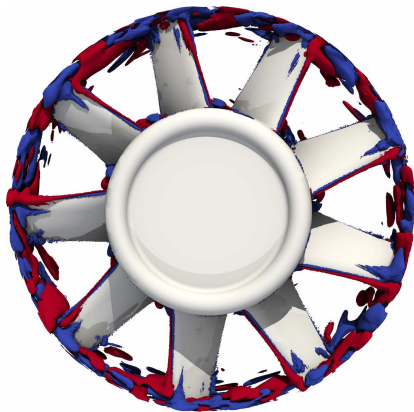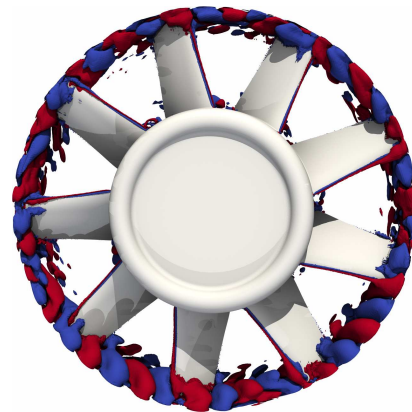
(d) Sources of the fourth batch at 340 Hz at the first subharmonic peak

(e) Sources of the seventh batch at 220 Hz close to the first BPF

(f) Sources of the seventh batch at 340 Hz at the first subharmonic peak

Figure 5.15.: Constant iso surfaces of the acoustic source term at different frequencies and different times in the simulation.

was not possible to investigate the whole flow field throughout the simulation, as the amount of data is too large.

From the CFD simulations some information can be obtained, to observe possible sound sources of the transient flow. One of the main sound sources for this fan is the interaction of the tip flow with the following blades. In Fig. 5.16, the streamlines through the tip gap of the blade pointing towards the observer are shown. It can be seen that they reach the blade tip of the following blade, where some of the streamlines are redirected downstream in the diffusor, which leads to interactions with the blade and therefore noise. Some of the streamlines pass this blade and reach even the next two following blades. For larger flow rates, the streamlines are redirected downstream and this interaction is reduced. Figure 5.17 shows iso surfaces of the
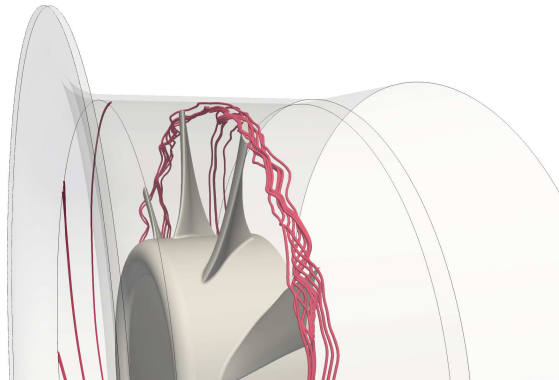

Figure 5.16.: Streamlines of the flow through the tip gap, which is interacting with the following blade.

Q-criterion colored with the flow velocity. The Q-criterion describes vortices in the flow[43], which are known to be sound sources. Large structures can be seen to origin from the blade tips. They coincide with the large acoustic sources of the PCWE equation. Furthermore, at the hub between the blades, vortices can be seen that arise from the secondary flow (see for example [108]). They can be expected to be responsible for the sources between the blades in Fig. 5.15. In addition to that, small horseshoe vortices at the roots of the blades are visible, but the Q-criterion gives no information about the noise sources at the leading edges of the blades. From the results it can be seen, that the noise prediction methods of class 1 and 2 can give basic information about the location and structure of the noise sources, although they are not suited to predict the tonal sound emission of this setup. From the CFD simulation some flow phenomena can be investigated that result in acoustic sources. But only the aeroacoustic sources of the PCWE equation give a real structure and behavior of the sources.
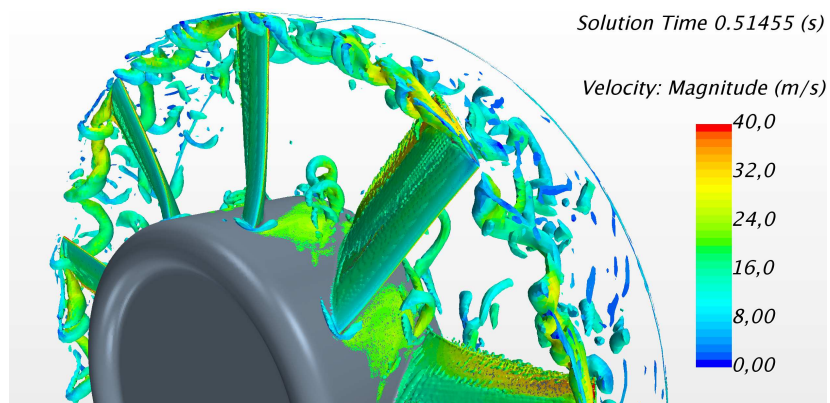
Figure 5.17.: *Q*-criterion at the certain time step, which is showing the turbulent structures of the tip flow.

Conclusion

The three aims of this work were to investigate the prerequisites for numerical aeroacoustic simulations to predict sound correctly, the comparison of different prediction methods and the investigation of noise sources on the application. For the prediction of the turbulent flow field a DES simulation with an all y^+ wall treatment, which uses Reichardt's law for a correct treatment of locally high values of y^+, was used. The used turbulence model had no visible effect on the aerodynamic results, therefore the fast Spalart-Allmaras model was used. A mesh convergence study lead to the choice of a mesh with $23.4\,\mathrm{M}$ cells. The deviation in pressure rise was $11.3\,\%$, in efficiency $3.4\,\%$ and in shaft power $7.1\,\%$. The most deviation in the velocity occurred at the pressure side of the fan. A stationary state for the flow field was reached after 2.5 revolutions of the fan. For the aeroacoustic simulations 9.9 revolutions of flow data were exported. From the results of the FWH analogy and the PCWE equation it was observed, that at least 5 revolutions of the fan had to be computed before tonal components were predicted in the spectrum. For the solution of the PCWE equation, the acoustic sources were interpolated on an acoustic mesh, with a tethrahedral mesh in the rotating domain and a hexahedral mesh in the propagation domain. For the interpolation, the cut-volume cell and the cell centroid interpolation method were compared. Both interpolation methods showed similar results with a deviation in the range of $\pm 0.3\,\%$ of the maximum value of the sources. A slow temporal blending at the beginning of the simulation was found to reduce unphysical artifacts. A spatial blending of the source terms before the nonmatching interfaces was found to improve the acoustic result, where a blending after the interfaces made the result worse. The mesh discretization of the acoustic mesh only had a small influence on the acoustic result, but the mesh size increases the computation time strongly.

The comparison of different prediction methods showed that even very rudimentary semi empirical prediction methods give results with an accuracy below $2\,\mathrm{dB}$ of the over all sound power level for the application to the used low pressure axial fan benchmark. This good agreement is just valid in the design point of the fan. For other operating points, the predictions of these methods get worse. Aeroacoustic optimization is not taken into account in this predic-

tion methods. The PCWE equation predicts the over all sound power level with a deviation of 0.6 dB. The spectral result shows that the subharmonic peaks are predicted, but the amplitudes below 500 Hz are underestimated. Compared to the FWH analogy the PCWE equation predicts higher amplitudes above 500 Hz. This is especially significant at microphone position 4 on the axis of rotation, where the acoustic directivity of the geometry leads to an amplification of the signal. To investigate the directivity of the geometry a harmonic simulation with an artificial excitation was used. The FWH analogy predicts the over all sound power level with a deviation of 2.1 dB. The prediction of the frequency range below 500 Hz is closer to the measurements compared with the PCWE equation. With used simplifications, the FWH analogy gives reasonable results to a frequency up to 2-3 kHz, but the numerical effort is smaller, since it is incorporated in the CFD solver. Both methods have the largest deviations to the measurements at microphone positions 1 and 7 which are perpendicular to the nozzle. From both prediction methods, a change in amplitude of the first subharmonic peak over time was observed. This time dependent behavior is likely to result from transient effects of the CFD simulation, but whether they are physical or numerical can not be identified.

The investigation of the predicted acoustic noise sources showed different sources, depending on the prediction method. The stochastic method of Proudman predicted the strongest sources in the volume of the tip gap, and in the wake of the tip flow. Further sources occur in the boundary layer of the blades and the duct. The stochastic method of Curle predicts the strongest sources on the surfaces of the leading edge and the tip gap of the fan blades. Streamlines of the flow field show interactions of the tip flow with the blades, which is an important noise mechanism. Furthermore, turbulent structures in the flow field occur in the outer region of the blades and at the hub between the blades, accounting for noise sources. A more direct information about the noise sources was obtained from the sources of the PCWE equation. For a transient observation, they show strong sources at the leading edges of the blades and at the outer radius in the tip flow region. In accordance to the acoustic result of the PCWE equation and the FWH analogy, the change in amplitude over time can also be observed in the sources.

Potential for improvement in this work is seen in the resolution of the CFD simulation. This might improve the prediction of the broadband noise, since the DES simulation models small vortices which are radiating at a high frequency. Further investigations could be undertaken to improve the velocity profile on the pressure and suction side of the fan. For a more profound assessment of CFD simulation, the convergence investigation should be expanded to the whole simulation workflow including the CFD simulation, computation of source terms, interpolation and acoustic propagation simulation. Only then, the convergence of acoustic result can be related to changes in the flow field. A first step would be to investigate the convergence of acoustic source quantities like the substantial derivative of the pressure directly in the flow simulation. But a valid criterion to judge the convergence of this quantity has yet to be found since it is space and time dependent. The computation of acoustic sources in the CFD simulation is also beneficial from a numerical point of view, since the CFD solver is distributed memory parallelized in contrast to the used program CFS++. With the higher parallelization a reduction of computational time could be achieved. In future works, the observed source structures could be used as a design parameter for the acoustic mesh. With a known size of the sources, the spatial resolution can be adapted not only to the acoustic wave length but also the source structure. An interesting behavior was made with the varying amplitude of the

first subharmonic peak. Here, a further investigation could bring more insight in the origin of this phenomenon.

Potential flow

The potential flow theory is used to obtain a solution for the Euler equations. Therefor it can just used for inviscid flow without flow separations. This can be applied to streamline bodies like airplanes or ships and gives information about the velocity and pressure filed. Most often it is applied for relatively incompressible flows. For design purposes this is often sufficient to obtain a fast prediction of lift and induced drag. Corrections for friction based drag can be applied later on. The Euler equation can be written as:

$$\frac{\partial \mathbf{u}}{\partial t} + \nabla \frac{\mathbf{u}^2}{2} - \mathbf{u} \times \nabla \times \mathbf{u} = -\frac{1}{\rho} \nabla p + f \tag{A.1}$$

with the velocity vector $\mathbf{u}$, density ρ, pressure p and a volume force f. For a flow without rotation:

$$\nabla \times \mathbf{u} = 0 \tag{A.2}$$

a scalar potential function can be found to describe the flow field and the flow field is called a 'potential flow field'[1]. Flow fields without rotation occur often in free flows outside of boundary layers. Alternatively the flow field can be decomposed in a rotational and a solenoidal field. Since the velocity field is rotational free, the flow field can be written as the gradient of a scalar function

$$\mathbf{u} = \nabla \Phi \,. \tag{A.3}$$

Inserting this in the conservation of mass

$$\frac{D\rho}{Dt} + \rho \nabla \cdot (\nabla \Phi) = \frac{D\rho}{Dt} + \rho \Delta \Phi = 0 \tag{A.4}$$

we obtain the potential formulation:

$$\Delta \Phi = 0 \,. \tag{A.5}$$

---

[1]For $\nabla \times \mathbf{u} \neq 0$ a vectorial potential function can be used to described the flow field and the flow field is called an 'eddy flow field'.

To obtain the pressure from the velocity field, the potential function can be inserted in the Euler equation and by neglecting the volume force term we obtain

$$\frac{\partial \Phi}{\partial t} + \frac{1}{2}(\nabla \Phi)^2 = -\frac{1}{\rho}p \,. \tag{A.6}$$

A.1. Potential Flow in 2D

In two dimensions the potential function writes as

$$\Delta \Phi = \frac{\partial^2 \Phi}{\partial x^2} + \frac{\partial^2 \Phi}{\partial y^2} = 0 \,, \tag{A.7}$$

with the velocity components:

$$u = \frac{\partial \Phi}{\partial x} \,, \tag{A.8}$$

$$v = \frac{\partial \Phi}{\partial y} \,. \tag{A.9}$$

A similar function, the stream function can be defined:

$$\Delta \Psi = \frac{\partial^2 \Psi}{\partial x^2} + \frac{\partial^2 \Psi}{\partial y^2} = 0 \tag{A.10}$$

it also fulfills the required conditions

$$\nabla \times \mathbf{u} = -\left(\frac{\partial^2 \Psi}{\partial x^2} + \frac{\partial^2 \Psi}{\partial y^2} \right) = 0 \tag{A.11}$$

and has the velocity components:

$$u = \frac{\partial \Psi}{\partial y} \,, \tag{A.12}$$

$$v = -\frac{\partial \Psi}{\partial x} \,. \tag{A.13}$$

In two dimensions the potential flow can describe in the complex plane with complex coordinates

$$z = x + iy \tag{A.14}$$

and the velocity in the complex plane

$$w = u + iv \,, \tag{A.15}$$

which simplifies the solution. The complex velocity potential writes then as

$$F(z) = F(x + iy) = \Phi + i\Psi \tag{A.16}$$

and the velocity components can be obtained by the derivative of the complex potential with respect to the complex coordinate:

$$\frac{dF}{dz} = u - iv\,. \tag{A.17}$$

Alternatively, the velocity in x and y components can be obtained by the spatial derivative of the velocity potential or the stream function:

$$u = \frac{\partial \Phi}{\partial x} = \frac{\partial \Psi}{\partial y}\,, \tag{A.18}$$

$$v = \frac{\partial \Phi}{\partial y} = -\frac{\partial \Psi}{\partial x}\,. \tag{A.19}$$

The circulation intensity computes as the line integral over the velocity

$$\Gamma = \oint_s \mathbf{u} \cdot \mathrm{d}s\,. \tag{A.20}$$

For inviscid flows yields

$$\frac{D\Gamma}{Dt} = 0 \tag{A.21}$$

which means, that the vortices do not dissipate over time.

To solve the Laplace problem, it is necessary to define all boundaries. Walls can just be described as slip walls by:

$$u_n = 0 \rightarrow \frac{\partial \Phi}{\partial n} = 0\,. \tag{A.22}$$

A far field flow can be described as:

$$\nabla \Phi = \mathbf{u}_\infty \rightarrow \Phi(x) = \mathbf{u}_\infty x + C\,. \tag{A.23}$$

The linearity of the problem makes it possible to superpose the solution. Furthermore, it should be mentioned, that the solution is just unique for convex domains.

A.2. Description of one vortex

In the complex potential a vortex can be described as

$$F(z) = -i\frac{\Gamma}{2\pi}\ln(z) = -\frac{\Gamma}{2\pi}(i\ln(r - \varphi)) = \frac{\Gamma}{2\pi i}\ln[(x - x_0) + i(y - y_0)] \tag{A.24}$$

with $\Box_0$ being the location of the vortex core. The resulting velocity potential is

$$\Phi = \frac{\Gamma}{2\pi}\arctan(\frac{y}{x}) = \frac{\Gamma}{2\pi}\varphi \tag{A.25}$$

and stream function

$$\Psi = -\frac{\Gamma}{2\pi}\ln(\sqrt{x^2 + y^2}) = -\frac{\Gamma}{2\pi}\ln(r) \tag{A.26}$$

which leads to the velocity components

$$u = -\frac{\Gamma}{2\pi}\frac{y}{x^2+y^2} = -\frac{\Gamma}{2\pi}\frac{\sin\varphi}{r}\,, \qquad (A.27)$$

$$v = \frac{\Gamma}{2\pi}\frac{x}{x^2+y^2} = \frac{\Gamma}{2\pi}\frac{\cos\varphi}{r}\,. \qquad (A.28)$$

In cylindrical coordinates the vortex can be described simply by the radius r and the angle θ

$$z = x + iy = re^{i\theta}\,, \qquad (A.29)$$

where the velocity in circumferential and radial direction are

$$u_\theta = \frac{\Gamma}{2\pi}\frac{1}{\sqrt{x^2+y^2}} = \frac{\Gamma}{2\pi}\frac{1}{r}\,, \qquad (A.30)$$

$$u_r = 0\,. \qquad (A.31)$$

A.3. Desingularization of the vortexcore

The velocity of potential vortex goes to infinity in the vortex center. This leads to numerical problems in the simulation. Therefore many models for a more physical vortex core exist. A comparison of different models is given in [13]. The easiest is the Rankine vortex model [92]. It assumes a linear velocity profile in the vortex core, comparable to a solid body rotation.

A more sophisticated model is the "Scully model" or so called Kaufmann vortex [100],[64]. It has the form:

$$u_\varphi = \frac{\Gamma}{2\pi}\frac{r}{r_c^2+r^2} \qquad (A.32)$$

with a desingularization factor r_c equivalent to the vortex core. In the inner core ($r_c \gg r$) this leads to a linear behavior ($u_\varphi \propto r$)like the Rankine vortex and for further distances from the vortex core ($r_c \ll r$) the velocity tends to the original solution ($u_\varphi \propto 1/r$). In Fig. A.1 the velocity of the vortex core is displayed over the vortex radius. In black is the original solution of the potential theory. Towards smaller radii the velocity increases hyperbolically. For an approximated vortex radius of $r_c = 1$ the velocities for the Rankine vortex (dotted) and the Sully vortex (dashed) are displayed. The velocity of the Rankine vortex shows the linear behavior of a solid rotating body. The velocity of the Sully vortex increases first liner and falls then to the original solution.

A similar model as the Scully vortex was provided by Vatistas [115] but he used higher exponents n:

$$u_\varphi = \frac{\Gamma}{2\pi}\frac{r}{(r_c^{2n}+r^{2n})^{1/n}}\,. \qquad (A.33)$$

There are other vortex model like the Hamle-Oseen vortex model or the Lamb-Oseen vortex model that take viscosity into account, but they time dependent, and therefore not suitable for a constantly rotating vortex pair configuration.
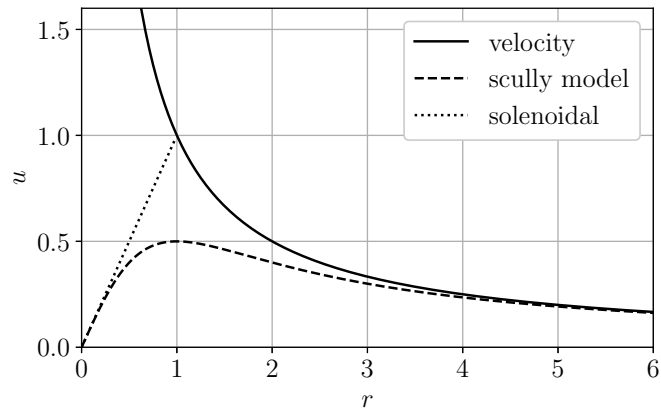
Figure A.1.: Velocity distribution over the radius.

Bibliography

[1] Bundesgesetz über Sicherheit und Gesundheitsschutz bei der Arbeit (ArbeitnehmerInnenschutzgesetz – ASchG), 1995.

[2] Akustik - Bestimmung der Schallleistungs- und Schallenergiepegel von Geräuschquellen aus Schalldruckmessungen - Hüllflächenverfahren der Genauigkeitsklasse 2 für ein im Wesentlichen freies Schallfeld über einer reflektierenden Ebene. DIN EN ISO 3744:2010, 2010.

[3] Noise generation and noise reduction in air-conditioning systems. VDI 2081, 2001.

[4] Emissionskennwerte technischer Schallquellen – Ventilatoren. VDI 3731 Blatt 2, 1990.

[5] Verordnung über den Schutz der Arbeitnehmer/innen vor der Gefährdung durch Lärm und Vibrationen (Verordnung Lärm und Vibrationen – VOLV), 2006.

[6] M. Ainsworth. Discrete dispersion relation for hp-version finite element approximation at high wave number. *SIAM J. Numer. Anal.*, 42(2):553–575, 2004. ISSN 0036-1429. doi: http://dx.doi.org/10.1137/S0036142903423460.

[7] R. Amiet. Noise due to turbulent flow past a trailing edge. *Journal of Sound and Vibration*, 47(3):387–393, Aug. 1976. doi: 10.1016/0022-460x(76)90948-2.

[8] R. Amiet. Effect of the incident surface pressure field on noise due to turbulent flow past a trailing edge. *Journal of Sound and Vibration*, 57(2):305–306, Mar. 1978. doi: 10.1016/0022-460x(78)90588-6.

[9] N. Andersson, L.-E. Eriksson, and L. Davidson. Large-Eddy Simulation of Subsonic Turbulent Jets and Their Radiated Sound. *AIAA Journal*, 43(9):1899–1912, Sept. 2005. doi: 10.2514/1.13278.

[10] H. Arbey and J. Bataille. Noise generated by airfoil profiles placed in a uniform laminar flow. *Journal of Fluid Mechanics*, 134(-1):33, Sept. 1983. doi: 10.1017/s0022112083003201.

[11] C. Bailly, P. Lafon, and S. Candel. Computation of noise generation and propagation for free and confined turbulent flows. In *Aeroacoustics Conference.* American Institute of Aeronautics and Astronautics, May 1996. doi: 10.2514/6.1996-1732.

[12] J. A. Benek, J. L. Steger, F. C. Dougherty, and P. G. Buning. Chimera: A Grid-Embedding Technique. Technical report, ARNOLD ENGINEERING DEVELOPMENT CENTER ARNOLD AFB TN, 1986.

[13] M. J. Bhagwat and J. G. Leishman. Generalized viscous vortex model for application to free-vortex wake and aeroacoustic calculations. *Annual forum proceedings-American helicopter society*, 58(2):2042–2057, 2002.

[14] C. Bogey, C. Bailly, and D. Juvé. Numerical Simulation of Sound Generated by Vortex Pairing in a Mixing Layer. *AIAA Journal*, 38(12):2210–2218, Dec. 2000. doi: 10.2514/2.906.

[15] L. Bommes. Spezifische Schallkenngrößen von Radialventilatoren. Technical Report 5, HLH, 1989.

[16] K. S. Brentner and F. Farassat. Analytical Comparison of the Acoustic Analogy and Kirchhoff Formulation for Moving Surfaces. *AIAA Journal*, 36(8):1379–1386, Aug. 1998. doi: 10.2514/2.558.

[17] M. Breuer. *Direkte Numerische Simulation und Large-Eddy Simulation turbulenter Strömungen auf Hochleistungsrechnern.* SHAKER VERLAG, 2002. ISBN 3-8265-9958-6.

[18] T. Brooks, D. Pope, and Marcolini. Airfoil self-noise and prediction. *NASA Reference Publication 1218*, 1989.

[19] Bundesministerium für Umwelt, Naturschutz und Reaktorsicherheit. Sechste Allgemeine Verwaltungsvorschrift zum Bundes-Immissionsschutzgesetz (Technische Anleitung zum Schutz gegen Lärm – TA Lärm), 1998.

[20] T. Carolus. *Ventilatoren.* Vieweg+Teubner Verlag, Springer Fachmedien Wiesbaden, 2013.

[21] T. Carolus. Noise Proves Nothing - Sources of Fan Noise and Their Prediction (Keynote lecture). In *Fan2012*, Senlis, France, 2012.

[22] I. B. Celik, Z. N. Cehreli, and I. Yavuz. Index of Resolution Quality for Large Eddy Simulations. *Journal of Fluids Engineering*, 127(5):949, 2005. doi: 10.1115/1.1990201.

[23] J. Christophe, J. Anthoine, and S. Moreau. Trailing Edge Noise of a Controlled-Diffusion Airfoil at Moderate and High Angle of Attack. In *15th AIAA/CEAS Aeroacoustics Conference (30th AIAA Aeroacoustics Conference).* American Institute of Aeronautics and Astronautics, May 2009. doi: 10.2514/6.2009-3196.

[24] N. Curle. The Influence of Solid Boundaries upon Aerodynamic Sound. *Proceedings of the Royal Society A: Mathematical, Physical and Engineering Sciences*, 231(1187):505–514, Sept. 1955. doi: 10.1098/rspa.1955.0191.

[25] J. Donea and A. Huerta. *Finite element methods for flow problems.* Wiley, 2003.

[26] F. Durst. *Grundlagen der Strömungsmechanik.* Springer, 2006.

[27] B. Eck. *Ventilatoren.* Springer-Verlag, Berlin-Heidelberg, 1991.

[28] K. Ehrenfried. *Strömungsakustik: Skript zur Vorlesung.* Mensch-und-Buch-Verl., Berlin, 2004. ISBN 3898206998.

[29] E. K. Enda Murphy. *Environmental Noise Pollution: Noise Mapping, Public Health, and Policy.* ELSEVIER, 2014. ISBN 0124115950.

[30] M. Escobar. *Finite Element Simulation of Flow-Induced Noise using Lighthill's Acoustic Analogy.* PhD thesis, University of Erlangen-Nuremberg, 2007.

[31] European Acoustics Association. Benchmark Cases for Computational Acoustics.

[32] R. Ewert. RPM - the fast Random Particle-Mesh method to realize unsteady turbulent sound sources and velocity fields for CAA applications. In *13th AIAA/CEAS Aeroacoustics Conference (28th AIAA Aeroacoustics Conference).* American Institute of Aeronautics and Astronautics, May 2007. doi: 10.2514/6.2007-3506.

[33] R. Ewert and R. Emunds. CAA Slat Noise Studies Applying Stochastic Sound Sources Based On Solenoidal Digital Filters. In *11th AIAA/CEAS Aeroacoustics Conference.* American Institute of Aeronautics and Astronautics, May 2005. doi: 10.2514/6.2005-2862.

[34] R. Ewert and W. Schröder. Acoustic perturbation equations based on flow decomposition via source filtering. *Journal of Computational Physics*, 188:365–398, 2003.

[35] F. Farassat. Derivation of Formulations 1 and 1A of Farassat. Technical Report NASA/TM-2007-214853, L-19318, NASA Langley Research Center, Hampton, VA, United States, Mar. 2007.

[36] P. Farrell and J. Maddison. Conservative interpolation between volume meshes by local Galerkin projection. *Computer Methods in Applied Mechanics and Engineering*, 200(1-4): 89–100, Jan. 2011. doi: 10.1016/j.cma.2010.07.015.

[37] J. H. Ferziger and M. Peric. *Computational Methods for Fluid Dynamics.* Springer, 2001. ISBN 3540420746.

[38] B. Francois, M. Costes, and G. Dufour. Comparison of Chimera and Sliding Mesh Techniques for Unsteady Simulations of Counter Rotating Open-Rotors. In *Proceeding in 20th ISABE Conference*, 2011.

[39] H. M. Frank and C.-D. Munz. Direct aeroacoustic simulation of acoustic feedback phenomena on a side-view mirror. *Journal of Sound and Vibration*, 371:132–149, June 2016. doi: 10.1016/j.jsv.2016.02.014.

[40] L. Gutin. Über das Schallfeld einer rotierenden Luftschraube. *Physical magazine of the Soviet Union*, 9(1):57–71, 1936.

[41] L. Gutin. On the Sound Field of a Rotating Propeller. Technical Report NACA-TM-1195, National Advisory Committee for Aeronautics, Langley Aeronautical Lab., Langley Field, VA, United States, Oct. 1948.

[42] C. Haigermoser. Application of an acoustic analogy to PIV data from rectangular cavity flows. *Experiments in Fluids*, 47(1):145–157, Mar. 2009. doi: 10.1007/s00348-009-0642-5.

[43] G. Haller. An objective definition of a vortex. *Journal of Fluid Mechanics*, 525:1–26, Feb. 2005. doi: 10.1017/s0022112004002526.

[44] A. Hansbo, P. Hansbo, and M. G. Larson. A finite element method on composite grids based on nitsche's method. *ESAIM: Mathematical Modelling and Numerical Analysis*, 37(3):495–514, May 2003. doi: 10.1051/m2an:2003039.

[45] J. Hardin and D. Pope. An acoustic/viscous splitting technique for computational aeroacoustics. *Theoretical and Computational Fluid Dynamics*, 6:323–340, 1994.

[46] M. Heckl and H. A. Müller. *Taschenbuch Der Technischen Akustik (German Edition)*. Springer, 1995. ISBN 3540544739.

[47] S. Heo, C. Cheong, and T. Kim. Unsteady Fast Random Particle Mesh method for efficient prediction of tonal and broadband noises of a centrifugal fan unit. *AIP Advances*, 5(9):097133, Sept. 2015. doi: 10.1063/1.4930979.

[48] M. Hornikx, M. Kaltenbacher, and S. Marburg. A Platform for Benchmark Cases in Computational Acoustics. *Acta Acustica united with Acustica*, 101(4):811–820, July 2015. doi: 10.3813/aaa.918875.

[49] T. J. Hughes. *The Finite Element Method*. Dover, Mineola, N.Y., 1. edition, 2000.

[50] A. Hüppe and M. Kaltenbacher. Investigation of interpolation strategies for hybrid schemes in computational aeroacoustics. In *41. Jahrestagung für Akustik*, pages 872–875, 2015. eingeladen; Vortrag: DAGA 2015, Nürnberg; 2015-03-16 – 2015-03-19.

[51] A. Hüppe and M. Kaltenbacher. A perfectly matched layer for the conservation equations of acoustics in the time domain. *Journal of Computational Acoustics*, 22(1), February 2012. in Publication.

[52] A. Hüppe, J. Grabinger, M. Kaltenbacher, A. Reppenhagen, and W. Kühnel. A non-conforming finite element method for computational aeroacoustics in rotating systems. In *American Institute of Aeronautics and Astronautics Conference 2014*, 2014.

[53] A. Hüppe, M.Kaltenbacher, A. Reppenhagen, F.Zenger, S. Becker, and K.Habr. Computational aeroacoustics for ducted fans. page 6, July 2015.

[54] International Organization for Standardization. ISO 5801:2007 Fans — Performance testing using standardized airways, 2007.

[55] M. P. Joel H. Ferziger. *Numerische Strömungsmechanik*. Springer Berlin Heidelberg, 2008.

[56] C. Junger and M. Kaltenbacher. Main Challenges in the Application of Hybrid Aeroacoustic Methods to Rotating Systems. In *43. Deutsche Jahrestagung für Akustik*, 2017.

[57] C. Junger and M. Kaltenbacher. Investigation of different fan noise prediction methods. In *FAN 2018 Proceedings*, 2018.

[58] C. Junger, F. Zenger, A. Reppenhagen, M. Kaltenbacher, and S. Becker. Numerical simulation of a benchmark case for aerodynamics and aeroacoustics of a low pressure axial fan. In *INTER-NOISE 2016*, pages 741–747, 2016. Vortrag: Inter-Noise 2016, Hamburg; 21.08.2016 - 24.08.2016;.

[59] B. Kaltenbacher, M. Kaltenbacher, and I. Sim. A modified and stable version of a perfectly matched layer technique for the 3-d second order wave equation in time domain with an application to aeroacoustics. *Journal of Computational Physics*, 235(0):407 – 422, 2013. ISSN 0021-9991. doi: http://dx.doi.org/10.1016/j.jcp.2012.10.016.

[60] M. Kaltenbacher. *Numerical Simulation of Mechatronic Sensors and Actuators*. Springer-Verlag Berlin Heidelberg, 3 edition, 2015. ISBN 978-3-642-40170-1. doi: 10.1007/978-3-642-40170-1.

[61] M. Kaltenbacher and A. Hüppe. Comparison of aeroacoustic source term formulations. In *DAGA 2014, Oldenburg*, 2014.

[62] M. Kaltenbacher, A. Hüppe, A. Reppenhagen, F. Zenger, and S. Becker. Computational aeroacoustics for rotating systems. In *22nd AIAA/CEAS Aeroacoustics Conference*, Lyon, France, 2016.

[63] M. Kaltenbacher, A. Hueppe, A. Reppenhagen, F. Zenger, and S. Becker. Computation aeroacoustics for rotating systems with application to an axial fan. *AIAA Journal*, 2017. doi: 10.2514/1.J055931.

[64] W. Kaufmann. Über die Ausbreitung kreiszylindrischer Wirbel in zähen (viskosen) Flüssigkeiten. *Ingenieur-Archiv*, 31(1):1–9, 1962. doi: 10.1007/bf00538235.

[65] A. Khavaran. Prediction of Turbulence-Generated Noise in Unheated Jets. Technical Report 213827, NASA, 2005.

[66] P. Költzsch. Ein Beitrag zur Berechnung des Wirbellärms von Axialventilatoren. In *Jahrestagung der Deutschen Akustischen Gesellschaft*, Frankfurt am Main, Germany, 1993.

[67] R. H. Kraichnan. Diffusion by a Random Velocity Field. *Physics of Fluids*, 13(1):22, 1970. doi: 10.1063/1.1692799.

[68] F. Krömer, A. Renz, and S. Becker. Experimental Investigation of the Sound Reduction by Leading-Edge Serrations in Axial Fans. *AIAA Journal*, 56(5):2086–2090, May 2018. doi: 10.2514/1.j056355.

[69] F. J. Krömer. *Sound emission of low-pressure axial fans under distorted inflow conditions*. PhD thesis, 2018.

[70] C. L. Ladson and J. Brooks, Cuyler W. Development of a computer program to obtain ordinates for NACA 4-digit, 4-digit modified, 5-digit, and 16 series airfoils. Technical report, NASA Langley Research Center; Hampton, VA, United States, 1975.

[71] R. Larusson, H. E. Hafsteinsson, N. Andersson, and L.-E. Eriksson. Investigation of Supersonic Jet Flow Using Modal Decomposition. In *20th AIAA/CEAS Aeroacoustics Conference*. American Institute of Aeronautics and Astronautics, June 2014. doi: 10. 2514/6.2014-3312.

[72] D. J. Lee and S. O. Koo. Numerical study of sound generation due to a spinning vortex pair. *AIAA Journal*, 33(1):20–26, Jan. 1995. doi: 10.2514/3.12327.

[73] M. J. Lighthill. On sound generated aerodynamically I. General theory. *Proceedings of the Royal Society of London*, 211:564–587, 1951.

[74] M. J. Lighthill. On sound generated aerodynamically II. Turbulence as a source of sound. *Proceedings of the Royal Society of London*, 222:1–32, 1953.

[75] A. Lodermeyer, M. Tautz, S. Becker, M. Döllinger, V. Birk, and S. Kniesburges. Aeroacoustic analysis of the human phonation process based on a hybrid acoustic PIV approach. *Experiments in Fluids*, 59(1), Dec. 2017. doi: 10.1007/s00348-017-2469-9.

[76] R. D. Madison. *Fan Engineering (Handbook)*. Buffalo Forge Company, Buffalo N.Y., 1949.

[77] S. Magne, M. Sanjose, S. Moreau, and A. Berry. Numerical Optimization of Fan Tonal Noise Control using Acoustic Modulation of Slowly-Rotating Obstructions. In *20th AIAA/CEAS Aeroacoustics Conference*. American Institute of Aeronautics and Astronautics, June 2014. doi: 10.2514/6.2014-2948.

[78] P. Martínez-Lera and C. Schram. Correction techniques for the truncation of the source field in acoustic analogies. *The Journal of the Acoustical Society of America*, 124(6): 3421–3429, Dec. 2008. doi: 10.1121/1.2999555.

[79] F. R. Menter and M. Kuntz. Adaptation of Eddy-Viscosity Turbulence Models to Unsteady Separated Flow Behind Vehicles. In *The Aerodynamics of Heavy Vehicles: Trucks, Buses, and Trains*, pages 339–352. Springer Berlin Heidelberg, 2004. doi: 10.1007/978-3-540-44419-0_30.

[80] M. Messner. *Fast boundary element methods in acoustics*. Citeseer, 2012.

[81] S. Moreau. Numerical and analytical predictions of low-speed fan aeroacoustics (keynote lecture). In *Fan2015*, Lyon, France, 2015.

[82] S. Moreau and M. Roger. Back-scattering correction and further extensions of Amiet's trailing-edge noise model. Part II: Application. *Journal of Sound and Vibration*, 323 (1-2):397–425, June 2009. doi: 10.1016/j.jsv.2008.11.051.

[83] E.-A. Müller and F. Obermeier. The spinning vortices as a source of sound. In *Fluids dynamics of Rotor and Fan supported Aircraft at Subsonic Speeds*, 1967.

[84] M. L. Munjal, M. Vorländer, P. Költzsch, M. Ochmann, and A. Cummings. *Formulas of Acoustics.* Springer-Verlag GmbH, 2008. ISBN 3540768327.

[85] C. Munz, M. Dumbser, and S. Roller. Linearized acoustic perturbation equations for low Mach number flow with variable density and temperature. *Journal of Computational Physics*, 224:352 – 364, 2007.

[86] M. Möser. *Technische Akustik.* Springer Berlin Heidelberg, 2009.

[87] A. A. Oberai, F. Roknaldin, and T. J. Hughes. Computational procedures for determining structural-acoustic response due to hydrodynamic sources. *Computer Methods in Applied Mechanics and Engineering*, 190:345–361, 2000.

[88] F. Perot, S. Moreau, M.-S. Kim, M. Henner, and D. Neal. Direct aeroacoustics predictions of a low speed axial fan. In *16th AIAA/CEAS Aeroacoustics Conference*. American Institute of Aeronautics and Astronautics, June 2010. doi: 10.2514/6.2010-3887.

[89] M. Piellard, B. B. Coutty, V. L. Goff, V. Vidal, and F. Perot. Direct aeroacoustics simulation of automotive engine cooling fan system: effect of upstream geometry on broadband noise. In *20th AIAA/CEAS Aeroacoustics Conference*. American Institute of Aeronautics and Astronautics, June 2014. doi: 10.2514/6.2014-2455.

[90] I. Proudman. The Generation of Noise by Isotropic Turbulence. *Proceedings of the Royal Society A: Mathematical, Physical and Engineering Sciences*, 214(1116):119–132, Aug. 1952. doi: 10.1098/rspa.1952.0154.

[91] F. Pérot, M.-S. Kim, S. Moreau, and M. Henner. Axial fan noise aeroacoustics predictions and inflow effect on tonal noise using LBM. In *Annual Conference of the CFD Society of Canada*, Sherbrooke, Canada, May 2013.

[92] W. J. M. Rankine. *Manual of applied mechanics.* Griffin, 1876.

[93] H. Reichardt. Vollständige Darstellung der turbulenten Geschwindigkeitsverteilung in glatten Leitungen. *ZAMM - Zeitschrift für Angewandte Mathematik und Mechanik*, 31 (7):208–219, 1951. doi: 10.1002/zamm.19510310704.

[94] H. S. Ribner. Aerodynamic sound from fluid dilatations, a theory of the sound from jets and other flows. *UTIA*, (86), 1962.

[95] M. Roger and S. Moreau. Back-scattering correction and further extensions of Amiet's trailing-edge noise model. Part 1: theory. *Journal of Sound and Vibration*, 286(3):477–506, Sept. 2005. doi: 10.1016/j.jsv.2004.10.054.

[96] C. L. Rumsey, J. P. Slotnick, M. Long, R. A. Stuever, and T. R. Wayman. Summary of the first AIAA CFD high-lift prediction workshop. *Journal of Aircraft*, 48(6):2068–2079, Nov. 2011. doi: 10.2514/1.c031447.

[97] M. D. Salas. Some observations on grid convergence. *Computers & Fluids*, 35(7):688–692, Aug. 2006. doi: 10.1016/j.compfluid.2006.01.003.

[98] M. Sanjose, M. Pestana, S. Moreau, and P. Caule. Evaluation of analytical aeroacoustic models for a low-speed axial ventilation system. In *Proceedings of International Conference of Fan Noise*, 2018.

[99] S. Schoder, C. Junger, M. Weitz, and M. Kaltenbacher. Conservative source term interpolation for hybrid aeroacoustic computations. In *25th AIAA/CEAS Aeroacoustics Conference*. American Institute of Aeronautics and Astronautics, May 2019. doi: 10.2514/6.2019-2538.

[100] M. Scully and J. Sullivan. Helicopter rotor wake geometry and airloads and helicopter rotor wakes. Technical report, MASSACHUSETTS INST OF TECH CAMBRIDGE AEROPHYSICS LAB, 1972.

[101] J. H. Seo and Y. J. Moon. Linearized perturbed compressible equations for low mach number aeroacoustics. *Journal of Computational Physics*, 218:702–719, 2006.

[102] Sharland, I. J. Sources of Noise in Axial Flow Fans. *Journal of Sound and Vibration*, 1 (3):302–322, 1964. doi: 10.1016/0022-460x(64)90068-9.

[103] M. L. Shur, P. R. Spalart, M. K. Strelets, and A. K. Travin. A hybrid RANS-LES approach with delayed-DES and wall-modelled LES capabilities. *International Journal of Heat and Fluid Flow*, 29(6):1638–1649, Dec. 2008. doi: 10.1016/j.ijheatfluidflow.2008. 07.001.

[104] *Star-CCM+ 12.06.011 User Guide*. Siemens Product Lifecycle Management Software Inc., 2017.

[105] J. Smagorinsky. General Circulation Experiments with the Primitive Equations. *Monthly Weather Review*, 91(3):99–164, Mar. 1963. doi: 10.1175/1520-0493(1963)091<0099: gcewtp>2.3.co;2.

[106] P. Spalart and S. Allmaras. A one-equation turbulence model for aerodynamic flows. In *30th Aerospace Sciences Meeting and Exhibit*. American Institute of Aeronautics and Astronautics, Jan. 1992. doi: 10.2514/6.1992-439.

[107] P. R. Spalart, S. Deck, M. L. Shur, K. D. Squires, M. K. Strelets, and A. Travin. A new version of detached-eddy simulation, resistant to ambiguous grid densities. *Theoretical and Computational Fluid Dynamics*, 20(3):181–195, May 2006. doi: 10.1007/ s00162-006-0015-0.

[108] K. Takeishi, M. Matsuura, S. Aoki, and T. Sato. An experimental study of heat transfer and film cooling on low aspect ratio turbine nozzles. In *Volume 4: Heat Transfer; Electric Power; Industrial and Cogeneration*. ASME, June 1989. doi: 10.1115/89-gt-187.

[109] C. K. W. Tam and L. Auriault. Jet mixing noise from fine-scale turbulence. *AIAA Journal*, 37(2):145–153, Feb. 1999. doi: 10.2514/2.691.

[110] M. Tautz, M. Kaltenbacher, and S. Becker. Comparison of Lighthill's Analogy and Acoustic Perturbation Equations for the Prediction of HVAC Blower Noise. In *FAN 2018 Proceedings*, 2018.

[111] THE EUROPEAN PARLIAMENT AND THE COUNCIL OF THE EUROPEAN UNION. Directive 2000/14/EC of the european parliament and of the council of 8 may 2000 on the approximation of the laws of the member states relating to the noise emission in the environment by equipment for use outdoors, 2000.

[112] THE EUROPEAN PARLIAMENT AND THE COUNCIL OF THE EUROPEAN UNION. Directive 2003/10/EC of the european parliament and of the council of 6 february 2003 on the minimum health and safety requirements regarding the exposure of workers to the risks arising from physical agents (noise) (seventeenth individual directive within the meaning of article 16(1) of directive 89/391/EEC), 2003.

[113] THE EUROPEAN PARLIAMENT AND THE COUNCIL OF THE EUROPEAN UNION. Directive 2006/42/EC of the european parliament and of the council of 17 may 2006 on machinery, and amending directive 95/16/EC (recast), 2006.

[114] J. Vassberg, E. Tinoco, M. Mani, B. Rider, T. Zickuhr, D. Levy, O. Brodersen, B. Eisfeld, S. Crippa, R. Wahls, J. Morrison, D. Mavriplis, and M. Murayama. Summary of the fourth AIAA CFD drag prediction workshop. In *28th AIAA Applied Aerodynamics Conference*. American Institute of Aeronautics and Astronautics, June 2010. doi: 10.2514/6.2010-4547.

[115] G. H. Vatistas, V. Kozel, and W. C. Mih. A simpler model for concentrated vortices. *Experiments in Fluids*, 11(1):73–76, Apr. 1991. doi: 10.1007/bf00198434.

[116] R. W. White. Acoustic ray tracing in moving inhomogeneous fluids. *The Journal of the Acoustical Society of America*, 53(6):1700–1704, June 1973. doi: 10.1121/1.1913522.

[117] D. C. Wilcox. *Turbulence Modeling for CFD (Third Edition)*. D C W Industries, 2006. ISBN 9781928729082.

[118] J. E. F. Williams and D.L.Hawkings. Sound generation by turbulence and surface in arbitratry motion. *Philosophical Transactions of the Royal Society of London, Series A, Mathematical and Physical Sciences*, 264:321–342, 1969.

[119] J. Winkler, R. Sandberg, and S. Moreau. Direct Numerical Simulation of the Self-Noise Radiated by an Airfoil in a Narrow Stream. In *18th AIAA/CEAS Aeroacoustics Conference (33rd AIAA Aeroacoustics Conference)*. American Institute of Aeronautics and Astronautics, June 2012. doi: 10.2514/6.2012-2059.

[120] D. A. Wolf-Gladrow. *Lattice-Gas Cellular Automata and Lattice Boltzmann Models*. Springer-Verlag GmbH, 2000. ISBN 3540669736.

[121] S. Wright. The acoustic spectrum of axial flow machines. *Journal of Sound and Vibration*, 45(2):165–223, Mar. 1976. doi: 10.1016/0022-460x(76)90596-4.

[122] K. Yousefi and A. Razeghi. Determination of the critical reynolds number for flow over symmetric NACA airfoils. In *2018 AIAA Aerospace Sciences Meeting*. American Institute of Aeronautics and Astronautics, jan 2018. doi: 10.2514/6.2018-0818.

[123] F. Zenger, C. Junger, M. Kaltenbacher, and S. Becker. A benchmark case for aerodynamics and aeroacoustics of a low pressure axial fan. In *SAE Technical Paper 2016-01-1805*, 2016. doi: 10.4271/2016-01-1805.

[124] X. Zhang, A. Sciacchitano, and S. Pröbsting. Aeroacoustic analysis of an NACA 0015 airfoil with Gurney flap based on time-resolved PIV measurements. In *INTER-NOISE 2016*, Hamburg, Germany, Aug. 2016.

Curriculum Vitae

Personal Data

Name: Clemens Junger

Date of Birth: June 16, 1987

Place of Birth: Reutlingen, Germany

Education

09/2003 – 06/2006   Apprenticeship Mechatronics
                     Gebr. Heller GmbH, Nürtingen, Germany

09/2006 – 09/2008   Diploma from secondary school
                     Philipp-Matthäus-Hahn-Schule, Nürtingen, Germany

10/2008 – 10/2013   Dipl.-Ing. Aerospace Engineering
                     University of Stuttgart, Germany

Professional Experiences

02/2014 – 08/2019   Research and Teaching Assistant
                     Research Unit of Technical Acoustics
                     TU Wien, Austria